Structure and Dynamics of Low-mass Star-forming Cores

Spandan Choudhury

München 2022

Structure and Dynamics of Low-mass Star-forming Cores

Spandan Choudhury

Dissertation
der Fakultät für Physik
der Ludwig-Maximilians-Universität
München

vorgelegt von
Spandan Choudhury
aus Guwahati, Indien

München, den 25/05/2022

Erstgutachter: Prof. Dr. Paola Caselli
Zweitgutachter: Prof. Dr. Andreas Burkert
Tag der mündlichen Prüfung: 7/7/2022

To Ma and Deuta

Contents

List of Figures

List of Tables

Zusammenfassung

Während ihrer ganzen Geschichte hindurch haben helle Sterne im Nachthimmel die Menschheit fasziniert. Für lange Zeit waren astronomische Beobachten auf helle Objekte wie Sterne oder Galaxien, welche bei optischen Wellenlängen sichtbar sind, beschränkt. Seit dem letzten Teil des 20. Jahrhunderts jedoch bieten Radioteleskope die Möglichkeit, ein komplett neues Set an astronomischen Objekten, welche bei optischen Wellenlängen so gut wie keinen Fluss emittieren und somit zuvor unentdeckt waren, zu beobachten. Im Besonderen ermöglichte das die Beobachtung und das Studium des Gases in verschiedenen Phasen des interstellaren Mediums (ISM). Das ISM ist der scheinbar leere Raum zwischen Sternen, welcher tatsächlich Gas in Dichten wesentlich geringer als das beste auf der Erde erzeugte Vakuum (weniger als einige tausend Teilchen pro Kubikzentimeter) beinhaltet. Eine der wichtigsten Entwicklungen war die Fähigkeit, Sternentstehungsgebiete während der Entwicklungsphasen, welche zur Entstehung des optischen Sterns (stellare Emission vorwiegend bei optischen Wellenlängen) führen, zu studieren, was bedeutet, dass wir nun den Entstehungsprozess von Sternen und die verschiedenen beeinflussenden Umgebungsfaktoren erforschen können.

Die Erkundung der Sternentstehungsgeschichte ist im Fall von Sternen niedriger Masse wie etwa unserer Sonne von besonderem Interesse, da sie direkt an die Geschichte unseres eigenen Sonnensystems knüpft. Im Fall von Sternen niedriger Masse wird die physikalische und chemische Struktur des Sterns beinahe vollständig von den Eigenschaften dichter Kerne, welche ihre Vorgänger sind, bestimmt. Dichte Kerne wiederum entstehen aus Material höherer Dichte innerhalb der Molekülwolken, welche die dichtesten und kältesten Gebiete im ISM sind. Daher ist das Studium der Sternentstehung inhärent mit dem Studium dichter Kerne und Molekülwolken verbunden. In dieser Arbeit präsentiere ich die Ergebnisse meiner Beobachtungen von dichten Kernen in nahegelegenen Molekülwolken, in denen Sterne entstehen und zeige dabei, wie tiefere Beobachtungen und fortgeschrittenere Analysetechniken neue Einblicke ermöglichen. Ich nutze die Vorteile des NH_3 Inversionslinienübergangs, um die Gebiete zu erkunden und das Gas in Relation zu Sternentstehungsprozessen zu erforschen.

Das erste Projekt konzentriert sich auf den Einfluss der Molekülwolkenkomponente entlang der Sichtlinie (eng.: “line-of-sight”, kurz “LoS”) in Richtung der dichten Kerne. Da diese Kerne im Durchschnitt eine um eine Größenordnung höhere Dichte haben als die umgebende Wolke, wird die Emission in der LoS vom Kernmaterial dominiert. Die Wolke im Vordergrund und Hintergrund des Kerns tragen jedoch auch zur Gesamtemission bei. Da diese Wolkenkomponente im Vergleich zum typischen Rauschen der Beobachtung schwach ist, wird sie bei Beobachtungen dichter Kerne oft nicht detektiert. Mit der verbesserten Empfindlichkeit bei gestapelten Spektren

strebe ich die Quantifizierung des Einflusses auf die Messungen der Kerneigenschaften an, da die Wolkenkomponenten in den Beobachtungen nicht berücksichtigt werden.

Im zweiten Teil erkunde ich den Übergang zur Kohärenz mithilfe von gestapelten Spektren in der Umgebung dichter Kerne. Frühere Beobachtungen haben gezeigt, dass das Gas in Molekülwolken supersonische Turbulenzen aufweist, was bedeutet, dass die turbulenten Bewegungen der Teilchen größer sind, als was von reinen thermischen Bewegungen erwartet werden kann. Im Gegensatz dazu weist das Material im dichten Kern Turbulenzen kleiner als die thermische Geschwindigkeit auf. Dies impliziert, dass an den Kerngrenzgebieten ein Übergang von turbulenten Wolken zu den sogenannten "kohärenten" dichten Kernen stattfinden muss und es wurde in der Tat vor kurzem beobachtet, dass dieser scharf ist. Dieses Übergangsgebiet wurde jedoch nicht mit hoher Empfindlichkeit, welche eine Entflechtung der Kern- und Wolkenkomponenten ermöglicht, erforscht. Dies ist essentiell für die Charakterisierung des physikalischen Eigenschaften, die den Übergang von turbulentem zu ruhigem Gas begleiten.

Für diese zwei Teile präsentiere ich meine Ergebnisse im Bezug auf kohärente Kerne in der Molekülwolke L1688 in Ophiuchus, welche auf Beobachtungen mit einem großen Einzelreflektorteleskop basieren.

Zu guter Letzt konzentriere ich mich auf die Strukturen, die im Innern dichter Kerne beobachtet wurden. Aufgrund von Gravitation fallen dichte Kerne in sich zusammen und formen einen "Protostern", das früheste Stadium eines Sterns, wenn kein starker interner Druck den Kern aufrechterhält. Falls der Kern eine ausreichende Masse hat, die eine weitere Fragmentierung erlaubt, dann gehen während des Kollaps der Entstehung eines Protosterns Strukturen wie "Filamente" und "Kondensationen" voraus. Ein solcher Fall wurde im isolierten, dichten Kern Barnard 5 (B5) in der Perseus Molekülwolke beobachtet. Aktuelle Beobachtungen haben zusätzlich zu einem jungen stellaren Objekt (eng. "young stellar object", kurz "YSO") zwei Filamente und drei Kondensationen in B5 offenbart. Voraussagen weisen darauf hin, dass diese Kondensationen mit dem YSO ein gebundenes Vierersystem formen werden. Ich benutze eine Vielkomponentenanalyse mit Beobachtungen hoher Auflösung ($\approx$2400 A.U.) in Richtung von B5, um Geschwindigkeitsstrukturen, die mit den zwei Filamenten assoziiert werden, zu betrachten und mögliche Hinweise auf den Einfall von Material in diese hineinzufinden.

Die Ergebnisse in dieser Arbeit werden zum Teil von der Auflösung und Empfindlichkeit der verfügbaren Daten begrenzt. Nachfolgende Beobachtungen mit Einzelreflektoren oder Interferometern mit höherer Empfindlichkeit werden dabei helfen, die Verbindungen zwischen Strukturen unterschiedlicher Größenordnungen in Sternentstehungsgebieten zu verstehen. Das wird sicherlich zu unserem Verständnis der Entstehungsgeschichte von Sternen und dem Effekt der Eigenschaften der umliegenden Wolke in diesem Prozess beitragen.

Abstract

The bright stars in the night sky have fascinated mankind throughout human history. For a long time, the astronomical observations were limited to bright objects like the stars and galaxies, which are visible in the optical wavelengths. However, since the later part of the 20^{th} century, advancements in radio telescopes offered the possibility to observe a completely new set of astronomical objects, which emitted little to no flux in the optical wavelengths and were therefore previously undetected. In particular, this made it possible to observe and study the gas in different phases of the interstellar medium (ISM). The ISM is the seemingly empty space between stars which, in fact, contains gas in densities smaller than the best vacuum created on Earth (less than a few thousand particles per cubic centimetre). A key development was the ability to observe the star-forming regions at evolutionary stages leading to the formation of the optical star (stellar emission predominantly at optical wavelengths). This meant that we could now study the process of formation of stars and the different environmental factors that affect it.

The exploration of the star formation history is particularly of interest in the case of low-mass stars like our sun due to how directly it connects with the history of our own solar system. In the case of low-mass stars, the physical and chemical structure of the star is almost entirely decided by the dense core properties, which are their progenitors. Dense cores, in turn, are formed from over-densities of material inside molecular clouds, which are the densest and coldest regions in the ISM. Therefore, the study of star formation is inherently linked to the study of dense cores and molecular clouds. In this thesis, I present observational results in my study of dense cores in nearby star-forming molecular clouds, showing how deeper (higher sensitivity) observations and more advanced analysis techniques reveal new insights. I take advantage of NH_3 inversion line transitions to explore the regions and probe the gas in relation to the star formation process.

The first project focuses on the effect of the molecular cloud component along the line-of-sight (LoS) towards the dense cores. As the cores are, on average, about an order of magnitude higher in density than the surrounding cloud, the emission in the LoS is dominated by the core material. However, the cloud in the foreground and background of the core also contributes to the total emission. Since this cloud component is faint compared to the typical noise of the observations, it is often not detected in observations of dense cores. With improved sensitivities using stacked spectra, I aim to quantify the effects on the measurements of the core properties due to the cloud component not being accounted for in the observations.

In the second part, I explore the transition to coherence with the help of stacked spectra in the vicinity of dense cores. Previous observations have revealed that the gas in molecular clouds shows supersonic turbulence, i.e., the turbulent motions of the particles are larger than what

is expected from pure thermal motions. In contrast, the dense core material shows turbulence lower than the thermal speed. This implies that a transition from turbulent clouds to the so-called "coherent" dense cores must occur at the core boundaries, and indeed, it was recently observed to be sharp. However, this transition region has not been studied with high sensitivity, which allows for disentanglement of the core and cloud components. This is essential to characterise the physical properties accompanying the transition from turbulent to quiescent gas.

For these two parts, I present my findings in relation to the coherent cores in the molecular cloud L1688 in Ophiuchus using observations with a large single-dish telescope.

Finally, I focus on the structures observed in the interiors of dense cores. Due to gravity, a dense core collapses onto itself to form a "protostar", the earliest stage of a star, when there is no strong internal pressure to sustain the core. Due to gravity, a dense core collapses onto itself when there is no strong internal pressure to sustain the core, to form a "protostar", the earliest stage of a star. If the core has sufficient mass to allow further fragmentation, then during the collapse, structures like "filaments" and "condensations" precede the formation of the protostar. One such case is observed in the isolated dense core Barnard 5 (B5) in the Perseus molecular cloud complex. Recent observations have revealed two filaments and three condensations in B5 in addition to a young stellar object (YSO). These condensations, along with the YSO, are predicted to form a bound quadruple system. I use multi-component analysis with high-resolution ($\approx$2400 au) observations towards B5 to look at velocity structures associated with the two filaments and find possible signs of infall of material onto them.

The results presented in this thesis are, in part, limited by the resolution and sensitivities of available data. Follow-up observations with higher sensitivities, using single-dish telescopes and interferometers, will help understand the connections between different-scale structures in star-forming regions. This will certainly add to our knowledge of the formation history of stars and the effect of the properties of the surrounding cloud in the process.

Chapter 1

Introduction

Figure 1.1: View of the Milky Way above Cerro Paranal mountain in Chile. The dark patches in the middle are due to interstellar dust obscuring the light from the background stars. *Credit : (A. Ghizzi Panizza/ESO)*

Since time immemorial, mankind has been fascinated with bright stars in the night sky. The formation and evolution of stars continues to be a topic of immense interest and importance in astronomy even today. Especially the formation history of low-mass ($<2M_{\odot}$, where $M_{\odot}$ is the mass of the Sun) is of particular interest to astronomers as it presents a way to understand the formation of the Sun and the solar system.

Star formation occurs in the dense cores embedded in molecular clouds in the interstellar medium (ISM). The physical and chemical structure of these cores regulates the initial conditions during the formation of the stars. Therefore, the study of the structure and kinematics of the dense cores is essential in understanding star formation.

Dense cores are observed using molecular line transitions. Different transitions trace different physical and chemical conditions (such as density, temperature, age). Therefore, using suitable molecular tracers, we are able to observe different layers of the molecular cloud and core. This also helps us study the different levels of structures present within and around the cores.

This Introduction briefly describes some concepts and methods used in the study and observations of star formation. Section 1.1 introduces the different phases and properties of the interstellar medium. In Section 1.2, we focus on the gas in molecular clouds, with attention to star-forming regions in the Milky Way. The classical low-mass star formation process is presented in Section 1.4. Dense cores, which are the focus of this thesis, are introduced in Section 1.3. In Section 1.5, we present observational and analytical tools used in our study. Finally, the contents of this thesis are laid out in Section 1.6.

1.1 Interstellar Medium

The process of star formation starts with the condensation of gas in the interstellar medium (ISM) of galaxies. Under the effect of gravity, the diffuse gas in the ISM gradually becomes denser, and under favourable conditions, it leads to the formation of molecular clouds, dense cores and finally, stars. This evolution is dictated by the physical and chemical structure of the ISM. Therefore, the study of the properties of the ISM constitutes an integral part of understanding the process of star formation. This section focuses on the properties of the ISM in the context of our host galaxy, the Milky Way. The Milky Way is a barred spiral galaxy of mass $M \sim 10^{12}\,\mathrm{M}_\odot$ (McMillan 2017) and visible diameter $d \sim 2 \times 10^5$ ly (or 60 kpc). The solar system is located near the mid-plane of the galaxy at a distance of approximately 8 kpc from its centre. Therefore, the Milky Way is viewed edge-on from the earth and appears to be a narrow band of white light (Figure 1.1) about 30° wide. The interstellar medium accounts for $\sim$ 10% of the mass in the Milky Way.

It is estimated that approximately 70% of the mass of the ISM in the Milky Way is constituted by hydrogen, the most abundant element in the universe. The material in the ISM is present in a wide range of temperature and density, constituting different phases. Correspondingly, the dominant form of hydrogen at each of these phases also varies from ionised (H^+, also denoted as HII) to neutral atomic (H, denoted as HI) to molecular (H_2). Based on their temperature and the predominant form of hydrogen present, the primary distinguishable phases of the ISM are the *warm ionised medium* (WIM), the *warm* and *cold neutral medium* (WNM and CNM) and *molecular gas*. WIM has a typical temperature of $T \sim 8000\,\mathrm{K}$ and a particle number density of $n \sim 0.3\ \mathrm{cm}^{-3}$, and the hydrogen is predominantly in the ionised form. WNM and CNM differ in temperature and density, with atomic hydrogen being the dominant form in both phases. WNM has temperatures and densities similar to the WIM, whereas the CNM exhibits temperatures of $T = 50 - 100\,\mathrm{K}$ and densities of $n = 20 - 50\ \mathrm{cm}^{-3}$. The neutral hydrogen (HI) line at 21 cm is commonly used to trace the neutral ISM (Figure 1.2). Molecular clouds, where hydrogen is mostly in H_2 form, are denser and colder than CNM, with $T = 10 - 20\,\mathrm{K}$ and $n = 10^2 - 10^6\ \mathrm{cm}^{-3}$. These different phases exist in pressure equilibrium with each other (McKee & Ostriker 1977; Ferrière 2001). In relation to star formation, molecular clouds are of greatest interest, as the

process takes place in this phase of the ISM.

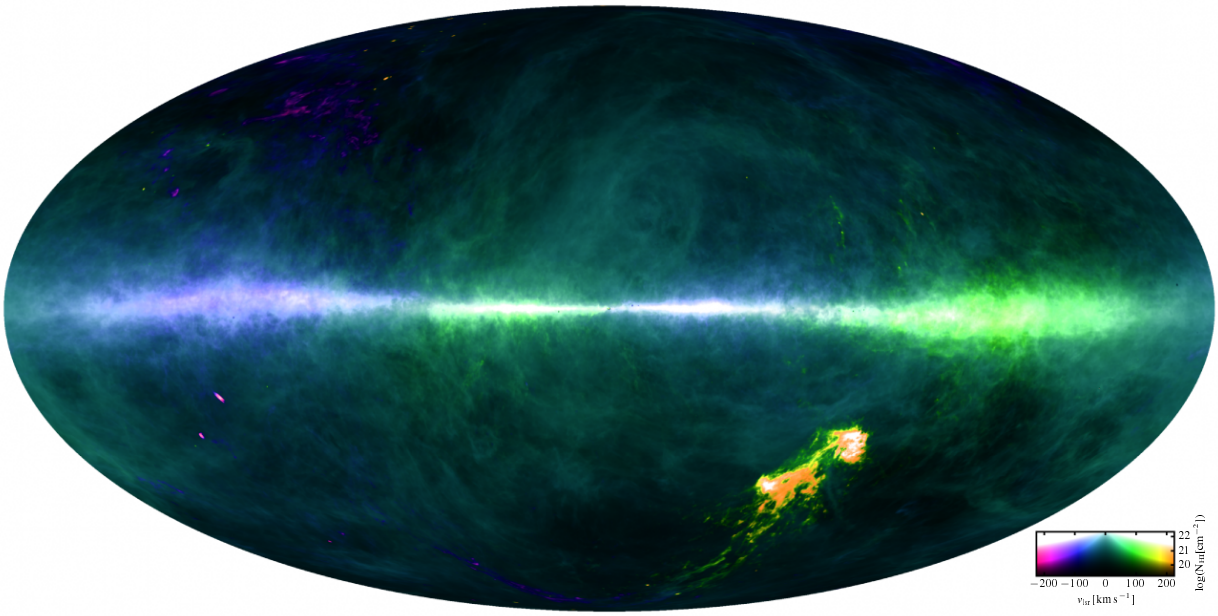

Figure 1.2: Column densities of HI at different velocities, using observations of the 21 cm line from the HI4PI survey. It clearly shows that the HI emission is dominated by the galactic plane. Figure from HI4PI Collaboration et al. (2016).

1.2 Molecular clouds in Milky Way

1.2.1 Observations of molecular clouds

As mentioned in Section 1.1, the densest and coldest parts of the ISM are the molecular clouds, which are the laboratories to study the process of star formation. Being relatively close, the cold *dark clouds* (so called, as they are seen as dark patches in optical images) in the Milky Way could be spatially resolved at radio wavelengths using ground-based large single-dish telescopes and interferometers. This allows us to study the physical, dynamical and chemical properties of different scale structures in the molecular clouds, like filaments and dense cores. Molecular clouds are present throughout the galaxy and therefore offer the possibility to study star formation in different conditions of interstellar radiation field (ISRF), low- and high-mass regions, and isolated vs cluster environments. The closest star forming molecular clouds are Ophiuchus and Taurus, which are both regions of low-mass star formation at distances of 120-160 pc (Ortiz-León et al. 2018; Galli et al. 2018) . The nearest high-mass (stellar mass>$8M_{\odot}$) region is the Orion molecular cloud, at a distance of $\sim$ 400 pc (Kounkel et al. 2017). Some of the prominent and widely studied molecular clouds are highlighted in Figure 1.3.

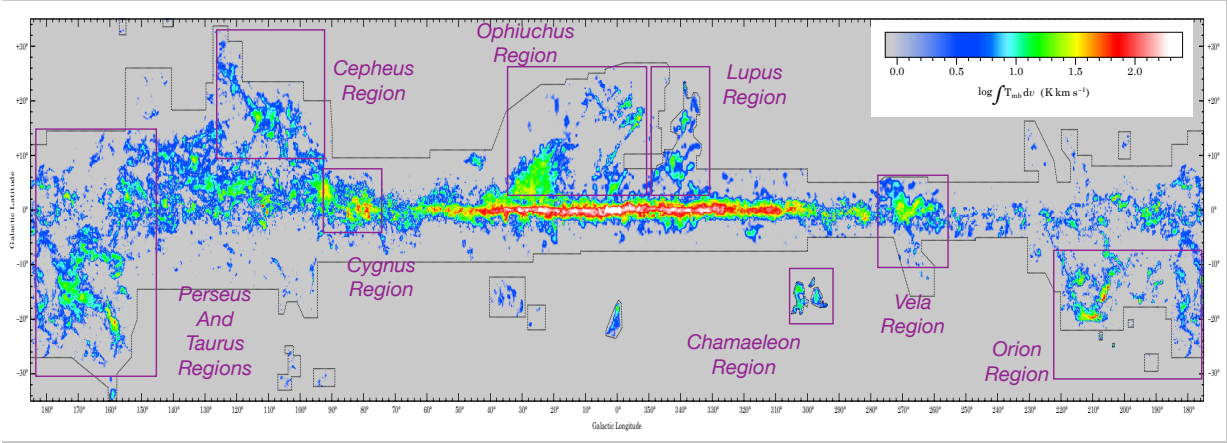

Figure 1.3: Integrated intensity of CO emission in Milky Way, combined from multiple surveys using the 1.2m telescopes at Center for Astrophysics, Harvard & Smithsonian in the United States and Cerro Tololo in Chile.. The black lines show the area covered by the surveys. The nearby and prominent molecular cloud complexes, including Ophiuchus and Perseus (two regions of interest in this thesis), are highlighted in purple. Figure adapted from Dame et al. (2001).

The most abundant molecule in this phase is H_2. However, being a non-polar molecule (dipole moment is zero), it has no strong lines in the infrared or radio frequencies. Therefore, the next most abundant molecule, carbon monoxide (CO), is commonly used as a proxy to study the molecular phase of the ISM. The abundance of CO is roughly 10^{-4} relative to H_2. Many rotational transitions of CO and its isotopologues (^{13}CO, C^{18}O) can be observed in millimetre and sub-millimetre wavelengths and are therefore widely used in the observations of molecular clouds.

Due to the higher density inside the molecular clouds, the background starlight is often highly absorbed by the dust grains. Consequently, these clouds often appear as dark regions in visible and near-infrared (NIR) observations (see Figure 1.4). The total visual extinction by dust along the line-of-sight, A_v is commonly used as a reliable proxy for the gas column density of the cloud. The absorbed light is re-radiated from the dust grains at longer wavelengths via black-body radiation. This dust continuum emission is another one of the primary tools used to observe and characterise the molecular clouds.

1.2.2 Cloud Stability and Fragmentation

The dynamics of gas in molecular clouds are regulated by gravity, unlike the diffuse phases of the ISM, which are in pressure equilibrium. The stability of the cloud is given by the *virial theorem*, which gives the relation between the moment of inertia (I) of a cloud and its total energy. The energy content of the cloud could be broadly divided into the thermal energy, U, which is the kinetic energy due to the thermal motion of the particles inside the cloud, and potential energy

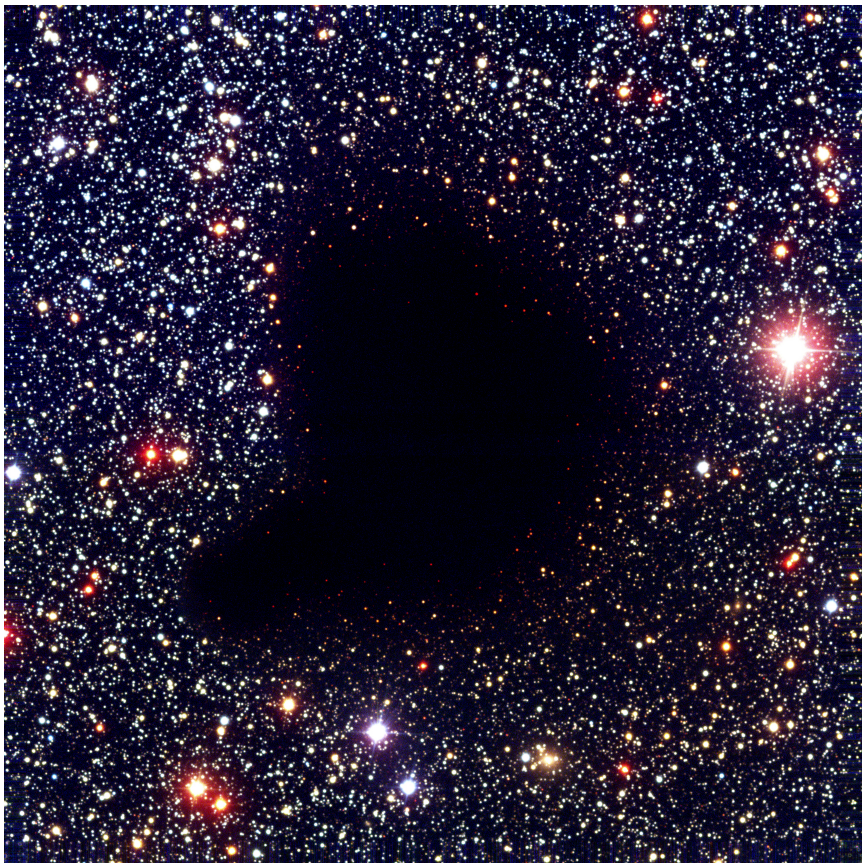

Figure 1.4: Composite visible and near-infrared image of the molecular cloud Barnard 68 in Ophiuchus, taken with the Very Large Telescope (VLT). Stars are visible at these wavelengths, but due to dust inside the molecular cloud, it is opaque. *Credit : (ESO)*

due to gravity, W. The simplified equation then reads :

$$\frac{1}{2}\frac{d^2I}{dt^2} = 2U + W \,, \tag{1.1}$$

Here, U is positive, and W is negative. For a molecular cloud of mass M, radius R (assuming spherical geometry) and internal temperature T,

$$U \sim \frac{3}{2}\frac{k_B T}{\mu m_H} M \,, \tag{1.2}$$

$$|W| \sim \frac{GM^2}{R} \,, \tag{1.3}$$

where k_B is the Boltzmann's constant, G is the gravitational constant, μ is the mean particle mass, and m_H is the mass of a hydrogen atom. Then, the ratio of thermal to gravitational energy is

$$\frac{U}{|W|} \approx \frac{3k_B TR}{2\mu m_H GM} \approx 0.02 \times \left(\frac{T}{20\,\mathrm{K}}\right)\left(\frac{R}{10\,\mathrm{pc}}\right)\left(\frac{M}{10^4\,\mathrm{M}_\odot}\right)^{-1} . \tag{1.4}$$

Therefore, for a molecular cloud of mass $10^4\,M_\odot$, size $\sim$ 10 pc and with typical gas temperature of $\sim$ 20 K, we have U/|W| $\approx$ 0.02. Therefore, the thermal energy is only about 2% of the gravitational energy, which means that for such a cloud, thermal motions alone cannot prevent gravitational collapse. We can then calculate the time required for the cloud to collapse under its own gravity, also known as the *free-fall time*, $t_{\rm ff}$. With thermal energy being relatively negligible, equation 1.1 becomes

$$\frac{1}{2}\frac{d^2I}{dt^2} = W \approx -\frac{GM^2}{R}\,, \tag{1.5}$$

and we get

$$t_{\rm ff} \approx \sqrt{\frac{R^3}{GM}}\,. \tag{1.6}$$

$t_{\rm ff}$ could also be obtained as the time taken for a sphere of uniform density ρ to collapse to a point in the absence of internal pressure :

$$t_{\rm ff} = \sqrt{\frac{3\pi}{32G\rho}}\,. \tag{1.7}$$

For a typical molecular cloud of dimensions mentioned above, the free-fall time is a few times 10^6 yr. However, the ages of molecular clouds estimated from observations are higher than this $t_{\rm ff}$. The rate of star formation predicted with such $t_{\rm ff}$ is also two orders of magnitude higher than what is observed (Robitaille & Whitney 2010). These suggest that the clouds are more stable than what would be achieved with only thermal motions of the particles to balance the gravitational potential. The additional factors providing cloud stability are kinetic energy, K from the bulk motion of the cloud (including rotation) and turbulence, and the energy stored in the magnetic field in the clouds, $\mathcal{M}$. Then, Equation 1.1 becomes :

$$\frac{1}{2}\frac{d^2I}{dt^2} = 2U + W + K + \mathcal{M}\,. \tag{1.8}$$

The turbulence in molecular clouds is seen to be supersonic in observations with CO and its isotopologues (Larson 1981), and the magnetic fields are present throughout the galaxy. Therefore, both these terms could provide a pressure balance against gravitational collapse.

Jeans Mass, M_J

The maximum mass of a cloud, which could be sustained by thermal pressure, is the Jeans mass, M_J. This mass could be calculated by considering Equation 1.1 in equilibrium, i.e., $2U = W$. We then have

$$\frac{k_BT}{\mu m_H} = \frac{GM_J}{R}\,. \tag{1.9}$$

Given that number density is $n = \rho/\mu m_H$, where $\rho \propto M/R^3$ is the density, we then get Jeans mass, M_J and corresponding Jeans length, λ_J as

$$M_J \propto T^{\frac{3}{2}} n^{-\frac{1}{2}} \approx 2M_\odot \left(\frac{T}{10\,K}\right)^{\frac{3}{2}} \left(\frac{n}{10^3 {\rm cm}^{-3}}\right)^{-\frac{1}{2}}\,, \tag{1.10}$$

$$\lambda_J \propto \left(\frac{M_J}{\mu m_H n}\right)^{\frac{1}{2}} \approx 0.4\mathrm{pc}\left(\frac{\mathrm{T}}{10\,\mathrm{K}}\right)^{\frac{1}{2}}\left(\frac{\mathrm{n}}{10^3\mathrm{cm}^{-3}}\right)^{-\frac{1}{2}} . \tag{1.11}$$

These equations highlight that colder temperatures facilitate collapse. From Equation 1.8, we also find that dissipation of turbulence helps the collapse. As M_J decreases with increasing density, the stable mass limit decreases during collapse and cloud fragments into *cores*. It is usually expected that an object with mass several times M_J is unstable and prone to fragmentation.

1.3 Dense Cores

Dense cores in molecular clouds are birthplaces of stars. The mass and chemical composition of a star is dictated by the core from which it is formed. Therefore, cores are studied in detail, and their structure and evolution are thought to be well-understood. These cores are characterised by higher density and lower temperatures compared to the parental cloud (Myers 1983; Myers & Benson 1983; Caselli et al. 2002). These cores typically have temperatures of about 10 K and densities n $\sim 10^4$ cm^{-3}. They are usually of few solar masses and have radii of $r \sim 0.1$ pc. Therefore, thermal motions can prevent further collapse of these smaller-scale structures (Equations 1.10 and 1.11). Gravitationally bound cores are also referred to as *prestellar cores*, as they are expected to form a *protostar* with further collapse (Figure 1.5 shows the different phases of star formation including molecular cloud and cores).

1.3.1 Observations of Dense Cores

The higher density found inside cores allows various chemical species to form on the dust grains, which are then released into the gas phase via various processes. The primary desorption mechanisms are *photo-evaporation* by energetic UV-photons induced by cosmic rays; *thermal desorption*, where the temperature is high enough to overcome the binding energy of the molecule to grains; and *chemical desorption*, where exothermic chemical reactions provide the necessary energy for desorption to its products. Due to the different *critical densities* needed to excite a particular line and variation of molecular abundances due to changing physical (and thus also chemical) conditions, spectral lines of different species and transitions can be used to observe different parts of the dense cores. Figure 1.6 shows some of the molecules abundant the gas phase and on dust grains in different parts of the dense cores (see Ceccarelli et al. 2014). Accurate knowledge of the *rest frequency* of molecular spectral lines and use of the *Doppler effect* allow for extraction of very useful information about the gas kinematics inside the cores. Observation of multiple spectral lines of the same specie also enables us to have an accurate measurement of the gas temperature and chemical abundances of the specie. Therefore, molecular lines are an integral part of the study of the physical and chemical structure of the dense cores.

Since the density of gas inside the core is much higher than the surrounding medium, molecular emission in the line of sight towards a core is heavily dominated by the core material. However, the material in the molecular cloud in the same line of sight is expected to also contribute to the observed flux. Due to the emission from the core being much stronger, it is not easy to detect

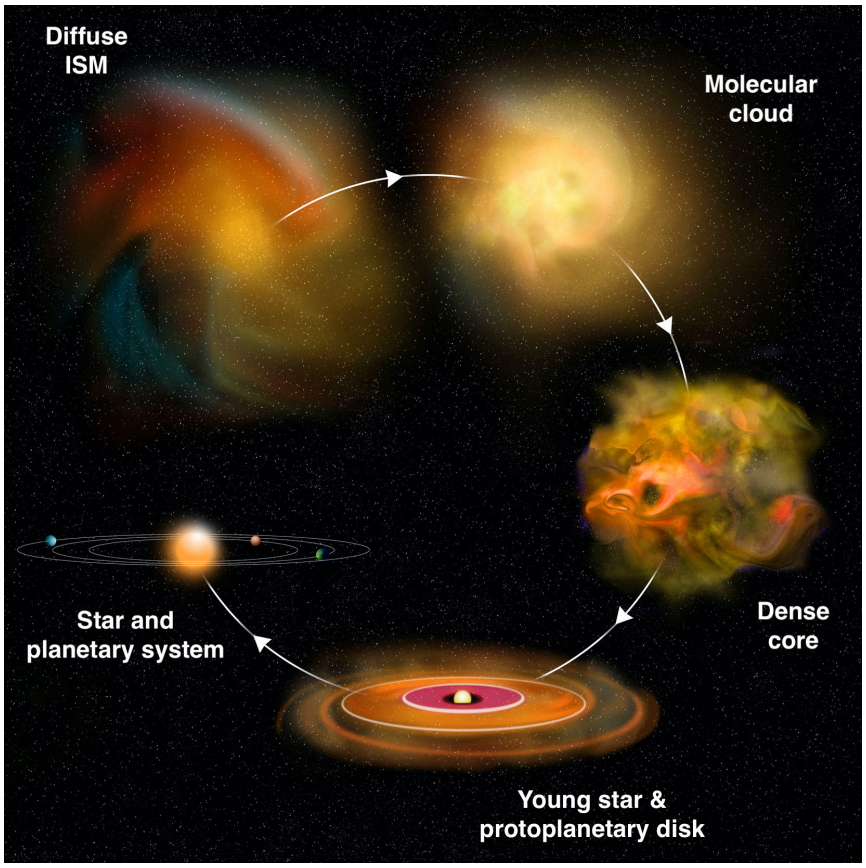

Figure 1.5: Schematic showing different stages of the star formation process. It starts with the diffuse material in the ISM, which then condenses into a molecular cloud. Then a dense core is formed, and gravitational collapse starts. This leads to the formation of protostars, which are usually surrounded by a protoplanetary disk. This system evolves to form the final stage of the star formation process: the star and orbiting planets. Credit : Bill Saxton/NRAO/AUI/NSF.

the relatively much fainter component from the molecular cloud. As both components arise from material with different physical conditions, it is imperative to disentangle the individual contributions if one is to measure the properties of dense cores robustly, as well as to understand how these cores form out of the cloud material. We focus on this in detail in Chapter 3.

Studies with high-density ($n(H_2) > 10^4$ cm^{-3}) tracers reveal subsonic levels of turbulence inside cores (Barranco & Goodman 1998; Caselli et al. 2002; Rosolowsky et al. 2008), in contrast to the supersonic linewidths observed in the ambient cloud (traced by lower density tracers, like CO; Larson 1981). The sharp transitions in turbulence and density lead to the current general understanding of cores being isolated units of star formation, well-separated from the surrounding cloud. However, the cloud-core transition has not been studied with high sensitivity in the vicinity of the cores. Direct observation of the transition region proves to be difficult, as typical high-density tracers do not emit significantly outside the cores, whereas using a classical cloud tracer like CO would only trace the outer layers of the cloud, and not the immediate surround-

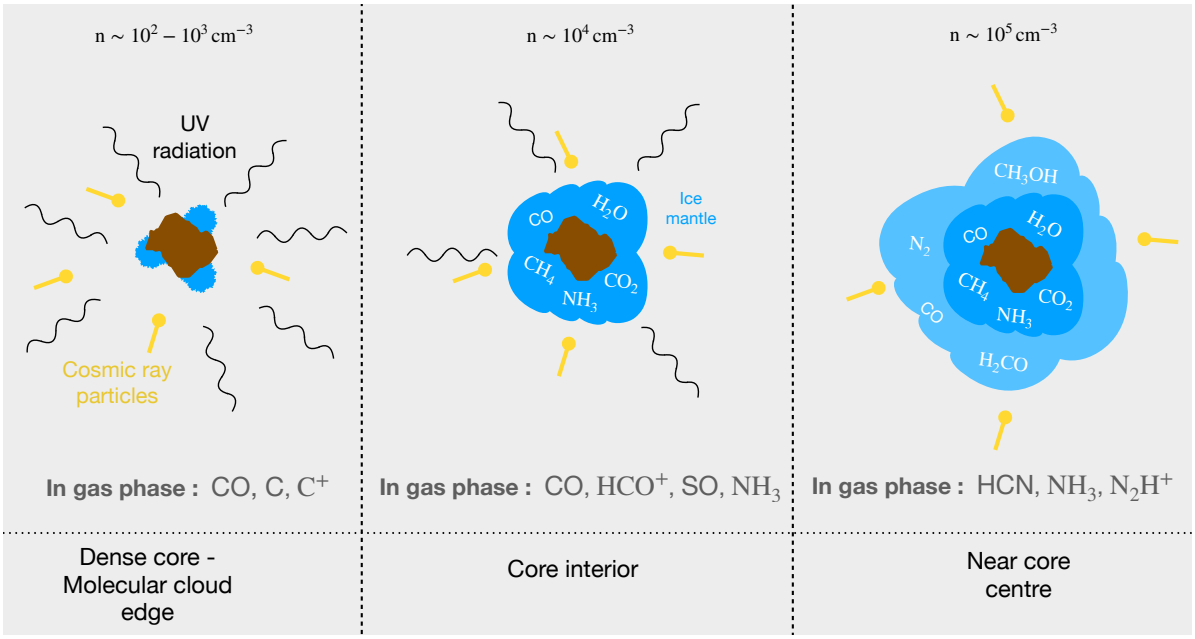

Figure 1.6: Schematic showing different chemical species present in the gas phase and the ice mantles on the grain surfaces at varying depths of the dense core. The molecules in the gas phase can be used as tracers in observations for the respective regions. Figure adapted from Caselli & Ceccarelli (2012) and Ceccarelli et al. (2014).

ing of the cores (see Figure 1.6). In Chapter 2, we use NH_3 inversion transitions to study this transition region in detail.

1.4 Low-mass star formation

The nearby molecular clouds in the Milky Way are sites of low-mass ($M_{star} < 2M_{\odot}$) star formation. The initial conditions and formation process of low-mass stars are of great interest as it relates very closely to the history of our own solar system. As low-mass protostars are more abundant in the solar neighbourhood, they are easier to study observationally than their higher mass counterparts. This is also aided by the fact that the evolutionary timescale for a low-mass star is much longer than their high-mass counterparts. The closest star-forming regions such as Ophiuchus and Taurus house many prestellar cores and *young stellar objects* (YSOs), which are progenitors of low-mass stars.

Figure 1.7 shows the different stages leading up to formation of a star. It highlights the evolution shown in the last three panels of Figure 1.5 in more detail. The progenitor prestellar core is very cold, $T \sim 10 - 20$ K, and radiates in far-infrared and sub-millimetre wavelengths. The evolutionary stages of the protostar are divided into *Classes* based on their observational characteristics (Lada 1987; Andre et al. 2000; Dunham et al. 2014). When the protostar is first formed, it is embedded in a dense envelope of material remaining from the core. Therefore,

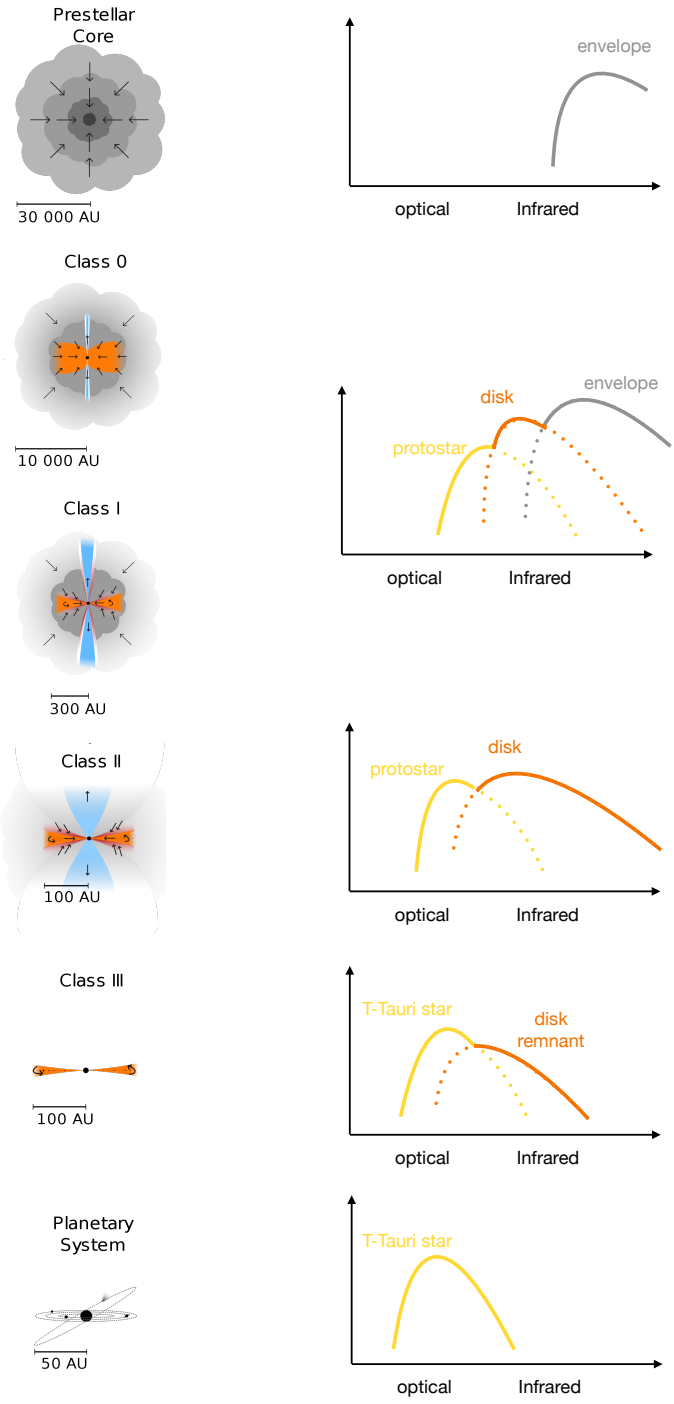

Figure 1.7: Schematic showing stages of star formation (*left*) and the typical spectral energy diagrams (*SED*) associated to each stage. The individual contributors to the black-body radiation are also shown. Credit for the left panel : Persson, Magnus Vilhelm. 2014. Current view of protostellar evolution. The SED diagrams are based on Lada (1987).

it is usually not visible in optical and NIR. Due to conservation of angular momentum, any amount of initial rotation in the collapsing core results in the formation of a disk surrounding the protostar. An outflow is often observed, usually orthogonal to the disk. A large accretion rate from the envelope onto the YSO is seen. This stage is referred to as the **Class 0** phase. The gravitational energy of the infalling material is released as heat, which is absorbed by the surrounding envelope. The envelope is efficiently cooled down by optically thin dust emission. The *accretion luminosity* is the energy that is absorbed by the envelope and then re-emitted at millimetre wavelengths. The protostar and the disk radiate in the near-infrared, but the spectral energy diagram (SED) of the system is still dominated by the envelope, which emits in the far-infrared. By the **Class I** phase, more material is accreted onto the star and the disk, the envelope becomes thinner, and the contribution from the star becomes more prominent. The YSO becomes visible in the NIR. When the envelope is completely dissipated, and the SED is comprised of the emission from the protostar and disk, we have the **Class II** phase. The protostar also accretes enough mass for the temperature to be high enough to radiate in optical. At this stage, the SED still has some infrared excess due to the disk. Gradually, the disk is cleared of gas and dust due to the formation of the planetary system, and the star becomes a classical T-Tauri star (**Class III**). At this stage, the IR-excess from the remnant of the disk is much lower relative to the emission from the star. Finally, we have the final star surrounded by the planetary system.

1.5 Observations of star formation

1.5.1 Radiative cooling processes in the ISM

The gas in the ISM, including the molecular cloud and cores, is constantly heated by energetic cosmic ray particles, interstellar radiation field and radiation from nearby massive stars. In molecular clouds and cores, this energy is lost mainly by two types of radiative processes. These are (i) black-body radiation by dust particles, and (ii) spectral line emission by molecules. We now look at both of these processes, the emissions due to which are generally used to observe molecular clouds and dense cores.

Black-body emission

The *radiative transfer equation* deals with the propagation of radiation from the source through the material (gas and dust) to the observer. As shown in Figure 1.8, if we consider the radiation to pass through a thin slab of material of width ds, then the change in the outgoing radiation, I_ν is due to the radiation being absorbed and re-radiated by the slab ds. Therefore, we have

$$\frac{dI_\nu}{ds} = -\rho\kappa_\nu I_\nu + j_\nu \,, \tag{1.12}$$

where the emission by the slab is given by its emissivity, j_ν. The absorption depends on the density, ρ, and the absorption coefficient, κ_ν. The emissivity and the absorption coefficient vary with the frequency of the radiation, ν.

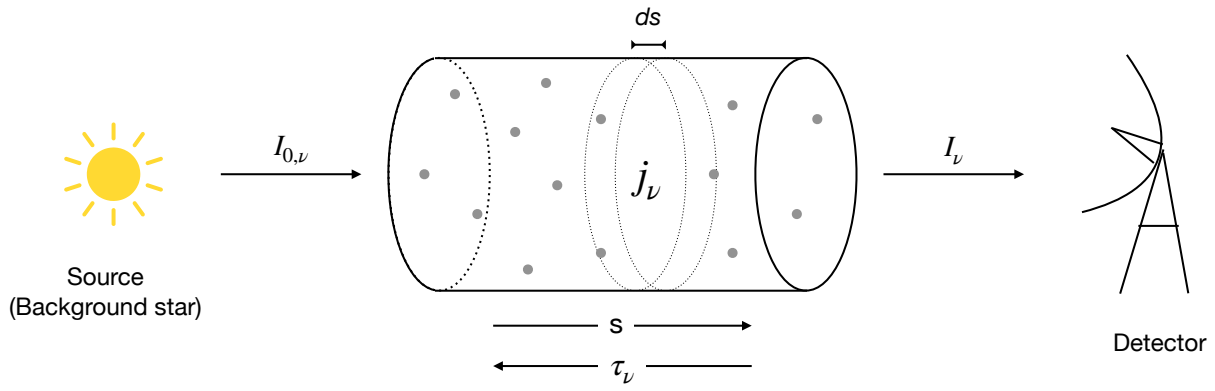

Figure 1.8: Radiation passing through a slab of gas in ISM. The optical depth, τ_ν increases (as seen by the observer) in the opposite direction of the distance passed by the ray through the slab, s. The ray passes through an slab of infinitesimal width, ds, of emissivity j_ν (see Section 1.5.1).

The optical depth, τ_ν of the medium refers to the total absorption in the line of sight, i.e.,

$$\tau_\nu = \int \rho \kappa_\nu ds \, . \tag{1.13}$$

The *source function,* S_ν , which is a characteristic property of the medium, is defined as the ratio of between its emissivity and absorption ($S_\nu \equiv j_\nu / \rho\kappa_\nu$). Equation 1.12 then becomes

$$\frac{dI_\nu}{d\tau_\nu} = \frac{1}{\rho\kappa_\nu}\frac{dI_\nu}{ds} = -I_\nu + S_\nu \, . \tag{1.14}$$

Integrating along optical depth of τ_ν gives us the emergent radiation flux, I_ν :

$$I_\nu = I_{0,\nu} e^{-\tau_\nu} + (1 - e^{-\tau_\nu}) S_\nu \, , \tag{1.15}$$

where, as denoted in Figure 1.8, $I_{0,\nu}$ is the radiation flux entering the medium.

In case of black-body radiation by dust particles, the emitted radiation is mostly at lower wavelengths than the incoming radiation. Hence, in Equation 1.15, the flux at emitted wavelengths is given by the source function, which is equal to the flux, $B_\nu(T)$, from a black-body at temperature T, i.e., $I_\nu = S_\nu = B_\nu(T)$. From *Planck's law*,

$$B_\nu(T) = \frac{2\nu^2}{c^2} \frac{h\nu}{e^{\frac{h\nu}{k_B T}} - 1} \, . \tag{1.16}$$

In the optically thin regime, the thermal dust emission can be approximated from Equation 1.15 and 1.16 as

$$I_\nu \approx B_\nu(T) \tau_\nu \, . \tag{1.17}$$

Then, the molecular column density $N(\mathrm{H_2})$ is related to τ_ν as

$$\tau_\nu = \kappa_\nu \mu_{\mathrm{H_2}} m_H N(\mathrm{H_2}) \, , \tag{1.18}$$

where $\mu_{\mathrm{H_2}}$ is the average mass per $\mathrm{H_2}$ molecule relative to hydrogen atom. Equation 1.18 gives a way to measure the column density in the line of sight through observation of dust continuum emission.

Molecular line emission

Molecules are excited through collisions due to the thermal motions of particles in the medium and via absorption of radiation. They are then de-excited collisionally or via the emission of radiation at characteristic frequencies. At the temperatures of molecular clouds, the molecules are usually excited to an upper level of their rotational and vibrational energies.

If n_u and n_l are the populations of molecules in the upper (u) and lower (l) energy states, with ΔE being the energy difference between the two states, then, Boltzmann's equation reads :

$$\frac{n_u}{n_l} = \frac{g_u}{g_l} e^{-\frac{\Delta E}{k_B T_{\rm ex}}} \ , \tag{1.19}$$

where $T_{\rm ex}$ is defined as the *excitation temperature* of the transition, and g_u and g_l are statistical weights of the two states for the transition. When considering the transition from u to l state via radiative cooling, their rate is given by Einstein's coefficient A_{ul}. In this process, a photon of frequency ν is emitted, such that $\Delta E = h\nu$. Then, considering the radiation to be uniform in the solid angle 4π, the emissivity j_ν in Equation 1.12 is given by

$$j_\nu = \frac{1}{4\pi} n_u A_{ul} \phi(\nu) \ , \tag{1.20}$$

where $\phi(\nu)$ is the probability of emission at frequency ν, which is the line profile, peaking strongly at $\nu_0 = \Delta E/h$. In this thesis, we use the inversion transitions of the ammonia molecule as the main observational tracer. This radiative transition is discussed in detail in Section 1.5.2.

1.5.2 NH_3 inversion transitions

The hyperfine structure of NH_3 inversion transitions (e.g. Figure 1.9) allows its individual components to remain optically thin at high column densities (Caselli et al. 2017a). Unlike carbon-bearing species, such as CO and HCO^+, NH_3 shows no depletion in single-dish observations at high densities and cold temperatures characteristic of cores (Bergin & Langer 1997). Even though the critical density of the transitions is a few times 10^3 cm^{-3}, NH_3 has been observed towards centres of dense cores, with typical densities of $10^5 - 10^6$ cm^{-3}. Therefore, NH_3 is an important high-density tracer of cold gas. To ensure direct and continuous measurements of the physical properties between different regions without introducing any more observational biases, it is essential to study them using the same tracer. As it allows for observation of a wide range of densities, NH_3 is also useful in the study of transition regions between core and cloud.

The molecular abundance of NH_3 relative to H_2 is $\sim 10^{-8}$ in dense cores (Tafalla et al. 2002; Crapsi et al. 2007). Ammonia is formed inside molecular clouds either in the gas phase via reaction between H_2 and N^+, or on the surfaces of the grains via repeated hydrogenation of nitrogen atoms. In diffuse gas, NH_3 is photo-dissociated by energetic photons, and hence not readily observed.

As shown in Figure 1.10, the NH_3 molecule is pyramid-shaped, with the three N-H bonds at an angle of approximately 107° with one another. The molecule rotates around its axis of symmetry (vertical in Figure 1.10), which can also precess around the axis. The rotational energy

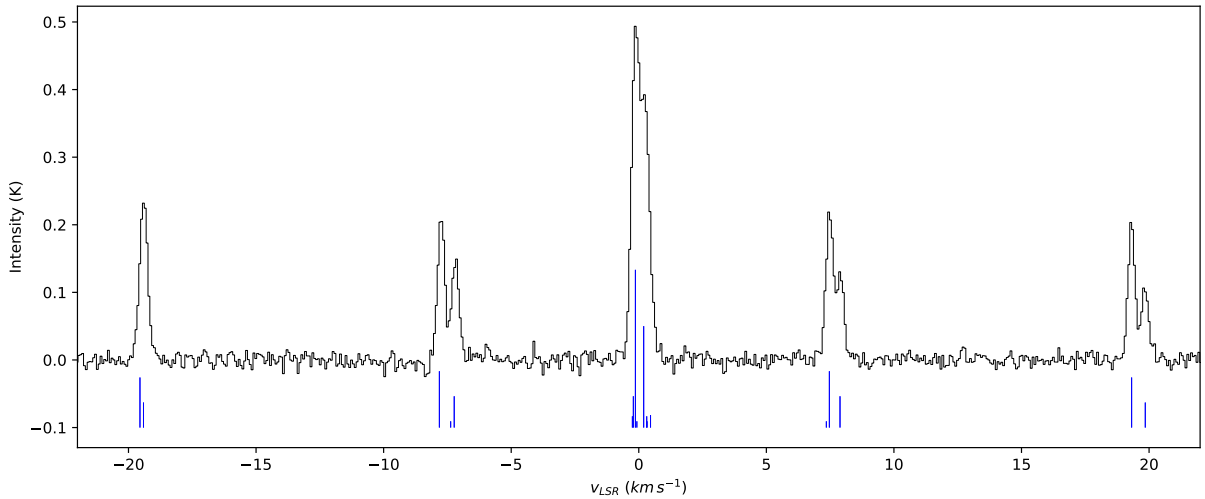

Figure 1.9: Observed spectrum for NH_3 (1,1) in L1688 (Chapters 2 and 3). The positions and the relative strengths of the different hyperfines are shown as blue vertical lines below the spectrum.

levels of the molecule are characterised by the total angular momentum, J and the projected angular momentum along the axis of symmetry, K. The $J > K$ energy states are short-lived, and the molecule quickly returns to the metastable $J = K$ states. Radiative transitions from one metastable state to another are forbidden, and therefore, the relative population of molecules at different metastable states are defined purely by thermal collision. Thus, the ratio of populations between two states could be used to accurately measure the kinetic temperature, $T_{\rm K}$of the gas. Each of the three hydrogen atoms possesses nuclear spin, and due to different possible relative orientations of their spins, NH_3 molecule can exist in two distinct forms: ortho-NH_3 (all H-spins are parallel, and $K = 3n$, where n is an integer) and para-NH_3 (one H-spin is anti-parallel, $K \neq 3n$). Therefore, among the metastable states, (3,3), (6,6), etc. are ortho-NH_3 and the (1,1), (2,2), (4,4), etc. are para-NH_3, where the states are represented as (J, K). Observationally, the first ortho state, (3,3), is difficult to observe in molecular clouds, as its excitation conditions require very high temperatures and densities (Ho & Townes 1983). Therefore, only the (1,1) and (2,2) lines are usually detected, and as both are para-NH_3, the ortho-para column density ratio is not constrained for these observations. Hence, an ortho-para ratio needs to be assumed to convert the para-NH_3 column density to the total NH_3 column density (see Chapters 2, 3, and 4).

The nitrogen atom in the NH_3 molecule can tunnel quantum-mechanically through the plane of the hydrogen atoms, causing an *inversion* of the molecule (Figure 1.10). As the nucleus of the nitrogen atom has a spin, this tunnelling causes the molecule to be in different orientations, with the nitrogen nuclear spin being parallel or anti-parallel to the geometry of the molecule. This splits the (J,K) states into *inversion doublets*, which are again split into multiple components due to interaction between nucleus moment and molecular rotation, and between atomic spins (see Figure 2 in Ho & Townes 1983). These split lines of the (J,K) inversion transitions are called *hyperfine components*. The (J,K)=(1,1) and (J,K)=(2,2) transitions have total of 18 and 21 hyperfine components, respectively. Some of the prominent hyperfine components of the NH_3

(1,1) spectrum are shown in Figure 1.9.

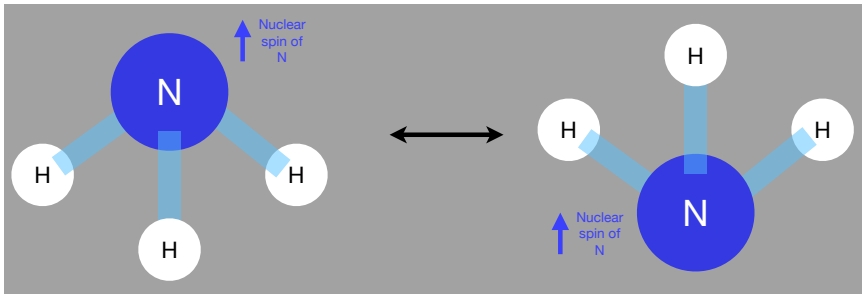

Figure 1.10: Schematic of the inversion transition of NH_3, between the two states where the nuclear spin of the nitrogen atom is parallel and anti-parallel to the direction of N with respect to the hydrogen atoms.

Using Equation 1.19, we can express the ratio between the column densities of the upper and lower energy levels of the (1,1) transition as

$$\frac{N_u}{N_l} = \frac{g_u}{g_l} e^{-\frac{h\nu_0}{k_B T_{\rm ex}}} , \tag{1.21}$$

where ν_0 is the frequency, and $T_{\rm ex}$ is the excitation temperature of the (1,1) transition. Then, the total column density (1,1) energy level is

$$N_{(1,1)} = N_l \left(1 + \frac{g_u}{g_l}\, e^{-\frac{h\nu_0}{k_B T_{\rm ex}}}\right) , \tag{1.22}$$

where N_l is the population in the lower level of (1,1). As radiative transitions between the states (1,1) and (2,2) are forbidden, the ratio of their populations can be used to derive the rotational temperature, T_{rot}, as

$$\frac{N_{(2,2)}}{N_{(1,1)}} = \frac{5}{3} e^{-\frac{T_0}{T_{rot}}} , \tag{1.23}$$

where the ratio between the statistical weights $g_i = (2J + 1)$ is 5/3, and $T_0 = 41.5\,\mathrm{K}$ is the temperature equivalent of the energy difference between the two states ($\Delta E = k_B T_0$). The rotational temperature corresponding the population ratios between (1,1) and (2,2) is related to the gas kinetic temperature, $T_{\rm K}$ as (Swift et al. 2005) :

$$T_{rot} = T_{\rm K} \left(1 + \frac{T_{\rm K}}{T_0}\, ln\left(1 + \frac{3}{5} e^{-\frac{15.7\,K}{T_{\rm K}}}\right)\right) \tag{1.24}$$

Thanks to the numerous hyperfine components, a single transition line allows for very accurate measurements of the gas kinematics. Barranco & Goodman (1998) observed dense cores with NH_3 hyperfine transitions and found the velocity dispersion inside those cores to be almost constant at a value only slightly higher than the thermal dispersion. Using NH_3 observations of a nearby core B5 in Perseus, Pineda et al. (2010) reported, for the first time, a direct observation of a sharp transition from turbulent ambient cloud to a coherent, subsonic dense core.

1.5.3 Single disk telescopes

The dish telescopes are one of the simplest radio telescopes. A single dish telescope consists of a primary parabolic reflector and a receiver. The basic components of a telescope are highlighted in Figure 1.11.

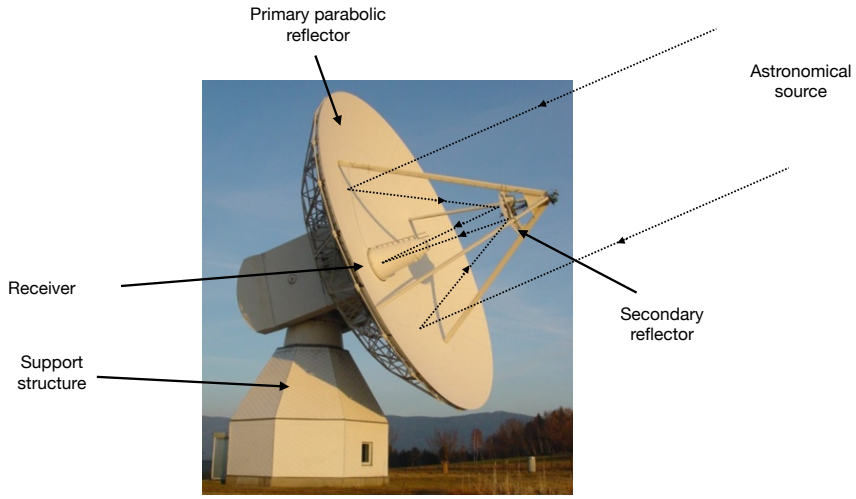

Figure 1.11: Components of a single-dish radio telescope. Shown here is the 20m telescope at Wettzell, Germany.

A key characteristic of a dish telescope is its beam pattern in the sky (shown in Figure 1.12), which consists of a *main lobe* and several *side lobes*, and denotes the directional receiving power (*gain*) of the telescope. The main lobe corresponds to the solid angle where the telescope is the most responsive. A high ratio between the main lobe and side lobe power is desired, as it corresponds to better directionality of the telescope. The width of the main lobe at half power, the *half power beam width* is called the **beam width**, θ_{MB}. The resolution of the telescope is also characterised by θ_{MB}, and

$$\theta_{MB} \sim \frac{\lambda}{D}\,, \tag{1.25}$$

where λ is the wavelength of observation, and D is the diameter of the dish. Therefore, a larger dish provides better resolution at the same wavelength. Equation 1.25 also highlights why radio telescopes need to be significantly larger than their optical counterparts (with much smaller λ) to achieve similar resolving power.

Another key parameter in single-dish observation is the **efficiency**, η of the telescope, which is the ratio between the received and measured energy flux. It depends on the quality of the reflective surface as well as the electronics of the receiver and other instruments used. For astronomical sources smaller with an angular size smaller than the main beam of the telescope, the **beam filling fraction**, which is the ratio between the angle subtended by the source and the beam width, becomes important to have an accurate measurement of the line emission.

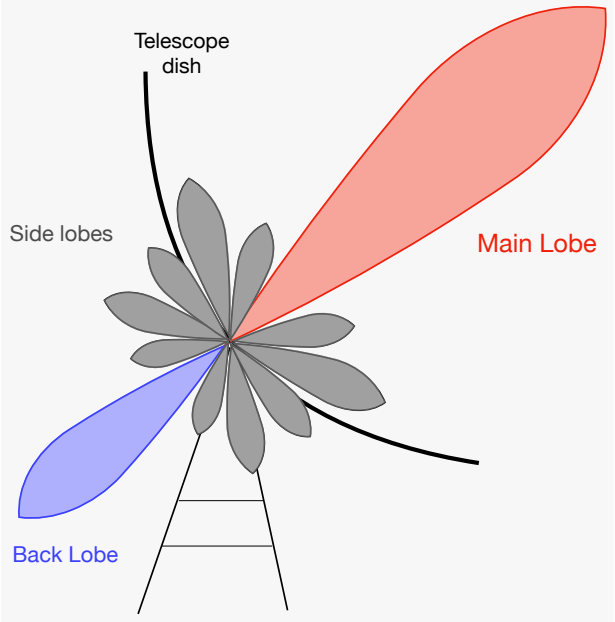

Figure 1.12: Schematic showing the antenna beam pattern for a single dish telescope

The total power received by the telescope is given in terms of the *system temperature*, T_{sys}, which is the temperature of a black body radiating equivalent power at that frequency, i.e.,

$$P_\nu = k_B T_{sys} \Delta\nu \,, \tag{1.26}$$

where P_ν is the power received by the telescope at frequency ν, $\Delta\nu$ is the *bandwidth*, the range of frequencies observed, and k_B is the Boltzmann's constant. For a typical observation, T_{sys} has contributions from different factors, giving

$$T_{sys} = T_A + T_{RX} + \eta \left(T_{bg} e^{-\tau} + T_{atm}(1 - e^{-\tau})\right) , \tag{1.27}$$

where T_A, the *antenna temperature* is the contribution from the astronomical source, and T_{RX}, T_{bg}, and T_{atm} are temperatures of the receiver noise, background sources and the earth's atmosphere, respectively. As previously defined, η is the telescope efficiency, and τ is the opacity of the atmosphere in the direction of the source. Therefore, to separate the source contribution, T_A, it becomes necessary to do *on* and *off* observations, i.e., towards the source, and away from the source, respectively, giving $T_A = T_{on} - T_{off}$. The antenna temperature is further corrected for atmospheric attenuation, and we have $T_A^* = T_A\, e^{-\tau}$. This atmosphere-corrected term is related to the source *brightness temperature,* T_B as

$$T_A^* = \frac{\eta}{\lambda^2} \int_{4\pi} A_e T_B d\Omega \,, \tag{1.28}$$

where $A_e = \lambda^2/\Omega_B$ is the effective aperture of the beam and Ω_B is the solid angle subtended by the beam. The integral is calculated over the total solid angle, 4π. The brightness temperature

is defined as the temperature of a black body with radiative intensity equivalent to that of the source,

$$T_B = \frac{\lambda^2}{2k_B} I_\nu \,, \tag{1.29}$$

where λ and ν are the wavelength and frequency of the observation, respectively, and I_ν is the source intensity at the telescope.

Mainly two types of receivers are used in radio telescopes. *Bolometers* measure the incident flux using a temperature-dependent resistor, whose resistance is proportional to the absorbed energy. Therefore, bolometers measure the total flux and do not retain the phase information of the incident radiation. In contrast, *heterodyne receivers* preserve the phase information by combining the input frequency with the known frequency of a *local oscillator, LO*. This data could be then used to obtain the spectra (e.g. of a molecular transition), which in turn provides information regarding the kinematics of the observed region (similar to the work presented in this thesis).

1.6 Contents of this thesis

In this section, we summarise the contents of the following chapters.

In Chapter 2, we discuss the detection of a supersonic cloud component towards the coherent cores of the molecular cloud L1688 in Ophiuchus. We use NH_3 data from the Green Bank Ammonia Survey (GAS) and stack the spectra to obtain unprecedented high sensitivity. Thus, we detect, and thereby account for, the supersonic cloud component in the spectra towards the subsonic cores. We show that not being able to disentangle the cloud component from the core spectra leads to a systematic overestimate of the kinetic temperature and the velocity dispersion of the core. This, in turn, affects the estimated physical structure and stability of the cores.

Chapter 3 presents a closer look at the physical properties, such as temperature, velocity dispersion, and abundance, accompanying the transition to coherence observed at the boundaries of cores in L1688. Using NH_3 data, we present, for the first time, a map of kinetic temperature towards dense cores and their natal molecular cloud using the same density tracer. We employ a multi-component analysis using stacked spectra towards the neighbourhood of coherent core to show the transition to coherence to be gradual, in contrast to previous results. For the first time, we also detect subsonic material outside coherent cores, suggesting subsonic material that could be accreted by the cores and possible substructures connecting the cores to the cloud.

In Chapter 4, we present our findings in the subsonic core Barnard 5 in Perseus, with combined observations using the Green Bank Telescope and the Very Large Array. We focus on the two filaments inside the subsonic core of B5 and employ multi-component analysis to study the velocity structure in the core. We detect two components towards the filaments, showing signs of infall. We also detect two additional components which could show material falling into B5 from the cloud. We also show that the two filaments were likely formed in a gravity-dominated collapse, as opposed to turbulent-driven compression.

Finally, Chapter 5 gives a summary of the work presented in this thesis and presents possible follow-ups to the results of these projects.

Chapter 2

Ubiquitous NH_3 supersonic component in L1688 coherent cores

The contents of this chapter were published in Astronomy & Astrophysics Journal. Credit: Choudhury et al., A&A, 640, L6, 2020, reproduced with permission © ESO

2.1 Abstract

Context. Star formation takes place in cold dense cores in molecular clouds. Earlier observations have found that dense cores exhibit subsonic non-thermal velocity dispersions. In contrast, CO observations show that the ambient large-scale cloud is warmer and has supersonic velocity dispersions.
Aims. We aim to study the ammonia (NH_3) molecular line profiles with exquisite sensitivity towards the coherent cores in L1688 in order to study their kinematical properties in unprecedented detail.
Methods. We used NH_3 (1,1) and (2,2) data from the first data release (DR1) in the Green Bank Ammonia Survey (GAS). We first smoothed the data to a larger beam of 1′ to obtain substantially more extended maps of velocity dispersion and kinetic temperature, compared to the DR1 maps. We then identified the coherent cores in the cloud and analysed the averaged line profiles towards the cores.
Results. For the first time, we detected a faint (mean NH_3(1,1) peak brightness <0.25 K in T_{MB}), supersonic component towards all the coherent cores in L1688. We fitted two components, one broad and one narrow, and derived the kinetic temperature and velocity dispersion of each component. The broad components towards all cores have supersonic linewidths ($\mathcal{M}_S \geq 1$). This component biases the estimate of the narrow dense core component's velocity dispersion by ≈28% and the kinetic temperature by ≈10%, on average, as compared to the results from single-component fits.
Conclusions. Neglecting this ubiquitous presence of a broad component towards all coherent cores causes the typical single-component fit to overestimate the temperature and velocity dispersion. This affects the derived detailed physical structure and stability of the cores estimated

from NH_3 observations.

2.2 Introduction

Star formation takes place in dense cores, which are embedded in molecular clouds. These cores in various molecular clouds are therefore studied in detail in relation to their physical and chemical properties. Across different molecular clouds, the star-forming cores are characterised by higher density and lower temperatures, as compared to the parental cloud (Myers 1983; Myers & Benson 1983; Caselli et al. 2002). When studied using molecular transitions tracing higher densities ($n(H_2) > 10^4$ cm^{-3}), the cores are revealed to show subsonic levels of turbulence (Barranco & Goodman 1998; Kirk et al. 2007; Rosolowsky et al. 2008). This is in contrast to lower density gas surrounding the cores, which show supersonic linewidths (Goodman et al. 1998).

Thanks to the numerous hyperfine components, NH_3 remains optically thin in the individual components even at high column densities (see Caselli et al. 2017b), thereby making it an important and useful tracer of cold and dense gas. Barranco & Goodman (1998) studied four cores in NH_3 (1,1) emission, and found that the linewidths within the cores were roughly constant and slightly greater than the pure thermal value. They called these 'coherent cores'. A 'transition to coherence' from the turbulent environment to the coherent region was hypothesised (Goodman et al. 1998), but not directly observed. Williams & Myers (2000) also noted eight 'quiescent' cores, which they defined as local minima in non-thermal dispersion, in the observation of Serpens in N_2H^+, using BIMA (Berkeley Illinois Maryland Association). They showed that the dispersion increased outwards from the centres of these cores. Using NH_3 (1,1) observations with the Green Bank Telescope, Pineda et al. (2010) studied the transition from the surrounding gas to inside a core, for the first time in the same tracer in the B5 region in Perseus, and reported a sharp transition to coherence (a decrease in the velocity dispersion by a factor of 2 within 0.04 pc). This suggests that we can define the boundaries of coherent cores in a systematic fashion, as regions with subsonic non-thermal linewidths (see also Chen et al. 2019). It should be noted that this definition of cores does not necessarily define cores identically to those defined using continuum emission. Therefore, not all of the 'coherent cores' have continuum counterparts.

In the Green Bank Ammonia Survey (GAS; Friesen et al. 2017), star forming regions in the Gould Belt were observed using NH_3 hyperfine transitions. The first data release (DR1) includs the following four regions in nearby molecular clouds: B18 in Taurus, NGC 1333 in Perseus, L1688 in Ophiuchus, and Orion A North. Using the results from this survey and H_2 column densities derived from Herschel data, Chen et al. (2019) identified 12 coherent structures (termed 'droplet' in the paper) in L1688 and six in B18. They observed that these droplets show high gas density ($\langle n_{H_2} \rangle \approx 5 \times 10^4$ cm^{-3}, derived from their masses and radii) and near-constant, almost-thermal velocity dispersions, with a sharp velocity dispersion increase across the boundary.

This letter presents a new analysis of the GAS DR1 observations to reach unprecedented noise levels towards coherent cores and reveal a broad supersonic component that has been previously unidentified. We focus on L1688, which is part of the Ophiuchus molecular cloud (distance = 138.4±2.6 pc, Ortiz-León et al. 2018, and mass ~980 $M_\odot$, Ladjelate et al. 2020a) because it is one of the nearest star-forming regions and with the most extended NH_3 emission beyond

cores among the GAS DR1 regions.

2.3 Ammonia maps

We use the NH_3 (1,1) and (2,2) maps from GAS DR1 (Friesen et al. 2017). The observations were carried out using the Green Bank Telescope (GBT) to map NH_3 emission in the star-forming regions in the Gould Belt with A_V >7 mag using the seven-beam K-Band Focal Plane Array (KFPA) at the GBT. Observations were performed in frequency switching mode with a frequency throw of 4.11 MHz ($\approx$ 52 km s^{-1}at 23.7 GHz). The spectral resolution of the data is 5.7 kHz, which corresponds to $\approx$ 72.1 ms^{-1}at 23.7 GHz (i,e, the approximate frequency of observations). The extents of the maps were selected using continuum data from Herschel or JCMT, or extinction maps derived from 2MASS (Two Micron All Sky Survey). To convert the spectra from frequency to velocity space, the rest frequencies for NH_3 (1,1) and (2,2) lines were considered to be 23.6944955 GHz and 23.7226336 GHz, respectively.

The parameter maps of L1688, which were released in DR1, are very patchy, particularly for the kinetic temperature. Therefore, to obtain a good estimate of the Mach number throughout the cloud, which requires determining the temperature, and thus, a good detection of the (2,2) line, the data were smoothed by convolving them to a beam of 1′ (GBT native beam at 23 GHz is $\approx$31″). The data cube was then re-gridded to avoid oversampling. The relative pixel size was kept the same as in the original GAS maps, at one-third the beam width. The median noise level achieved as a result is 39 mK in the regions of interest (see Sections 2.4.2 and 2.4.3). In comparison, the median noise in the same regions was 131 mK in the original GAS DR1 maps.[1]

2.4 Analysis

2.4.1 Line fitting

We fitted NH_3 line profiles to the data with the `pyspeckit` package (Ginsburg & Mirocha 2011), which uses a forward modelling approach, following the process described in Friesen et al. (2017). The range in velocity to fit is determined from the average spectrum of the entire region (Figure A.1). Since the ortho-to-para ratio in the region is not known, we only used the p-NH_3 column density in the fitting process, and did not attempt to convert it to total NH_3 column density[2].

The model produces synthetic spectra based on initial guesses provided for the input parameters: excitation temperature ($T_{\rm ex}$), kinetic temperature ($T_{\rm K}$), para-ammonia column density (N(p-NH_3)), velocity dispersion ($\sigma_{\rm v}$), and line-of-sight central velocity ($v_{\rm LSR}$) of the gas (Section 3.1 in

[1]The GAS data use a tapered Bessel function as the gridding kernel (advocated for by Mangum et al. 2007a), to achieve maximum resolution. The kernel is not strictly positive, which leads to adjacent pixels having anti-correlated noise. When smoothing over anti-correlated values, the noise level drops faster than what is expected from independent data. Therefore, we see the noise level drop faster than the inverse of the beam radius.

[2]To compare N(p-NH3) to the total NH_3 column densities reported in other works, an easy conversion is to multiply it by two, with the ortho-to-para ratio assumed to be unity.

Friesen et al. 2017). A non-linear gradient descent algorithm, MPFIT (Markwardt 2009) is then used to determine the best-fit model, and the corresponding values of the parameters. A good set of initial conditions is necessary to ensure that the non-linear least-squares fitting does not get stuck in a local minimum. The value of v_{LSR} is critical, and, therefore, we used the first-order moments of the (1,1) line as initial guesses. The second-order moments were used as guesses for velocity dispersion. For the other parameters, we used guesses based on the GAS DR1 map of the respective parameter. The initial guesses used in our work are: $\log_{10}(N_{p-NH_3}/cm^{-2}) = 14$, $T_K = 20\,K$, and $T_{ex} = 5\,K$. These numbers are within the range of the values reported in the GAS DR1 maps, and therefore, they are reasonable guesses. As a test, we checked the fits with varying guesses and determined that the exact values of the initial parameters did not affect the final results, as long as they were within a reasonable range.

In this work, we use the `cold_ammonia` model in the `pyspeckit` library, which makes the assumption that only the (1,1), (2,2) and (2,1) levels are occupied. It is also assumed that the excitation temperature, T_{ex}, is the same for the (1,1) and (2,2) transitions, as well as their hyperfine components.

2.4.2 Identification of coherent cores

To study the spectra towards cores, we first define 'coherent cores' as the region with a sonic Mach number < 1 and larger than a beam (similar to Pineda et al. 2010; Chen et al. 2019)[3]. The sonic Mach number, $\mathcal{M}_S$, is defined as the ratio of the non-thermal velocity dispersion, σ_{NT} (see Appendix A.1) to the sound speed in the medium,

$$\mathcal{M}_S = \frac{\sigma_{NT}}{c_S}\,, \tag{2.1}$$

where c_S is the one-dimensional sound speed in the gas,

$$c_S = \sqrt{\frac{k_B T_K}{\mu_{gas}}}\,. \tag{2.2}$$

Here k_B is the Boltzmann's constant, T_K is the kinetic temperature in the region, and $\mu_{gas} = 2.37$ amu is the average molecular mass (Kauffmann et al. 2008).

Based on this definition, we identify 12 regions in L1688 as coherent cores. They are shown in Figure 2.1. See Appendix A.2 for a brief description of the cores.

2.4.3 Averaging spectra towards the coherent cores

We first averaged the spectra towards each coherent core defined in Section 2.4.2, to get a higher signal-to-noise ratio. To avoid any possible line broadening due to averaging in a region with velocity gradients, we aligned the spectra at each pixel within a core before averaging. We took

[3]It should be noted that Chen et al. (2019) also require a corresponding peak in $N(H_2)$ inside a coherent region for it to be identified as a 'droplet', whereas we consider the sonic Mach number as the only criterion.

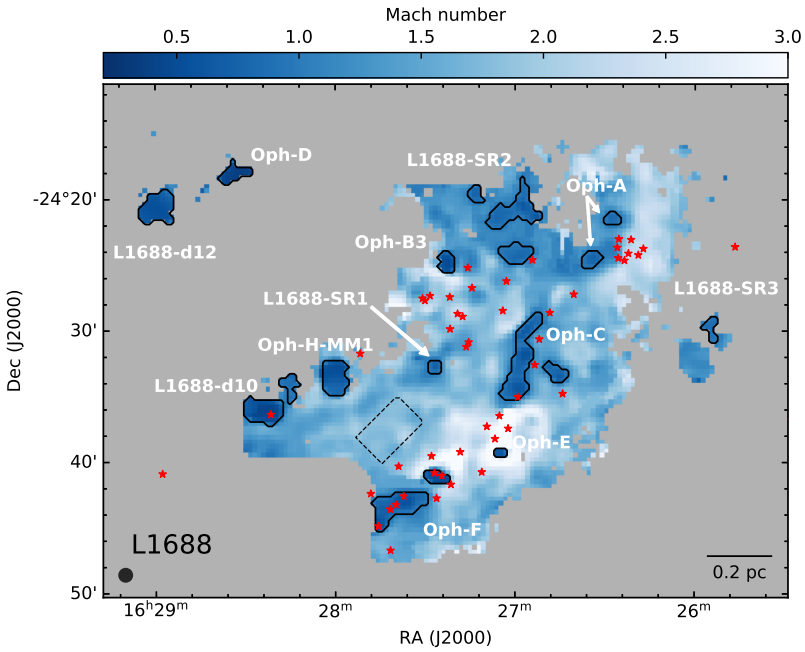

Figure 2.1: Coherent cores, as defined in Section 2.4.2, are shown by black contours. The background colour scale shows the sonic Mach number. The dashed rectangle shows the box considered to be representative of the ambient cloud. The red stars show positions of Class 0/I and flat-spectrum protostars in the cloud (Dunham et al. 2015). The beam and the scale bar are shown in the bottom left and bottom right corners, respectively.

the velocity at a pixel, which was determined from the single-component fit at that pixel, and using the `channelShift` function from module `gridregion` in the GAS pipeline[4], we shifted the spectra by the corresponding number of channels. Then, we averaged the resultant spectra from all pixels inside a core, which are now essentially aligned at v=0. This averaging allowed us to reach a typical noise level of 18 mK in the average spectra, which is almost seven times better than the median noise level of 131 mK in the individual spectra towards the cores in the original GAS maps.

We checked if smoothing the data (Section 2.3) before averaging had any effect on the results and found that the change is not significant. See Appendix A.3 for details.

2.5 Results

2.5.1 Presence of a second component in core spectra

The top panels in Figure 2.2 show the average spectra in the Oph-F core, with a single-component fit (see Appendix A.4 for the guesses used in the fit process), and corresponding residual. Oph-

[4]https://github.com/GBTAmmoniaSurvey/GAS/tree/master/GAS

F is shown here as an example, the average spectra for the other coherent cores are shown in Appendix A.7 (Figures A.2 to A.12). From the residuals, it is evident that the fit does not recover all of the flux at the positions of the hyperfine lines. In particular, the single-component fit misses the flux present in a broad component, which is ubiquitously present towards all cores.

Therefore, we added a second component to the fit (see Appendix A.4 for the fit procedure). The resultant two-component fits and the individual components for Oph-F are shown in the bottom panel of Figure 2.2, and in Figures A.2 to A.12 for the other cores. The two-component fit is clearly an improvement (better χ^2), as seen from the respective residuals. We employed the Akaike Information Criterion (AIC, see Appendix A.5) to verify that for each core, considering a second component corresponds to a significant improvement in the fit to the spectra. The difference in AIC values from single-component fits to two-component fits, $\Delta_{\rm AIC} = {\rm AIC}_{1-{\rm comp.}} - {\rm AIC}_{2-{\rm comp.}}$, are shown in Table A.1.

In model comparison, the model with the lowest AIC value is the preferred one, and, therefore all regions are better fit by a two-component fit. However, for coherent cores L1688-d12 and L1688-SR3, the value of $\Delta_{\rm AIC}$ is small (see Table A.1) and the average spectra fits (Figures A.9 and A.12) only show marginal improvements with the two-component fit. Therefore, we note that these two regions are better fit with a two-component model, but their fit-derived results are not as well-constrained as in the other ten coherent cores.

The kinetic temperatures, velocity dispersions, LSR velocities, and p-NH_3 column densities for the single-component fits and for each individual component in the two-component fits are shown in Table A.1. We see that one of the two components is subsonic ($\mathcal{M}_S < 1$) across all cores, whereas the other component has $\mathcal{M}_S \geq 1$. We refer to the subsonic and supersonic components as 'narrow' and 'broad' components, respectively.

We note that the residuals from the two-component fit in some cores, in particular Oph-E, might suggest the presence of a third component or a non-Gaussian component. However, we do not see this towards all of the cores. Even when this occurs, the indication is not very clear : residuals comparable to the noise or not more than one or two channels wide. Therefore, we did not fit more than two components to the spectra in the cores.

2.5.2 Detection of a broad component in cores

A narrow and a broad component of ammonia emission has been detected in all of the coherent cores in L1688 (Figure 2.1). The broad component in the cores is fainter, with a mean (1,1) peak brightness temperature (T_p) $\approx$0.25 K and $T_{p,(2,2)} <$ 0.13 K, except in Oph-A ($T_{p,(2,2)} \approx$0.27 K) and Oph-C ($T_{p,(2,2)} \approx$0.16 K). Because of such low intensities, this component cannot be detected from the previous ammonia maps. As a comparison, the original GAS maps had noise levels of $\approx$131 mK in the coherent core regions, which is not low enough for a 3σ detection of the (1,1), and in most cases, this is comparable to the T_{MB} of the broad component in the (2,2). Therefore, using the original GAS data, one would not be able to detect the broad component, and the temperature and linewidth of the narrow core component would be affected. As can be seen in Table A.1, the mean noise level in the average spectra in the cores is $\approx$18 mK in this work, enabling us to comfortably fit even the faint broad component in these spectra for both (1,1) and (2,2).

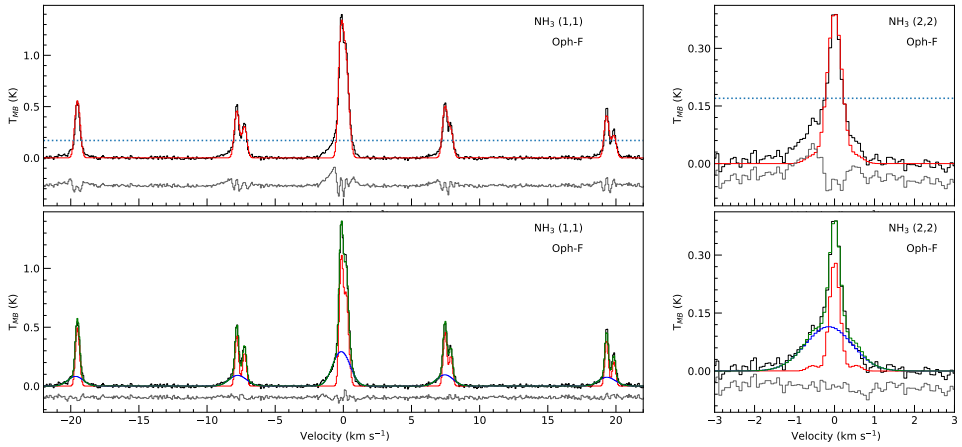

Figure 2.2: *Top panels* : Average NH_3 (1,1) and (2,2) spectra of Oph-F core, with a single-component fit. The blue-dotted line shows the median noise level in Oph-F in the original GAS data, which clearly shows that the broad component cannot be detected in the individual spectra in GAS DR1 data. *Bottom panels* : Same spectra, with two-component fit (green). The narrow (red) and broad (blue) components are also shown separately.

2.5.3 Spectra in the ambient cloud outside cores

To check if the two components, which are seen towards the coherent cores, are present throughout L1688, we looked at the spectra outside of the cores. Since the spectra outside of the cores are even fainter than those inside of them, we have to consider the average spectra in a small region, away from the cores. Therefore, we defined a rectangular box (shown by the black-dashed box in Figure 2.1) that is representative of the ambient cloud in L1688, as :

- being at least two beams away from any coherent cores, to avoid contamination from the core spectra;
- not including, or being very close($\lesssim$ one beam) to known protostars; and
- being away from the western edge of the cloud, which is affected by a strong external illumination (Habart et al. 2003).

The top panels of Figure 2.3 show the average spectrum in the ambient cloud with a single-component fit. Even when a two-component fit was attempted, we did not see a narrow component (bottom panel of Figure 2.3). AIC indicates that the two-component fit is a better model, with both components being supersonic (Mach number >1). Therefore, we conclude that these are two broad components in the ambient cloud, which are separated in centroid velocity by $\approx$0.6 km s^{-1}. The two components in the spectra have equal dispersions of 0.35 km s^{-1}. The kinetic temperatures of these two components are also approximately equal, 16.9 $\pm$ 0.2 K and 17.0 $\pm$ 0.5 K. These values are comparable to those from the broad components in the cores, and higher than the typical temperature of the narrow components. The Mach numbers of these two cloud components are comparable to that of the broad components seen in the cores (Table A.1).

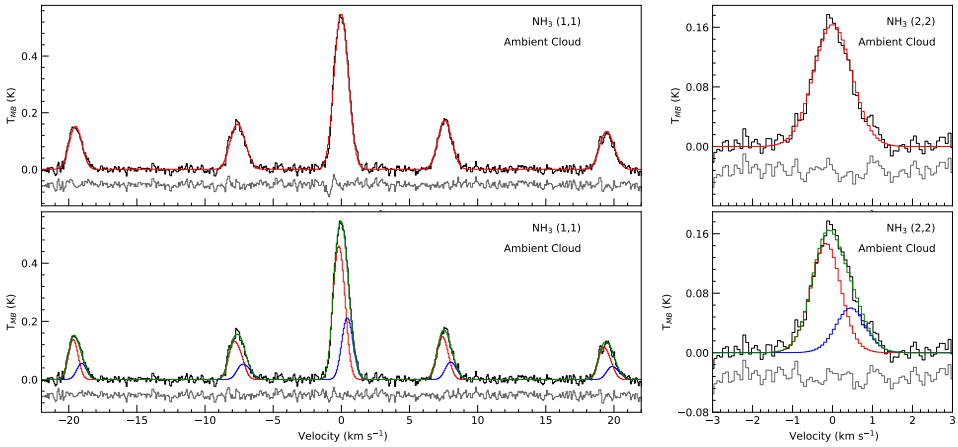

Figure 2.3: *Top panels:* Average spectra of ambient cloud (defined in Section 2.5.3) with a single-component fit. *Bottom panels:* Same spectra, with two-component fit (green). The individual components are shown separately in red and blue.

The residuals from the single-component fit to the ambient cloud spectra are not as suggestive as in the cores. Therefore, the single-component model can also be considered as a reasonable fit. Even then, the comparison between the ambient cloud and the broad component towards the cores, as mentioned above, remains the same. The temperature, velocity dispersion, and the Mach number in the ambient cloud, from a single-component fit, are very similar to those in the broad component in the coherent cores.

2.5.4 Comparison of physical parameters determined from the fit

Figure 2.4 shows the comparison between kinetic temperature, velocity dispersion, Mach number, and non-thermal dispersion in the coherent cores, from a single-component fit, and for the narrow component in the two-component fit. Clearly, a single-component fit significantly overestimates all of these parameters in all cores. The kinetic temperature from the narrow component is lower by 1.19±0.07 K, compared to the single-component fit. Similarly, the velocity dispersion of the narrow component is lower by an average[5] of 0.0332± 0.0007 km s^{-1}. The difference is as high as ≈0.1 km s^{-1}in the case of SR1. On average, the single-component fit overestimates the kinetic temperature by 10% and the velocity dispersion by 28%, as compared to the narrow component. Correspondingly, the Mach number is overestimated, on average, by 32%, and the non-thermal dispersion is typically overestimated by 39%.

The average kinetic temperatures and velocity dispersions inside the cores in the GAS DR1 parameter maps, which were obtained using single-component fits, are very similar to the single-component results we report. Therefore, the aforementioned comparison with narrow component results still holds, if the DR1 results (final two columns in Table A.1) are considered. On average, the GAS DR1 results show a 14% overestimate in T_K and a 34% overestimate in σ_v, as compared

[5]Weighted averages of ΔT_K and $\Delta\sigma_v$.

to our narrow component results.

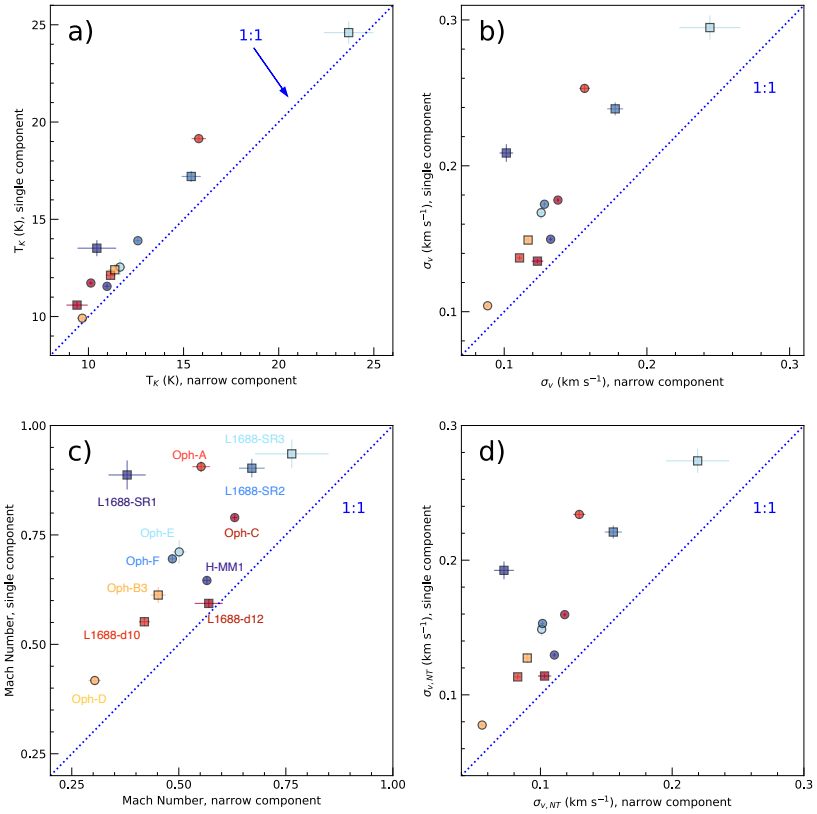

Figure 2.4: Kinetic temperature, velocity dispersion, Mach number and non-thermal dispersion in the cores, from single-component fits, and for the narrow component of a two-component fit, are shown in panels a, b, c and d, respectively. In the cases where the error bar is not visible, the error is smaller than the symbols.

2.6 Discussion and conclusions

For the first time, a faint, broad component has been detected towards coherent dense cores. When we consider a two-component fit to the spectra, it enables us to measure the velocity dispersion and kinetic temperature of the coherent core more accurately. We find that the typically-used single-component fit towards dense cores overestimates their temperatures and dispersions, on average, by 10% and 28%, respectively.

The 1.2 K systematic offset in temperature in the cores derived from the single-component fit is important, as it is comparable to the temperature drop observed towards the centre of the cores when compared to the outer 1′ or 2′ (Crapsi et al. 2007; Harju et al. 2017). This decreased temperature of the cores has an effect on the chemistry inside the cores (Caselli & Ceccarelli 2012; Bergin & Tafalla 2007), since, at the volume densities of L1688 dense cores ($\sim 10^5$ cm^{-3}),

gas and dust are thermally coupled (Goldsmith 2001) and surface chemistry rates exponentially depend on the dust temperature (see Hasegawa et al. 1992).

Without the detection of the faint broad component, both the temperature and velocity dispersion in the cores are overestimated. This changes the estimates of the dynamical stability for the cores.

In the ambient cloud surrounding the coherent cores, we do not see the narrow component. Instead, at the position of our 'ambient cloud box' (Figure 2.1), we see two broad components that are $\approx$0.6 km s^{-1}apart in centroid velocity, with equal temperatures and velocity dispersions. This might suggest the presence of two molecular clouds at slightly different velocities, which are probably merging at the location of L1688. The collision between these two clouds might result in a local density increase, where the narrow features are produced following a corresponding dissipation of turbulence, thus creating the observed coherent cores with subsonic linewidths.

On the other hand, if the faint broad features seen towards the coherent core position trace the less dense and more turbulent cloud along the line of sight of the coherent core, then we can measure the relative motions between the cores and the cloud in a direct way. Accordingly, we measured the relative velocity between the narrow and broad component, $\delta v_{(n-b)}$. Two-thirds of the coherent cores show subsonic $|\delta v_{(n-b)}|$ values, which suggests that most cores are dynamically coupled to their natal cloud (Kirk et al. 2010). The standard deviation of $\delta v_{(n-b)}$ is 0.35 km s^{-1}, which is lower than the broad component's typical velocity dispersion (0.48 km s^{-1}). Therefore, the motions of the cores are lower than the typical motions in the surrounding gas (see also Walsh et al. 2007; Kirk et al. 2007, 2010). Bailey et al. (2015) have also reported similar findings in simulated observations.

The cloud velocity dispersions that we derived from NH_3 are lower than those obtained using lower density tracers (CO) in the earlier studies. Therefore, the results from lower density tracers might overestimate the local degree of turbulence in the cloud, or NH_3 based measurements provide a strict lower bound to it.

Without the required sensitivity in the observations, the faint broad component is not detected, and, therefore cannot be considered in the fit. This causes both the kinetic temperature and the velocity dispersion in the cores to be overestimated. Therefore, our results suggest that with deeper observations, we obtain better estimates of the core properties.

Chapter 3

Transition from coherent cores to surrounding cloud in L1688

The contents of this chapter were published in Astronomy & Astrophysics Journal. Credit: Choudhury et al., A&A, 648, A114, 2021, reproduced with permission © ESO

3.1 Abstract

Context. Stars form in cold dense cores showing subsonic velocity dispersions. The parental molecular clouds display higher temperatures and supersonic velocity dispersions. The transition from core to cloud has been observed in velocity dispersion, but temperature and abundance variations are unknown.
Aims. We aim to measure the temperature and velocity dispersion across cores and ambient cloud in a single tracer to study the transition between the two regions.
Methods. We use NH_3 (1,1) and (2,2) maps in L1688 from the Green Bank Ammonia Survey, smoothed to $1'$, and determine the physical properties by fitting the spectra. We identify the coherent cores and study the changes in temperature and velocity dispersion from the cores to the surrounding cloud.
Results. We obtain a kinetic temperature map extending beyond dense cores and tracing the cloud, improving from previous maps tracing mostly the cores. The cloud is 4-6 K warmer than the cores, and shows a larger velocity dispersion ($\Delta\sigma_v$ = 0.15-0.25 km s^{-1}). Comparing to *Herschel*-based dust temperatures, we find that cores show kinetic temperatures that are $\approx$1.8 K lower than the dust temperature, while the gas temperature is higher than the dust temperature in the cloud. We find an average p-NH_3 fractional abundance (with respect to H_2) of (4.2±0.2) $\times10^{-9}$ towards the coherent cores, and (1.4±0.1) $\times10^{-9}$ outside the core boundaries. Using stacked spectra, we detect two components, one narrow and one broad, towards cores and their neighbourhoods. We find the turbulence in the narrow component to be correlated with the size of the structure (Pearson-r=0.54). With these unresolved regional measurements, we obtain a turbulence–size relation of $\sigma_{v,NT} \propto r^{0.5}$, which is similar to previous findings using multiple tracers.

Conclusions. We discover that the subsonic component extends up to 0.15 pc beyond the typical coherent boundaries, unveiling larger extents of the coherent cores and showing gradual transition to coherence over ~ 0.2 pc.

3.2 Introduction

Star formation takes place in dense cores in molecular clouds. Detailed studies of dense cores unveil their physical and chemical properties, which provide the initial conditions in the process of star formation. Across different molecular clouds, the star-forming cores are characterised by higher density and lower temperatures compared to the ambient cloud. Many of the cores also exhibit subsonic turbulence. However, the transition from core to cloud is still not well-understood.

The hyperfine structure of NH_3 inversion transitions allows its individual components to remain optically thin at high column densities (Caselli et al. 2017a). Unlike carbon-bearing species, such as CO and HCO^+, NH_3 shows no depletion at high densities and cold temperatures characteristic of cores (Bergin & Langer 1997). Therefore, NH_3 is an important and useful high-density tracer of cold gas. Using NH_3 (1,1) line emission, Barranco & Goodman (1998) found that the line width inside the four cores studied was roughly constant, and slightly greater than the pure thermal value. These latter authors also reported that at the edge of the cores, the line widths begin to increase. By analysing the cores and their environments, Goodman et al. (1998) suggested that a transition to coherence might mark the boundaries of the dense cores. Using NH_3 (1,1) observations with the Green Bank Telescope, Pineda et al. (2010) studied the transition from inside a core to the surrounding gas, for the first time in the same tracer, and reported a similar, but sharper transition to coherence (an increase in the dispersion by a factor of two in a scale less than 0.04 pc) in the B5 region in Perseus. However, the exact nature of the transition from the subsonic cores to the surrounding molecular cloud is not well known. It is important to study these transition regions, as this could give us clues on how dense cores form and accrete material from the surrounding cloud.

In the Green Bank Ammonia Survey (GAS, Friesen et al. 2017), star-forming regions in the Gould Belt were observed using NH_3 hyperfine transitions. Their first data release included four regions in nearby molecular clouds: B18 in Taurus, NGC1333 in Perseus, L1688 in Ophiuchus, and Orion A North. Using the results from this survey and H_2 column densities derived with *Herschel*, Chen et al. (2019) identified 18 coherent structures (termed 'droplet') in L1688 and B18. These latter authors observed that these droplets show gas at high density ($\langle n_H \rangle \approx 5 \times 10^4$ cm^{-3}; from masses and effective radii of the droplets, assuming a spherical geometry) and near-constant, almost-thermal velocity dispersion, with a sharp transition in dispersion around the boundary.

The results from Pineda et al. (2010) and Chen et al. (2019) suggest that we can define the boundaries of coherent cores systematically as the regions with subsonic nonthermal line widths. It is to be noted that this approach does not necessarily define cores in the same way as when using continuum emission. Therefore, not all of the 'coherent cores' will have continuum counterparts.

The temperature profile inside cores has been studied, and the cores are found to be usually at a temperature ≈10 K (e.g., Tafalla et al. 2002), and more dynamically evolved cores show a temperature drop towards the centre (Crapsi et al. 2007; Pagani et al. 2007). Crapsi et al. (2007) observed a temperature drop down to ≈ 6 K towards the centre of L1544 (see also Young et al. 2004). Pagani et al. (2007) and Launhardt et al. (2013) also reported gradients in temperature outwards from the centres of cores with observations of $N_2H^+ - N_2D^+$, and far-infrared (FIR)-submillimetre continuum, respectively. However, the transition in gas temperature from cores to their immediate surroundings has not been studied. This is important, as dust and gas are not thermally coupled at volume densities below 10^5 cm^{-3} (Goldsmith 2001), as expected in inter-core material (average density in L1688 is $\sim 4 \times 10^3$ cm^{-3}, see Section 3.3.1). Therefore, the gas temperature can provide important constraints on the cosmic-ray ionisation rate (with cosmic rays being the main heating agents of dark clouds), as discussed in Ivlev et al. (2019). This transition in temperature, as well as in other physical properties, such as velocity dispersion, density and NH_3 abundance, from core to cloud, is the focus of the present paper.

In our previous paper (Choudhury et al. 2020, hereafter Paper I) we reported a faint supersonic component along with the narrow core component, towards all cores. We suggested that the broad component traces the cloud surrounding the cores, and therefore, presents an opportunity to study the gas in the neighbourhood of the cores with the same density tracer. Here, we extend that analysis to study the changes in physical properties of these two components from cores to their surroundings.

In this project, we use the data from GAS in L1688 –smoothed to a larger beam– to study the transition in both velocity dispersion and temperature, from coherent cores, to the extended molecular cloud, using the same lines (NH_3 (1,1) and (2,2)). In Section 3.3, the primary NH_3 data from GAS and complimentary *Herschel* continuum maps, are briefly described. Section 3.4 explains the procedure used to determine the physical parameters in the cloud. The improved integrated intensity maps and the parameter maps are presented in Section 3.5. In Section 3.6, the selection of coherent cores, considered in this paper is explained, followed by a discussion on the observed transition of physical parameters and spectra, from cores to their surroundings.

3.3 Data

3.3.1 Ammonia maps

As our primary data set, we use the NH_3 (1,1) and (2,2) maps, taken from the first data release of Green Bank Ammonia Survey (GAS, Friesen et al. 2017). The observations were carried out using the Green Bank Telescope (GBT) to map NH_3 in the star forming regions in the Gould Belt with $A_V > 7$ mag, using the seven-beam K-Band Focal Plane Array(KFPA) at the *GBT*. Observations were made in frequency switching mode with a frequency throw of 4.11 MHz (≈52 km s^{-1}at 23.7 GHz). The spectral resolution of the data is 5.7 kHz, which corresponds to ≈ 72.1 ms^{-1}at 23.7 GHz (approximate frequency of observations). The extents of the maps were selected using continuum data from *Herschel* or *JCMT*, or extinction maps derived from 2MASS (Two Micron All Sky Survey). To convert the spectra from frequency to velocity space, central

frequencies for NH_3 (1,1) and (2,2) lines were considered as 23.6944955 GHz and 23.7226333 GHz, respectively (Lovas et al. 2009).

Out of the four regions in the GAS DR1, we focus on L1688 in this paper, as we were able to obtain an extended kinetic temperature map of the cloud for this region. L1688 is part of the Ophiuchus molecular cloud at a distance of $\sim 138.4 \pm 2.6$ pc (Ortiz-León et al. 2018). The cloud mapped in NH_3 is $\sim$1 pc in radius with a mass of $\approx 980\, M_\odot$ (Ladjelate et al. 2020b). Assuming spherical geometry and a mean molecular weight of 2.37 amu (Kauffmann et al. 2008), the average gas density is then $\sim 4 \times 10^3$ cm^{-3}.

The parameter maps of L1688, released in DR1, are not very extended, particularly for kinetic temperature, as a robust temperature measurement is restricted by the signal-to-noise ratio (S/N) of the (2,2) line. Therefore, in order to have a good detection, especially of the (2,2) line, in the outer and less dense part of the cloud, the data were smoothed by convolving them to a beam of 1′ (*GBT* native beam at 23 GHz is $\approx$31″). The data cube was then re-gridded to avoid oversampling. The relative pixel size was kept the same as the original GAS maps, at one-third of the beam-width. The mean root-mean-square (rms) noise level achieved as a result is 0.041 K and 0.042 K in the (1,1) and (2,2), respectively. For comparison, the mean noise level in the GAS DR1 maps was 0.17 K. Figure 3.1 shows the integrated intensity maps obtained for NH_3 (1,1) and (2,2).

3.3.2 H_2 column density and dust temperature maps

L1688 was observed in dust continuum using the *Herschel* space observatory as part of the Herschel Gould Belt Survey (HGBS, André et al. 2010a). In order to compare the dust-derived properties to our results with NH_3, we use the dust temperature and H_2 column density in Ophiuchus from the HGBS archive[1] (Ladjelate et al. 2016). These maps were also convolved to a 1′ beam, and then regridded to the same grid as the NH_3 maps. Figures 3.2 and 3.3 show the smoothed and re-gridded N(H_2) and dust temperature maps, respectively.

3.4 Analysis

3.4.1 Line fitting

We fit NH_3 line profiles to the data with the `pyspeckit` package (Ginsburg & Mirocha 2011), which uses a forward modelling approach. We follow the fitting process described in Friesen et al. (2017). The range in velocity to fit is determined from the average spectra of the entire region. As the ortho-to-para ratio in the region is not known, we only report the p-NH_3 column density here, and do not attempt to convert it to total NH_3 column density[2].

The model produces synthetic spectra based on the guesses provided for the input parameters : excitation temperature (T_{ex}), kinetic temperature (T_K), para-ammonia column density (N(p-

[1] `www.herschel.fr/cea/gouldbelt/en/archives`

[2] To compare to the total NH_3 column densities reported in other works, an easy conversion is to multiply N(p-NH_3) by 2, if the ortho-to-para ratio is assumed to be the LTE value of unity.

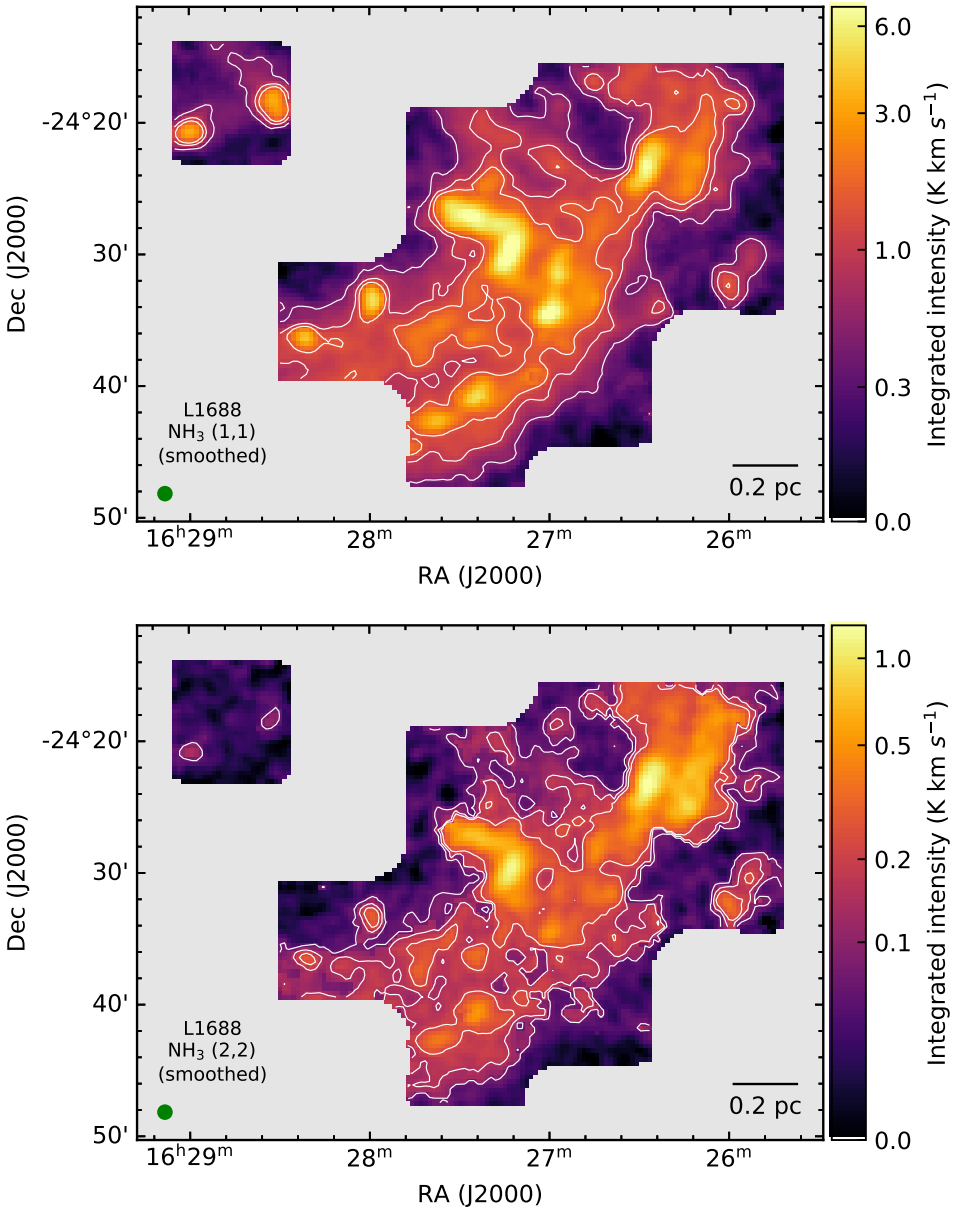

Figure 3.1: Integrated intensity maps of NH_3 (1,1) (top) and (2,2) (bottom) lines. For NH_3 (1,1), the contour levels indicate 15σ,30σ, and 45σ, and for NH_3 (2,2), contours are shown for 6σ,12σ, and 18σ; where σ is the median error in emitted intensity calculated from the signal-free spectral range in each pixel and converted to the error in integrated intensity. The moment maps were improved by considering only the spectral range containing emission, as described in Section 3.5.1. The $1'$ beam, which the data was convolved to, is shown in green in the bottom-left corner, and the scale bar is shown in the bottom-right corner.

NH_3)), velocity dispersion (σ_v) and line-of-sight central velocity (v_{LSR}) of the gas (see Section

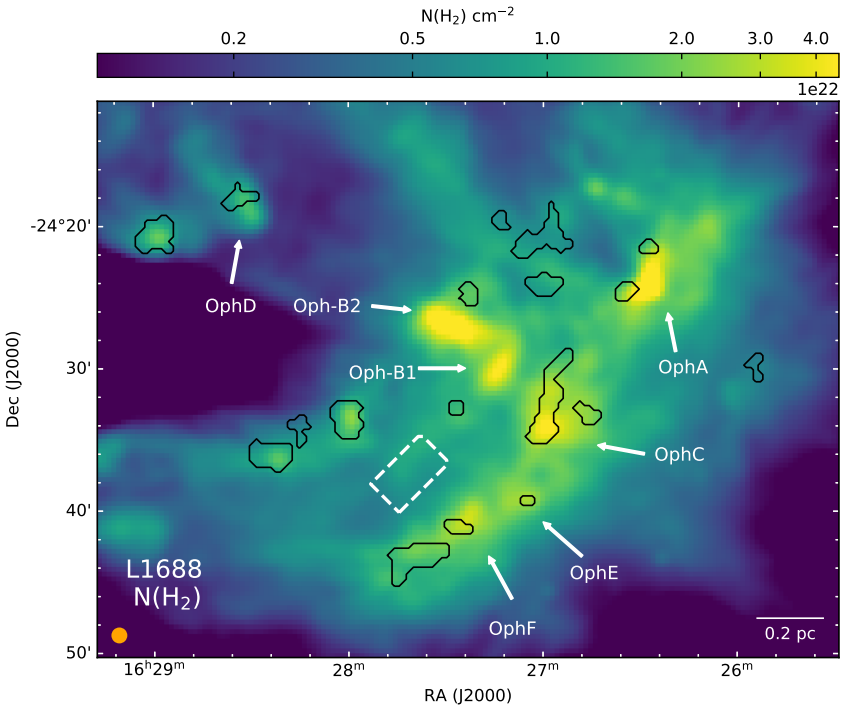

Figure 3.2: $N(H_2)$ in L1688, taken from Herschel Gould Belt Survey archive. Positions of the continuum cores reported in (Motte et al. 1998) are indicated by arrows. The dashed rectangle shows the area used to calculate mean cloud properties (see Section 3.5.3). The solid black contours show the coherent cores in the region (described later in Section 3.5.4). The 1′ beam, which the data was convolved to, is shown in orange in the bottom-left corner, and the scale bar is shown in the bottom-right corner.

3.1 in Friesen et al. 2017). A nonlinear gradient descent algorithm, MPFIT (Markwardt 2009) is then used to determine the best-fit model, and corresponding values of the parameters. A good set of initial conditions is necessary to ensure that the nonlinear least-squares fitting does not get stuck in a local minimum. The value of v_{LSR} is critical; therefore, we use the first-order moments of the (1,1) line as initial guesses. The second-order moments are used as guesses for velocity dispersion. For the other parameters, we use : $\log_{10}(N_{p-NH_3}/cm^{-2}) = 14$, $T_K = 20$ K and $T_{ex} = 5$ K. These numbers are within the range of values reported in GAS DR1 maps, and are therefore reasonable guesses. As a test, we checked the fits with varying guesses, and determined that the exact values of the initial parameters does not affect the final results, as long as they are within a reasonable range.

In this work, we use the `cold_ammonia` model in `pyspeckit` library, which makes the assumption that only the (1,1), (2,2), and (2,1) levels are occupied in p-NH_3. It is also assumed that the radiative excitation temperature, T_{ex}, is the same for (1,1) and (2,2) lines, as well as their hyperfine components.

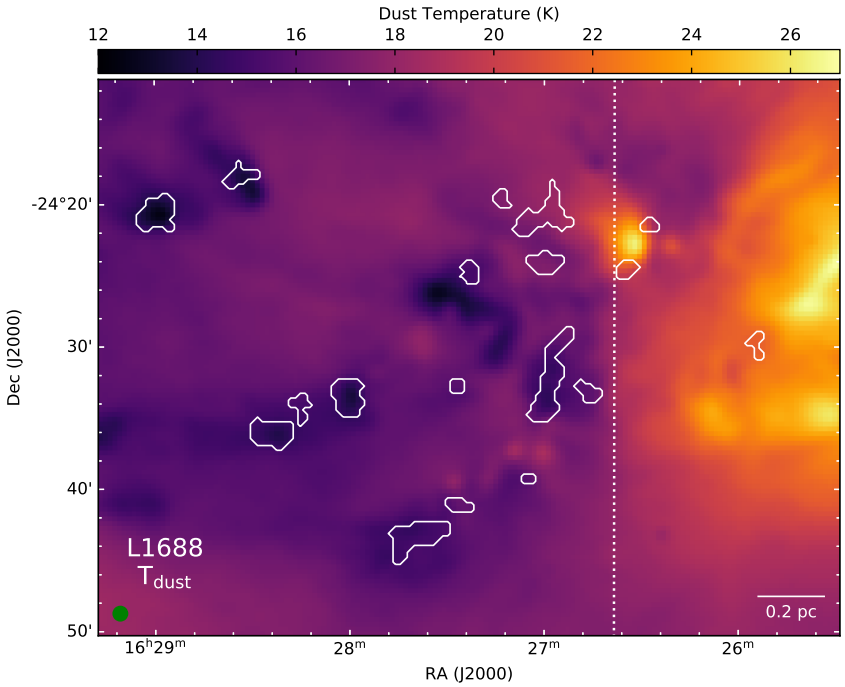

Figure 3.3: Dust temperature in L1688, taken from Herschel Gould Belt Survey archive. The solid white contours show the coherent cores in the region (described later in Section 3.5.4). The vertical dotted line roughly separates the dark cloud (to the left of the line) from the molecular material affected by the external illumination, due to irradiation from HD147889 (Habart et al. 2003). The 1′ beam, which the data was convolved to, is shown in green in the bottom-left corner, and the scale bar is shown in the bottom-right corner.

3.4.2 Data masking

To ensure that the parameters are well determined from the fit, several flags are applied on each parameter, separately. For a good fit to the (1,1) and (2,2) lines, a clear detection is necessary. For centroid velocity, velocity dispersion and excitation temperature, we mask the pixels with a S/N<5 in the integrated intensity of the (1,1) line. Similarly, we remove pixels with a S/N<3 in the peak intensity of the central hyperfine of the (2,2), in the kinetic temperature and p-NH_3 column density maps. These lower limits for the S/N in the (1,1) and (2,2) lines were chosen after a visual inspection of the spectra and the model fits in randomly sampled pixels in order to determine which flags most effectively filtered out the unreliable fits. As we use the pixels with a S/N of 5 or more in the integrated intensity of the (1,1), we expect the excitation temperature, centroid velocity, and velocity dispersion to be determined with reasonably high certainty. Similarly, for kinetic temperature, we only use the pixels with detection of the (2,2) with S/N of 3 in the peak intensity, and therefore T_K should also be well determined. Therefore, we mask the pixels with a fit determined error >20% of the corresponding parameter from the T_K, v_{LSR} and σ_v maps. Calculation of N(p-NH_3) requires a good determination of excitation temperature, and `pyspeckit` reports log(N(p-NH_3)), and the error in log(N(p-NH_3)). We still expect N(p-NH_3) to

be determined with reasonable accuracy, and therefore we set the relative error cut in N(p-NH_3) at 33% (3σ).

3.5 Results

3.5.1 Integrated Intensity maps

While calculating the integrated intensity of the region, it is better to use a narrow range of velocities around the velocity at each pixel than using a broad, average velocity range for the entire cloud, because there is a gradient in velocity present among different parts in L1688. Therefore, we employ the procedure described in Section 3.2 of Friesen et al. (2017) in deriving the moment maps. We use the best-fit model at each pixel and select the spectral range for which the model shows an intensity > 0.0125 K [3]. In places where the fit was not satisfactory (based on fit-determined errors), we use the average value of v_{LSR} and σ_v for the cloud. We then use the known relative positions of the hyperfine transitions of (1,1) and (2,2) to define a range where any emission is expected. We then calculate the integrated emission (and the associated error) using only these channels.

The integrated intensity maps thus obtained for the smoothed data are presented in Figure 3.1.

3.5.2 Property maps

Figures 3.4-3.6 show the velocity, velocity dispersion, NH_3 kinetic temperature and p-NH_3 column density maps for L1688 obtained from our fits. We obtain much more extended maps for velocity dispersion and kinetic temperature (73.4% and 65% of the total observed area, respectively), compared to the original GAS DR1 maps (Figs. 13 and 17 in Friesen et al. 2017, 19.2% and 13% of the total observed area respectively). Also, for the first time, we are able to map the temperature in the dense cores, as well as the surrounding gas in the same density tracer.

In the less dense, outer region of the cloud, the NH_3 (1,1) line becomes optically thin, and so, the excitation temperature is harder to determine satisfactorily[4]. Correspondingly, the p-NH_3 column density (Figure 3.6) is also not well determined away from some of the continuum cores (identified in Motte et al. 1998).

3.5.3 Variation of temperature and velocity dispersion throughout the cloud

Figure 3.5 shows the kinetic temperature in L1688. Motte et al. (1998) identify seven dense cores, namely Oph-A, Oph-B1, Oph-B2, Oph-C, Oph-D, Oph-E and Oph-F, from continuum observations in the cloud (these are shown in Figure 3.2). It can be clearly seen from Figure

[3] Although this threshold is below the noise level (≈ one-quarter), it was chosen because it significantly recovered the flux in the model.

[4] We observe that typically for τ (1,1) < 0.12, it is difficult to constrain T_{ex} and therefore the ammonia column densities.

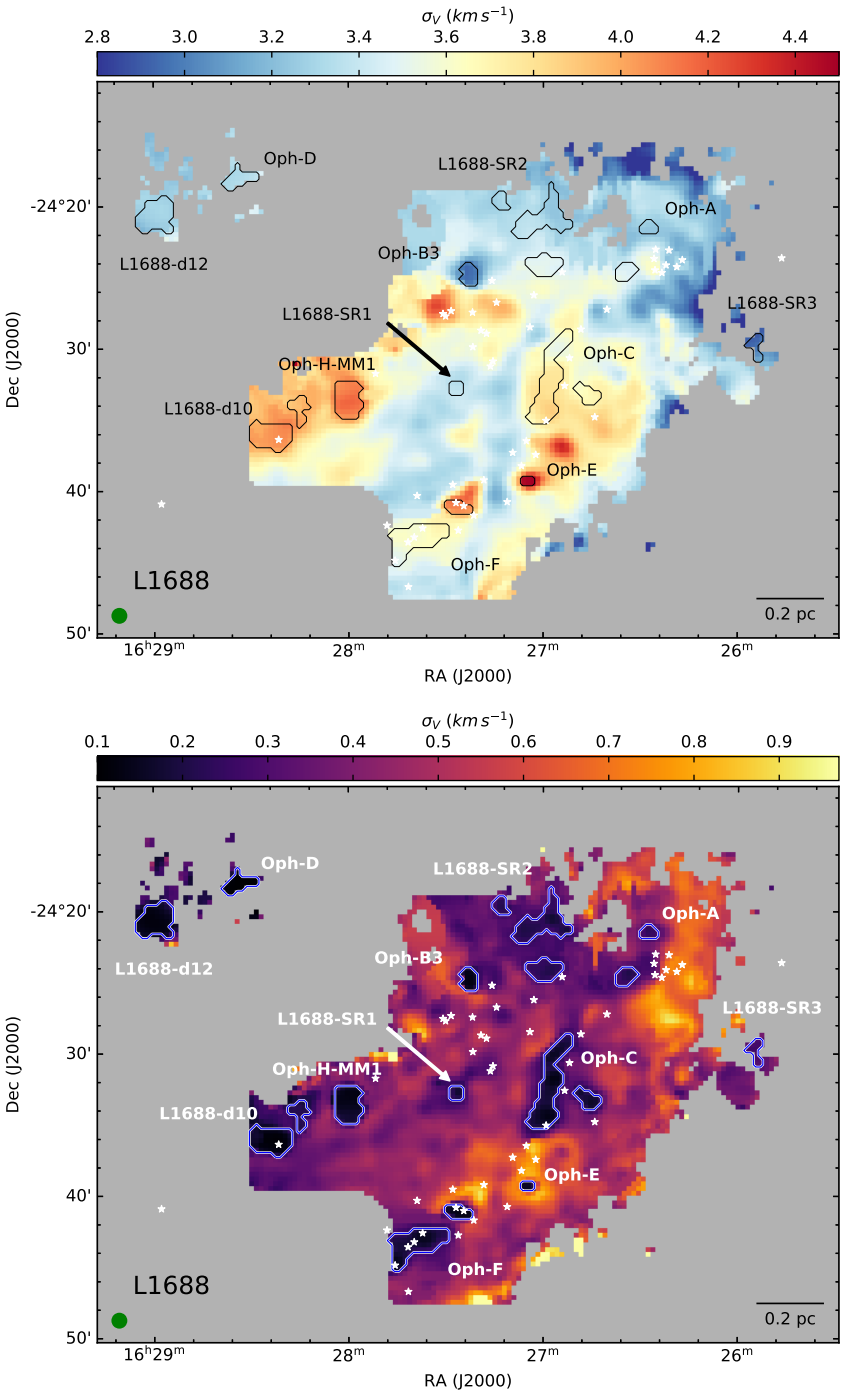

Figure 3.4: Centroid velocity (top panel) and velocity dispersion (bottom panel) in L1688. The contours are similar to Figure 3.3. The black (top panel) and white (bottom panel) stars show the positions of Class 0/I and flat-spectrum protostars (Dunham et al. 2015). The beam is shown in green in the bottom-left corner, and the scale bar is shown in the bottom-right corner.

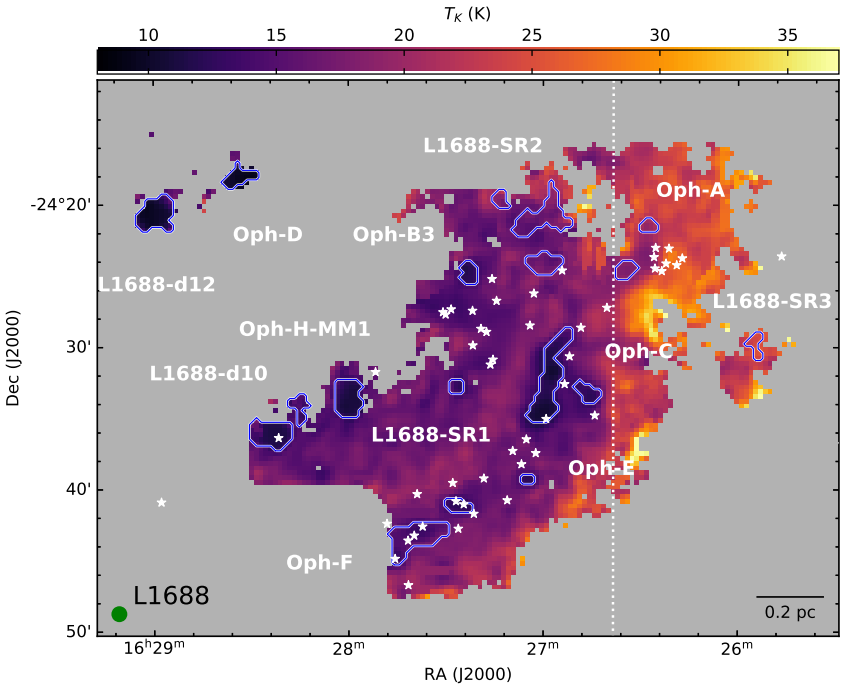

Figure 3.5: Kinetic temperature in L1688. The solid blue contours show the coherent cores in the region (described later in Section 3.5.4). The white stars show the positions of Class 0/I and flat-spectrum protostars. To see the difference between the part of the cloud affected by the external radiation, and the dark cloud further away from the illumination source, we consider a vertical boundary, as shown. The beam is shown in green in the bottom-left corner, and the scale bar is shown in the bottom-right corner.

3.5, that these continuum cores are at a lower temperature than the gas surrounding them. On average, the kinetic temperature in the N(H_2) peak inside the continuum cores is ≈ 3.7 K lower than the mean ambient cloud temperature (calculated in the area shown by the dashed rectangle in Figure 3.2).

To the west of the cloud, there is a strong radiation field due to a young, massive B2-type star (Houk & Smith-Moore 1988), HD147889 (RA:16h25m24.31s, Dec:-24°27′56.57″; Gaia Collaboration 2018). The radiation field near the western edge is estimated to be $\sim$ 400 G_0 [5](Habart et al. 2003). Due to this external illumination, the kinetic temperature is ≈ 7.8 K higher in the western edge of the cloud (considered as the region to the right of the vertical boundary shown in Figure 3.5) compared to the mean cloud temperature. This increase in temperature can also be seen in the dust temperature map from *Herschel* (Figure 3.3).

In the velocity dispersion map in Figure 3.4, we see that the continuum cores identified in Motte et al. (1998, shown in Figure 3.2), except Oph-B1 and Oph-B2, show less turbulent gas compared to the surrounding gas. The dispersion averaged over one beam around the continuum

[5]Definition of G_0 from Hollenbach & Tielens (1999): G_0 represents the unit of an average interstellar flux of 1.6 erg cm^{-2} s^{-1} in the energy range 6-13.6 eV (Habing 1968).

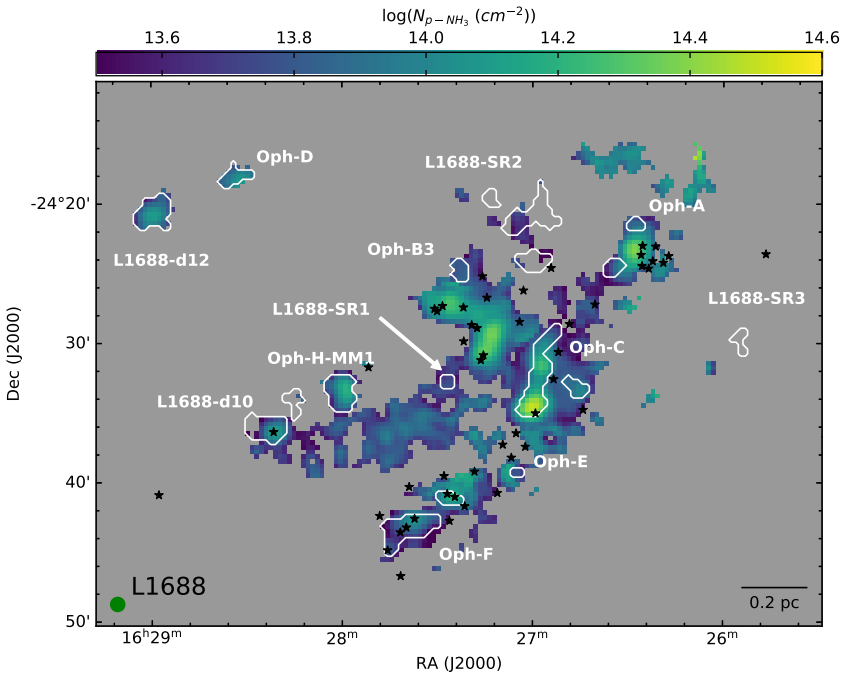

Figure 3.6: p-NH_3 column density in L1688. The solid white contours show the coherent cores in the region (described later in Section 3.5.4). The black stars show the positions of Class 0/I and flat-spectrum protostars. The beam is shown in green in the bottom-left corner, and the scale bar is shown in the bottom-right corner.

peaks of Oph-C, Oph-D, Oph-E and Oph-F is $\leq 0.2\,\mathrm{km\,s^{-1}}$, and around the continuum peak of Oph-A is $\approx 0.3\,\mathrm{km\,s^{-1}}$. Oph-B1 and Oph-B2 contain a cluster of Class 0/I and flat spectrum protostars, similar to Oph-F in type, number and luminosity. However, Oph-F shows gas in low dispersion, whereas the σ_v observed in Oph-B is significantly higher(≈ 0.45 and $0.54\,\mathrm{km\,s^{-1}}$, averaged over one beam around the continuum peaks of Oph-B1 and Oph-B2, respectively). A strong outflow is observed in the vicinity of Oph-B1 and Oph-B2 (Kamazaki et al. 2003; White et al. 2015), and no such outflow is seen near Oph-F. Therefore, the higher σ_v observed in Oph-B might be associated with the presence of protostellar feedback.

Figure 3.7 shows how the kinetic temperature of the gas changes with respect to velocity dispersion in L1688. Due to the large number of data points, we show a density distribution plot instead of the actual data set in order to represent the distribution more clearly. Here, we use a Gaussian kernel density estimator (KDE) from the package `scipy`. The KDE replaces each data point with a Gaussian of a constant width, and the sum of the individual Gaussians is used as an estimate for the density distribution of the data. The width of the Gaussian is determined using Scott's rule (Scott 1992), and depends on the number of data points.

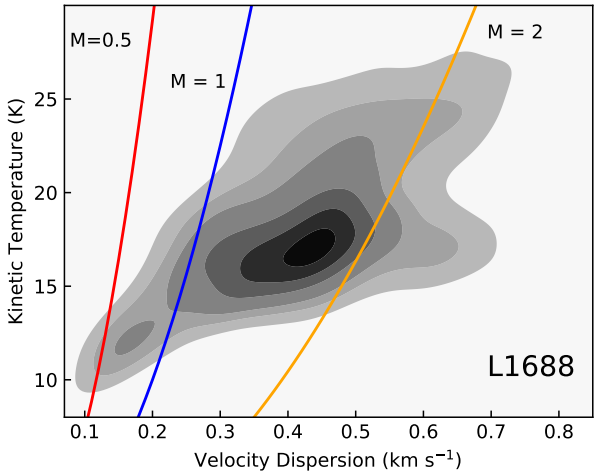

Figure 3.7: Kinetic temperature and velocity dispersion in L1688, shown here as a normalised kernel density distribution. The contour levels are 0.1,0.2,0.3,0.5,0.7 and 0.9. The red, blue and orange lines represent Mach numbers of 0.5, 1 and 2, respectively.

3.5.4 Identification of coherent cores

In order to study the change in kinetic temperature and velocity dispersion from cores to the surrounding material, we first identify what we consider as 'coherent cores'. For this purpose, we use the sonic Mach number, $\mathcal{M}_S$, which is defined as the ratio of the non-thermal velocity dispersion to the sound speed in the medium :

$$\mathcal{M}_S = \frac{\sigma_{\rm v,NT}}{c_S} \,, \tag{3.1}$$

where c_S is the one-dimensional sound speed in the gas, given by :

$$c_S = \sqrt{\frac{k_B T_{\rm K}}{\mu_{\rm gas}}} \,, \tag{3.2}$$

where k_B is the Boltzmann's constant, $T_{\rm K}$ is the kinetic temperature in the region, and $\mu_{\rm gas}$ is the average molecular mass (taken to be 2.37 amu, Kauffmann et al. 2008). The non-thermal component of the velocity dispersion is calculated by removing the thermal dispersion for the observed molecule ($\sigma_{\rm T}$) from the total observed velocity dispersion ($\sigma_{\rm v}$) :

$${\sigma_{\rm v,NT}}^2 = {\sigma_{\rm v}}^2 - {\sigma_{\rm T,NH_3}}^2 - {\sigma_{\rm chan}}^2 \,, \tag{3.3}$$

where $\sigma_{\rm chan}$ is the contribution due to the width of the channel. The thermal component of the dispersion observed in NH_3 is:

$$\sigma_{T,\rm NH_3} = \sqrt{\frac{k_B T_K}{\mu_{\rm NH_3}}} \,, \tag{3.4}$$

with μ_{NH_3} = 17 amu, being the mass of the ammonia molecule. For T_K = 14 K, the thermal component (σ_{T,NH_3}) is 0.082 km s^{-1}.

When a Hann-like kernel is used in the spectrometer, the correction factor for the measured velocity dispersion is given by (see Leroy et al. 2016; Koch et al. 2018) :

$$\sigma_{\rm chan} = \frac{\Delta}{\sqrt{2\pi}}(1.0 + 1.18k + 10.4k^2) \,, \tag{3.5}$$

where Δ is the spectral resolution and k is dependent on the Hann-like function applied. In the case of the VEGAS spectrometer used in the GAS observations, k is 0.11, which corresponds to a correction term of:

$$\sigma_{chan} = \frac{\Delta}{1.994} = 0.036\,{\rm km\,s^{-1}} \,. \tag{3.6}$$

After applying this small correction, we obtain a typical non-thermal component of the velocity dispersion of $\sigma_{v,NT}$ = 0.182 km s^{-1}, for σ_v = 0.2 km s^{-1}.

In Figure 3.7, it can be observed that a group of points lies below the line depicting a Mach number of 1, and a much larger distribution lies in the supersonic part of the plot. This separation is taken as the basis for separating the subsonic cores from the extended, more turbulent cloud. We first identify a mask with the regions in L1688 having a sonic Mach number of 1 or lower (similar to Pineda et al. 2010; Chen et al. 2019). Regions smaller than the beam size are removed from the mask. All the remaining regions are then considered as the 'coherent cores' in L1688.

Based on this definition, we identify 12 regions in L1688 as coherent cores (same as Paper I). These include:

- Five continuum cores, namely Oph-A, Oph-C, Oph-D, Oph-E and Oph-F. We identify two islands in Oph-A as coherent cores (Oph-A North, and Oph-A South), and consider them together as Oph-A.
- One DCO^+ core, Oph-B3 (Loren et al. 1990; Friesen et al. 2009).
- Two 'coherent droplets', L1688-d10 and L1688-d12, (Chen et al. 2019).
- One prestellar core Oph-H-MM1 (Johnstone et al. 2004).

Apart from these previously identified cores[6], we also identified three more subsonic regions : L1688-SR1 (south of Oph-B1), L1688-SR2 (three islands east of Oph-A) and L1688-SR3 (near the western edge of the map). These cores are shown in Figure 3.8, along with the positions of Class 0/I and flat spectrum protostars in L1688 (Dunham et al. 2015). Following the classification of Class-0 and -I protostars in the region according to Enoch et al. (2009), we find no significant difference between the positions of Class 0/I protostars and those of flat spectrum protostars with respect to the coherent cores. The continuum cores Oph-B1 and Oph-B2 are not subsonic, as

[6]Oph-B3, Oph-D and H-MM1 are also identified as L1688-c4, L1688-d11 and L1688-d9, respectively, in Chen et al. (2019). The two structures that we identify as Oph-A are likely associated with Oph-A-N2 and Oph-A-N6, as identified in N_2H^+ by Di Francesco et al. (2004).

previously discussed (Section 3.5.3, see also : Friesen et al. 2009), and therefore, they are not considered as 'coherent cores' by our definition.

Because we use a larger beam (almost twice in size) compared to the GAS data, our definitions of the coherent boundaries are expected to vary slightly compared to other analyses carried out with the original data (e.g. Chen et al. 2019, which also applied more stringent criteria[7] in their definition). However, comparison with Chen et al. (2019) shows that the overall coherent boundaries in the two works are consistent within one beam (1′).

Ladjelate et al. (2020b) identifies a prestellar core at the position of SR1, and an unbound starless core at the position of SR3. SR1 and SR3 are associated with a local peak in NH_3 integrated intensity. SR2 does not contain any bound core in *Herschel* data, nor does it show a local NH_3 peak. However, as can be seen from our later results (presented in Section 3.6.5), the ambient cloud in the line of sight to the cores has a higher temperature compared to the gas in the core. However, in the computation of $N(H_2)$ from *Herschel* data, a single temperature was assumed for the entire line of sight. Therefore, it is possible that small clumps of over-densities at the position of coherent cores, which have a much lower temperature than that of the ambient cloud, will not be seen in the $N(H_2)$ maps. Without allowing for different temperatures in different parts of the cloud along the line of sight in the calculations of $N(H_2)$, we cannot dismiss the possibility of an over-density being associated with SR2.

In order to study the environment surrounding the coherent cores, we define two consecutive shells around each core. Shell-1 is defined as all the pixels around each coherent core, within a distance of one beam (the smallest resolved scale) from the boundary. Shell-2 is defined as all the pixels around shell-1 within one beam. This allows us to study the environment surrounding the cores in the two consecutive layers. The regions defined[8] are displayed in Figure 3.8.

As mentioned earlier, although considered as continuum cores, Oph-B1 and Oph-B2 are not coherent cores according to our definition. Being close to these two cores, the shells of Oph-B3 and L1688-SR1 might contain some high column density gas with supersonic velocity dispersions, produced by protostellar feedback, which is not representative of the cloud surrounding a coherent core. Therefore, we define a boundary roughly containing Oph-B1 and Oph-B2 based on column density ($N(H_2)>2.1\times10^{22}\,cm^{-2}$, shown in white dashed contours in Figure 3.8), and remove the pixels inside this boundary from the shells of Oph-B3 and L1688-SR1 for all subsequent analyses.

[7]Chen et al. (2019) had further requirements for the coherent regions to be identified as 'droplets' (such as associated local maxima in peak NH_3 (1,1) intensity and $N(H_2)$, and relatively smooth v_{LSR} distribution inside), whereas we consider the sonic Mach number as the only criterion.

[8]For most cases, the shells of different cores have little to no overlap. For L1688-d10 and H-MM1, there would have been some overlap with the shell definitions, but we avoid this overlap by restricting the boundaries of respective shells-2, as can be seen in Figure 3.8

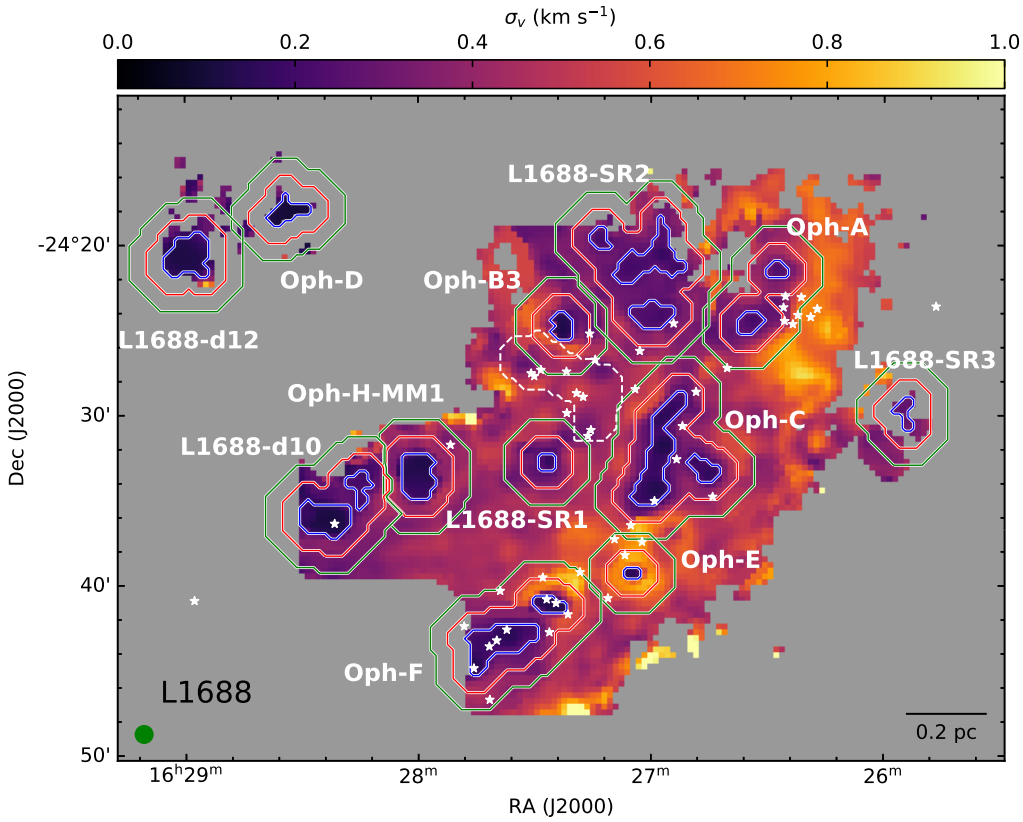

Figure 3.8: Coherent cores and their immediate neighbourhood, as defined in Section 3.5.4, shown in the velocity dispersion map. The coherent cores, and the shell-1 and shell-2 regions are shown with blue, red, and green contours, respectively. The white dashed contour shows the boundary considered for continuum cores Oph-B1 and Oph-B2 (see Section 3.5.4 for details). The white stars show the positions of Class 0/I and flat-spectrum protostars in the cloud. The beam and the scale bar are shown in the bottom left and bottom right corners, respectively.

3.6 Discussion

3.6.1 Transition from coherent cores to their immediate neighbourhood: A distribution analysis

We study the change in kinetic temperature and dispersion observed between the coherent cores and their surrounding environment (shell-1 and shell-2). The left panel of Figure 3.9 shows the kernel density distribution of kinetic temperature with velocity dispersion for all the cores, and corresponding shell-1 and shell-2. The coherent cores are characterised by a kinetic temperature 3-7 K lower than shell-1 and shell-2. The velocity dispersion in the cores is also 0.2-0.4 km s^{-1}lower than in the shells. Compared to the change in T_K and σ_v from core to shell-1, the values of the two parameters in shell-1 and shell-2 do not change as much. The kinetic temperatures of the two shells are within $\approx$2 K of each other, and the difference in dispersion is $\leq$

0.1 km s^{-1}.

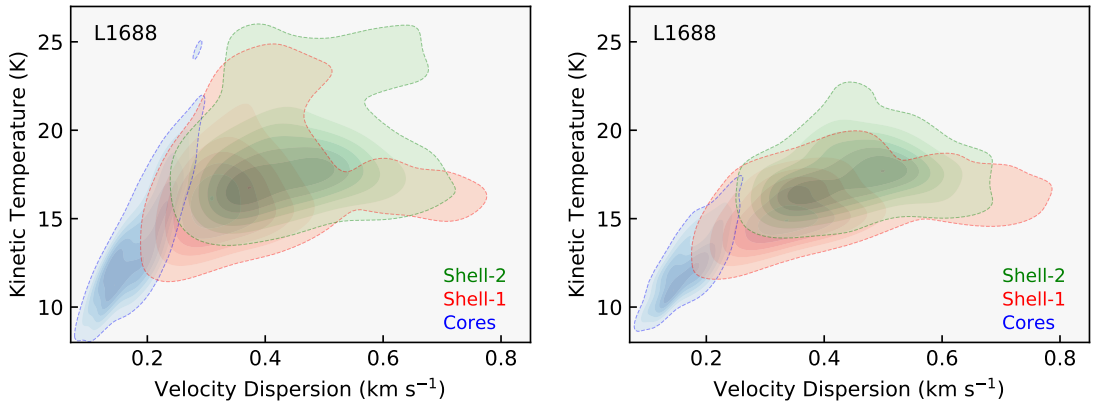

Figure 3.9: Left : Distribution of kinetic temperature and velocity dispersion for all the coherent cores and the shell-1 and shell-2 regions. Shells-1 and shells-2 are defined as two consecutive shells of width equal to one beam around the respective coherent cores. Each kernel density distribution was normalised to have a peak density of 1. The contours show normalised KDE levels of 0.1, 0.25, 0.4, 0.55, 0.7 and 0.85. Right : Same as the left panel, but without the regions L1688-SR3, L1688-SR2, and Oph-A, and ignoring one beam at each star position. This is done to remove the effect of external heating, and possible contribution from prostellar feedback.

The transition from the coherent cores to the surrounding molecular cloud in kinetic temperature is gradual, and there is no sudden jump, indicating that it changes smoothly from core to cloud at the angular resolution of the present work. By our definition of the cores, the transition in velocity dispersion at the core boundaries is sharp. The average kinetic temperature and velocity dispersion for the coherent cores are 12.107±0.009 K and 0.1495±0.0001 km s^{-1}, respectively[9] with a standard deviation of 3.2 K and 0.047 km s^{-1}. Similarly, for the first shell, the average values are $T_{\rm K}$=15.80±0.01 K (std. dev. = 3.12 K) and $\sigma_{\rm v}$=0.3175±0.0002 km s^{-1}(std. dev. = 0.127 km s^{-1}); and for the second shell, $T_{\rm K}$=18.11±0.02 K (std. dev. = 3.5 K) and $\sigma_{\rm v}$=0.4176±0.0004 km s^{-1}(std. dev. = 0.127 km s^{-1}). We selected three roundish cores: Oph-E, Oph-H-MM1 and L1688-d12, and compared the radial profiles of velocity dispersion with those reported in Chen et al. (2019). We observed that $\sigma_{\rm v}$ inside these coherent cores lies inside the 1σ distribution of pixels in each distance bin equal to the beam size for the corresponding droplet in Chen et al. 2019. Furthermore, we also observed that the radial profiles showed similar shape as compared to those in Chen et al. (2019), up to shell-2. Therefore, we see similar radial profiles to those of Chen et al. (2019), even though we are using a larger beam. On average, we see a kinetic temperature difference of ≈ 4 K between core and shell-2, i.e. ≈ 2′ from core. Harju et al. (2017) observed a similar increase in kinetic temperature, ≈ 5 K, 2′ away from the centre of the starless core H-MM1 (see also Crapsi et al. 2007). This is consistent with the temperature structure of externally heated dense cores (e.g. Evans et al. 2001; Zucconi et al. 2001).

[9]All the averages reported in this section are weighted averages, with associated error on the weighted average.

Assuming the gas to be completely molecular, so that $N_{\rm H} = 2 \times N(H_2)$, and the relation between hydrogen column density and optical extinction to be $N_{\rm H}$ (cm^{-2}) $\approx 2.21 \times 10^{21}\ A_V$ (mag) (Güver & Özel 2009), we find that the average extinction through the cores is ≈16 mag. Through shell-1 and shell-2, the average extinctions are $A_V \approx 13.16$ and $A_V \approx 11.2$ mag, respectively. As we do not have the p-NH_3 column density in the extended cloud (away from the cores), we fit the average spectra (see Section 3.6.2) of each core and their shells to get an idea of the average N(p-NH_3) in the regions. From that analysis, we find that the average p-NH_3 column density in the cores is $\approx (8.99 \pm 0.08) \times 10^{13}$ cm^{-2}; and that in shell-1 and shell-2 are $(5.2 \pm 0.1) \times 10^{13}$ cm^{-2} and $(3.7 \pm 0.1) \times 10^{13}$ cm^{-2}, respectively.

As mentioned in Section 3.5.3, the west part of L1688 is affected by a strong external radiation field, the effect of which can be clearly seen in the kinetic temperature map (Figure 3.5). The regions Oph-A, L1688-SR3, and L1688-SR2 lie in the affected region of the cloud. To get a clearer view of the behaviour of kinetic temperature and velocity dispersion in the embedded cores (without the effect of the outside illumination), we omit the regions L1688-SR3, L1688-SR2, and Oph-A, as well as their neighbourhoods. In order to remove any possible contribution from prostellar feedback in the regions, we also mask one beam at the positions of known protostars (Dunham et al. 2015). The distribution of the remaining cores and the shells is shown in the right panel of Figure 3.9. When the effects of external illumination, and possible contributions from protostellar feedback are masked, the average kinetic temperature in the cores drops (11.66±0.01 K, std. dev. = 1.71 K). The change in $\sigma_{\rm v}$ is not as stark, with the average for the new distribution being 0.1487±0.0001 km s^{-1}(std. dev. = 0.038 km s^{-1}). Similarly, masking the heating by the external radiation removes the high kinetic temperature region in shells 1 and 2, reducing the average temperature to 14.68±0.02 K (std. dev. = 1.9 K) and 17.37±0.02 K (std. dev. = 2.1 K), respectively. By comparison, the spread in $\sigma_{\rm v}$ remains almost constant, and its average value is unchanged (within errors). Therefore, our results suggest that the external irradiation is not accompanied by turbulence injection in the neighbourhood of the cores.

3.6.2 Transition from coherent cores to their immediate neighbourhood: Analysis of individual cores

For the cores L1688-SR3, Oph-D, and d12, we have the kinetic temperature information for very few points in shells 1 and 2. The individual pixels in these shells do not have sufficient S/N for a good fit, and therefore direct determination of the kinetic temperature in the individual pixels is not possible. Moreover, $T_{\rm K}$ could not be determined in some pixels in the outer shells of d10, L1688-SR2, Oph-A and Oph-F either. Therefore, to get a fair comparison of the temperatures in the cores, shells-1 and shells-2, we average the spectra in each of these regions. Stacking the spectra for a large number of points results in significantly reduced noise levels, and we have sufficient S/N to be able to fit these spectra and obtain the kinetic temperature for each region. With the low noise, we are also able to look at minor details in the spectra towards each core and shell. To avoid any possible line broadening due to averaging in a region with velocity gradients, we align the spectra at each pixel within a region before averaging. For this, we take the velocity at a pixel, determined from the one-component fit at that pixel, and using the `channelShift`

function from module `gridregion` in the GAS pipeline[10], we shift the spectra at that pixel by the corresponding number of channels. We then average the resultant spectra from all pixels inside a region, now essentially aligned at v=0.

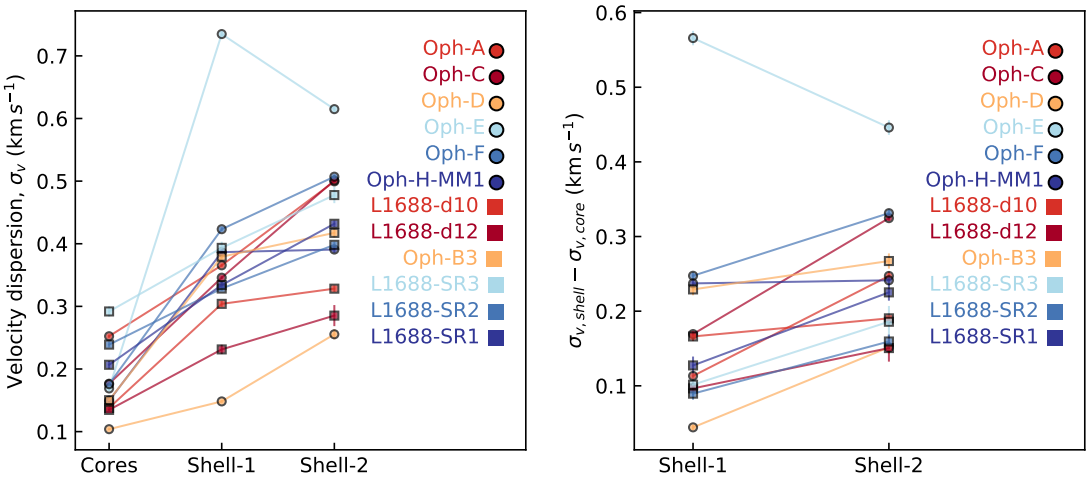

Figure 3.10: Left panel: Velocity dispersion in the core and the shells determined from average spectra in the respective core or shell. Shells-1 and shells-2 are defined as two consecutive shells of width equal to one beam around the respective coherent cores. Right panel : Velocity dispersion in the shells relative to their respective cores.

Figures 3.10 and 3.11 show the velocity dispersion and kinetic temperature, respectively, at each individual core and their respective neighbourhoods, determined from one-component fits to the averaged spectra in those regions. This gives us an idea of the change in the parameters as we move from core to shell-1, and then to shell-2. The left panel of Figure 3.10 shows the velocity dispersions of each individual core, shell-1 and shell-2. The right panel shows the σ_v of the shells, relative to their corresponding cores. Similarly, Figure 3.11 shows this relation for kinetic temperature.

Figure 3.10 shows that, as expected, the velocity dispersion increases from core to shell-1 for all cores. For most cores, the dispersion steadily increases outwards to shell-2. Oph-E is an exception to this, where σ_v decreases slightly in shell-2. It is clearly seen that for all the cores, the kinetic temperature steadily increases from the cores to shells 1 and 2. For d12, we see a slight drop in temperature from shell-1 to shell-2, but the difference is within the error margin, and therefore not significant. It can be again seen that the highest kinetic temperatures for cores, shell-1 and shell-2 are for the regions affected by the outside illumination (Oph-A, L1688-SR2 and L1688-SR3). The temperature rise from shell-1 to shell-2 for Oph-C is very drastic, as the second shell includes part of the cloud heated by the external radiation (see Figure B.1 for reference).

We estimate the volume densities in the core, shell-1, and shell-2, with the T_{ex}, T_K, and τ measurements from the one-component fits using the following relation described in Foster et al.

[10]https://github.com/GBTAmmoniaSurvey/GAS/tree/master/GAS

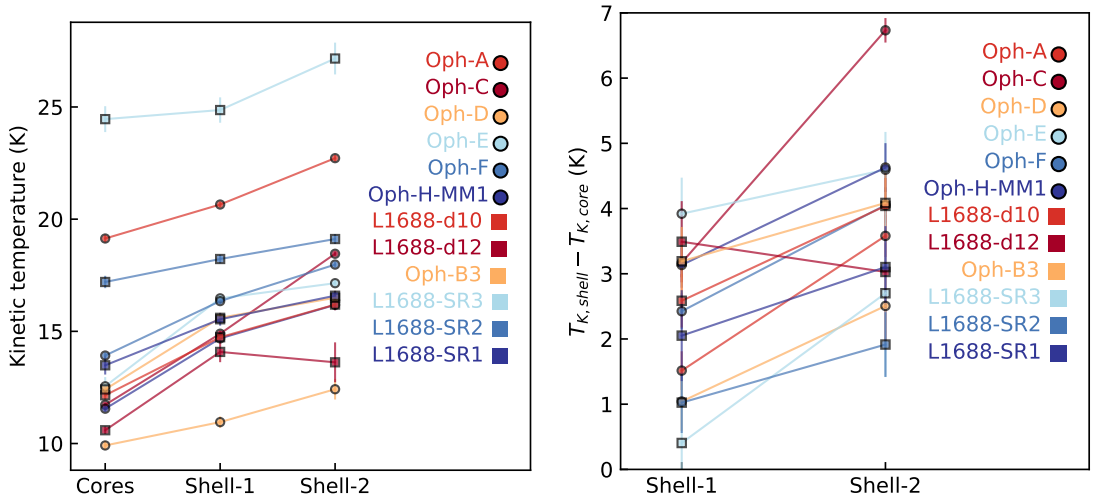

Figure 3.11: Left panel: Kinetic temperature in core and the shells, determined from average spectra in the respective core or shell. Shells-1 and shells-2 are defined as two consecutive shells of width equal to one beam around the respective coherent cores. Right panel : Kinetic temperature in the shells relative to their respective cores.

(2009):

$$n = \frac{(J(T_{\rm ex}) - J(T_{cmb})kJ(T_{\rm K}))}{h\nu_{(1,1)}(1 - J(T_{\rm ex}))} \times n_{crit} \times \beta\,, \tag{3.7}$$

where $T_{\rm cmb} = 2.73$ K, $n_{\rm crit} = 2 \times 10^4$, k is the Boltzmann's constant, h is the Planck's constant, β is the escape probability estimated as $\beta = (1 - e^{-\tau})/\tau$, and

$$J(T) = \frac{h\nu_{(1,1)}}{k(1 - e^{-\frac{h\nu_{(1,1)}}{kT}})}\,. \tag{3.8}$$

We find the cores to have a mean density of $1.66\pm0.09\times10^5$ cm^{-3}. Shell-1 and shell-2 have similar densities : $1.5\pm0.1\times10^5$ cm^{-3} and $1.4\pm0.2\times10^5$ cm^{-3}, respectively[11]. The densities in all of these three regions are more than an order of magnitude higher than the average density of the cloud traced by NH_3, calculated using the $N(H_2)$ estimate from *Herschel* ($\sim 4 \times 10^3$cm^{-3}, see Section 3.3.1). It should be noted that the density estimate from Foster et al. (2009) uses measurements with NH_3, which traces a higher density than dust continuum. Therefore, by design, the Foster et al. (2009) estimate is mainly sensitive to higher density regions, whereas the *Herschel* continuum measurements refer to a significantly larger volume (as dust is much more extended than NH_3). Also, the *Herschel* column density maps are obtained assuming a single line-of-sight dust temperature, which might create discrepancies in the $N(H_2)$ estimate, especially towards the cores, which are much colder than the surrounding gas. Therefore, a systematic difference in the two density estimates (using NH_3, and from the $N(H_2)$ map) is expected.

[11]Non-weighted averages

3.6.3 Comparison of kinetic temperature with dust temperature

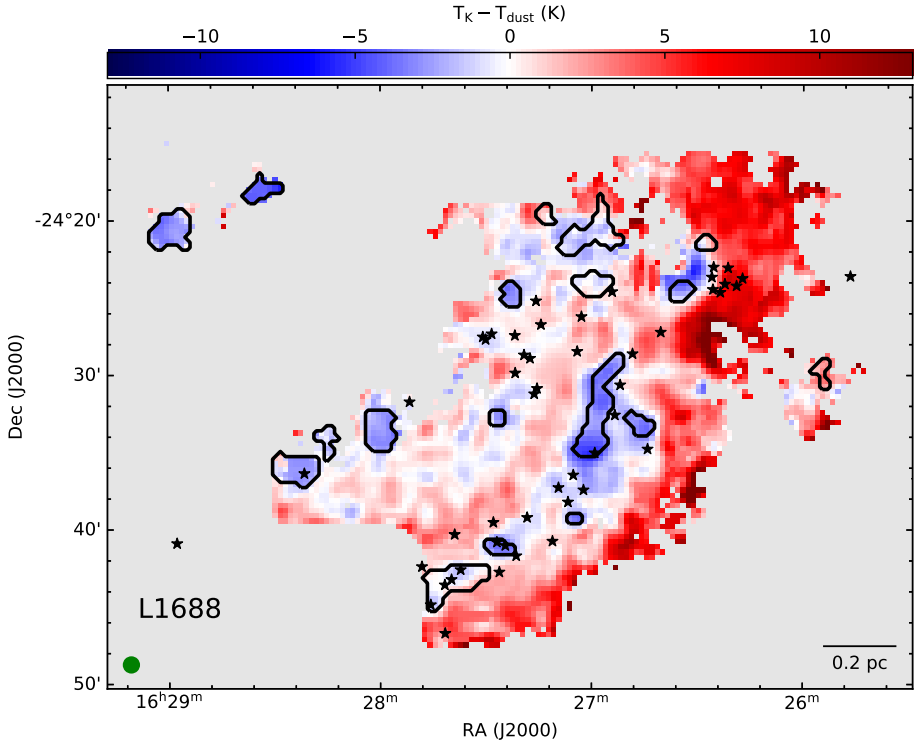

Figure 3.12: Map of the difference between kinetic temperature (from NH_3) and dust temperature (from *Herschel*). The black stars show the positions of known protostars in the region. The solid black contours show the coherent cores in the region (see Section 3.5.4). The beam and the scale bar are shown in the bottom-left and bottom-right corners, respectively.

In Figure 3.12, we show the map of the difference between the kinetic temperature derived using NH_3 and the dust temperature derived from *Herschel*. The blue region in the map shows the gas with kinetic temperature less than dust temperature, and the red part shows the region in L1688 with kinetic temperature higher than dust temperature. Gas and dust are expected to be effectively coupled only at densities above $10^{4.5}$ cm^{-3} (Goldsmith 2001; Galli et al. 2002). The average density in L1688 is lower than 10^4 cm^{-3} (Section 3.3.1) and therefore gas–dust coupling is not achieved in this cloud (except in the core regions and their neighbourhoods).

Although NH_3 emission in L1688 is extended, the comparison with the dust temperature indicates that NH_3 is not tracing the larger scale molecular cloud traced by the dust emission (or by low-density tracers such as CO). Instead, it is likely tracing the inner region of the cloud (at $A_v > 10$ mag), where NH_3 is abundant and its inversion transitions can be excited. The coherent cores have a lower kinetic temperature than dust temperatures, even though their identification is done only using the kinematical information (σ_v). This is expected, because the NH_3 emission towards the cores is dominated by the inner dense, cold core material; whereas the dust temperature is representative of the temperature of the foreground, outer part of the cloud. On average,

the kinetic temperature in the coherent cores is 1.8 K lower than the dust temperature. In the two shells surrounding the cores, the situation is reversed. In shell-1, the kinetic temperature is marginally higher ($\approx$ 0.3 K) than the dust temperature, and in shell-2, the difference is even stronger, $T_{\rm K}$ - $T_{\rm dust}$ $\approx$ 1.8 K. The gas towards the western edge, which is affected by the strong external radiation (defined as the region to the right of the vertical dotted line shown in Figure 3.3), shows ammonia at a temperature that is $\approx$5 K higher than the dust temperature. This region is illuminated by a far-ultraviolet (FUV) field of $\sim$ 400 G_0 (Habart et al. 2003). Therefore, the gas temperature in this region is significantly higher than the dust temperature, as expected in a dense region with high external illumination (Koumpia et al. 2015), and as gas–dust coupling is not achieved at those densities.

3.6.4 Ammonia abundance

To see how the ammonia abundance varies going from the cores to the surrounding cloud, we separate the points in the coherent cores and the shells. It can be seen from Figure 3.6, that we are not able to obtain a much extended map for the p-NH_3 column density. Consequently, we have too few points in shell-2 of the cores for a meaningful analysis. Therefore, we limit our analysis of NH_3 abundance to only the cores and shell-1. As mentioned in Section 3.4.1, in this work we focus on the column density of only para-ammonia. We do not attempt to convert this into the total NH_3 column density because the ortho-to-para ratio is unknown.

Figure 3.13 shows the distribution of N(p-NH_3) with N(H_2), inside the cores (left panel) and shell-1 (right panel). We note that the plots only show the pixels, for which a good determination of N(p-NH_3) was possible. To clearly show the distribution of a large number of points, we plot the KDE instead of the individual data points in the plots (the calculation of KDE distribution from the data is explained in Section 3.5.3). The error in p-NH_3 column density is considered in the calculation of the KDE.

To get an estimate of the para-ammonia abundance in the cores and shell-1, we fit a straight line of the form `y = mx + c` to each data set. The slope of the line, `m`, gives us the fractional para-ammonia abundance, $X(p\text{-}NH_3) = N(p\text{-}NH_3)/N(H_2)$, in the region. We use `curve_fit` from the python package `scipy` to obtain the best linear fit. We take into account the error in our calculation of N(p-NH_3) in fitting this data. However, as the error associated with the H_2 column density was not available in the *Herschel* public archive, we do not incorporate any error in the x-axis for the fit.

The model in the core is a good fit to the data. The fit in shell-1 is slightly offset from the peak due to the presence of a small number of high N(p-NH_3) points. However, the fit still provides a good constraint on the slope, which is the parameter of interest. From this analysis, we report an average para-ammonia fractional abundance (with respect to H_2) of $4.2\pm0.2\times10^{-9}$ in the coherent cores, and $1.4\pm0.1\times10^{-9}$ in shell-1. Therefore, the para-ammonia abundance drops by a factor of three from the cores to their immediate surroundings. The p-NH_3 abundance within the coherent cores reported here is comparable to that in L1544, as found by Tafalla et al. (2002), Crapsi et al. (2007), and Caselli et al. (2017a), which is $\approx 4\times10^{-9}$. Crapsi et al. (2007) also report a similar drop in abundance for a similar distance outside the core in L1544. These latter authors report an abundance of $\approx2\times10^{-9}$ at a distance $\sim$10 000 au. This is comparable to the abundance we report

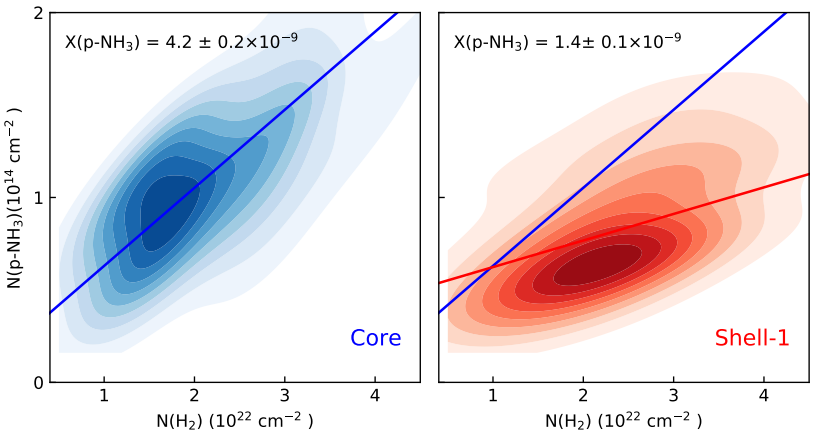

Figure 3.13: Kernel density estimate representation of the distribution of p-NH_3 column density with $N(H_2)$ in the cores (in red) and shell-1 (in blue), as defined in Section 3.5.4 and shown in Figure 3.8. The straight lines show the best linear fit to the data in the corresponding region. For comparison between the regions, the linear fit to the data in the cores (red line) is also shown in the plot for shell-1. The slopes of the linear fits indicate the fractional p-NH_3 abundance (with respect to H_2) in the region, which is shown in the top-left corner.

for shell-1, which is at a similar distance (∼10 000 au) from the cores in our study[12].

3.6.5 Presence of a second component : comparison with Paper I results

From the fits and corresponding residuals to the average spectra towards all the cores and most of the shells (Figures B.3 to B.14), we see that the single component fits do not recover all the flux. This indicates the presence of a second component in these spectra. In Paper I, we analysed the dual-component nature of the spectra towards the cores. It was shown that a faint supersonic component is present along with the narrow core component, towards all cores. We suggested that the narrow component is representative of the subsonic core, and the broad component traces the foreground cloud next to the cores. Here, we extend that analysis to shell-1 and shell-2 around the coherent cores, and study how the two components change going from the cores to their shells.

Similar to Paper I, we use the Akaike information criterion (AIC), which determines if the quality of the model improves significantly, considering the increase in the number of parameters used. We find that for all the regions, the two-component fit is a better model to the spectra. However, with a closer look at the spectra, we see that for shell-2 of d12, and shell-1 of SR3, one of the components fit by the model has very large σ_v ($> 1\,\mathrm{km\,s^{-1}}$), and is very faint (peak $T_{MB,(1,1)} \approx 10\,\mathrm{mK}$, which is comparable to, or lower than the noise in the spectrum). Therefore,

[12]These studies report the total ammonia abundance ($X(NH_3)$). We convert this to X(p-NH_3) for comparison, using an ortho-para ratio of unity, as assumed in these studies.

we do not have reliable constraints for the fits to these components, and so we do not consider them for further analysis.

Extending the definition of the two components used in Paper I, we refer to the two components as 'narrow' and 'broad' based on their velocity dispersion. However, it should be noted that unlike towards the cores (in Paper I), the narrow components in the shells, especially shell-2, are not always subsonic. In this paper, our distinction of the components is merely based on the velocity dispersion, in order to be able to track the transition of each component from core to shell-2.

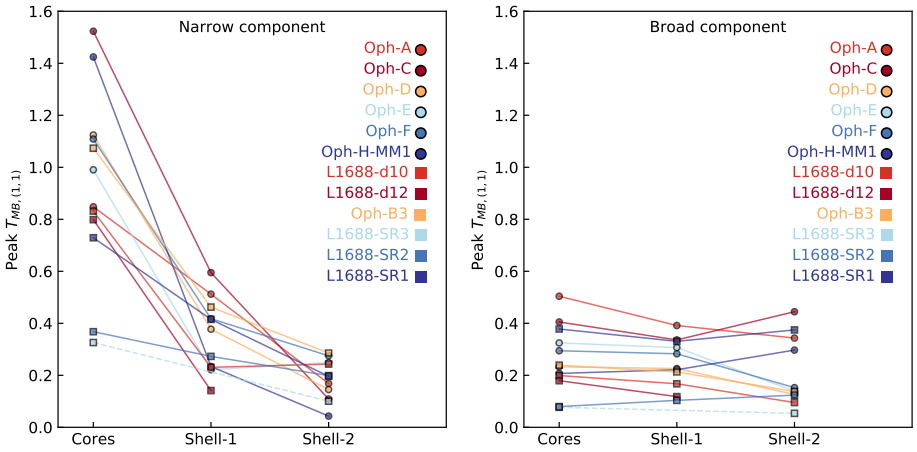

Figure 3.14: Left panel: Peak main beam brightness temperature of (1,1), for the narrow component in the cores, shells-1, and shells-2. Shell-1 and shell-2 are defined as two consecutive shells of width equal to one beam around the respective coherent cores. Right panel : Same variance, but for the broad component. We note that as we do not consider the two-component fit to shell-1 of SR3 (see Section 3.6.5), the values for the core and shell-2 are connected by a dashed line.

Figure 3.14 shows the variation of the peak main beam brightness temperature of the (1,1) across cores and shells for the narrow component (left panel) and the broad component (right panel). It can be seen that the intensity of the narrow component decreases sharply from core to shell-1, and less so from shell-1 to shell-2. In comparison, the intensity of the broad component remains largely constant for all three regions. This result agrees with the conclusions of Paper I, in that the narrow component is the core component, and the broad component is a single cloud component representative of the surrounding cloud. This figure also shows that the single component fit results would be skewed towards the narrow component in the core. The flux is dominated by the broad components in shell-2 because of the larger width, as the intensities are similar to those of the narrow components. For shell-1, neither component is clearly dominant.

The variation of velocity dispersion and kinetic temperature from the cores to the shells for the two components, is shown in Figures 3.15 and 3.16, respectively. It can clearly be seen from Figure 3.15 that the narrow component becomes more turbulent further away from the cores.

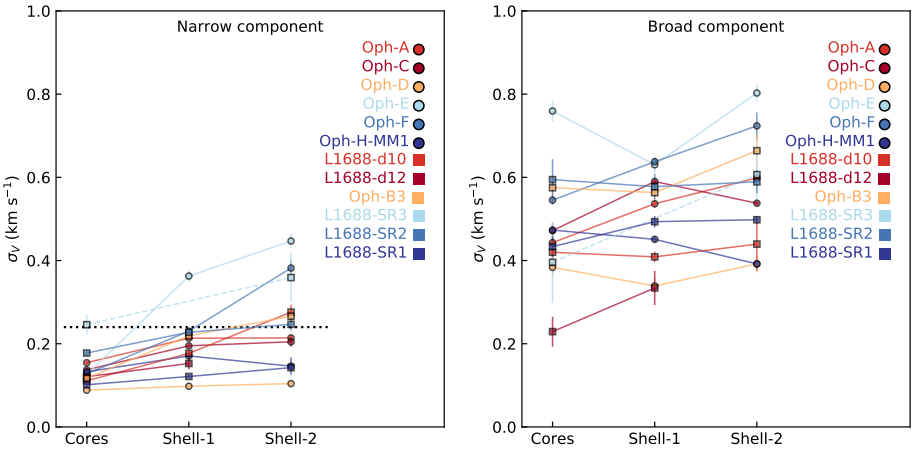

Figure 3.15: Left panel: Velocity dispersion of the narrow component in the cores, shells-1 and shells-2. Shells-1 and shells-2 are defined as two consecutive shells of width equal to one beam around the respective coherent cores. The black-dotted line shows the velocity dispersion with $\mathcal{M}_S = 1$ at typical core temperature of T_K=10 K. Right panel : Same, but for the broad component. We note that as we do not consider the two-component fit to shell-1 of SR3 (see Section 3.6.5), the values for the core and shell-2 are connected by a dashed line.

The broad cloud component does not show any clear trend and is mostly invariant. The narrow component, even in shell-2, has lower σ_v than the broad component towards the cores. This again agrees with the interpretation of Paper I, in that the narrow component traces the subsonic core, and the broad component traces the more turbulent surrounding cloud.

For the kinetic temperature, we do not see a clear trend in either of the two components (Figure 3.16). It can be seen that the narrow component is slightly colder towards the cores compared to the shells. In general, the narrow component is at a lower temperature than the broad component. In shell-2 of Oph-C, the (2,2) line could not be fit for the broad component, and therefore, the kinetic temperature of that component is not well defined. Hence, shell-2 of Oph-C is omitted from Figure 3.16 (for the broad component).

Figure 3.16 shows that for H-MM1, the kinetic temperature of the narrow component shows an unusual trend, in that T_K in shell-2 seems to be $\approx$ 20 K higher than that in the core. A look at the spectra (Figure B.9) reveals that the relative positions of the narrow and broad component seem to switch from core and shell-1, to shell-2. The narrow component in shell-2 seems to be brighter in (2,2) than in shell-1. These unexpected behaviours could be explained by the relatively small change in AIC in the two-component fit, from the one-component fit (see B.1). As mentioned in Appendix E of Paper I, the physical properties derived from two-component fit are not well constrained, for small Δ_{AIC} (= $AIC_{1-comp} - AIC_{2-comp}$). In particular, for H-MM1, we find that more restrictions (e.g., not allowing the two components to switch their relative positions) results in a different two-component fit, with only a slightly smaller Δ_{AIC} (=27). This

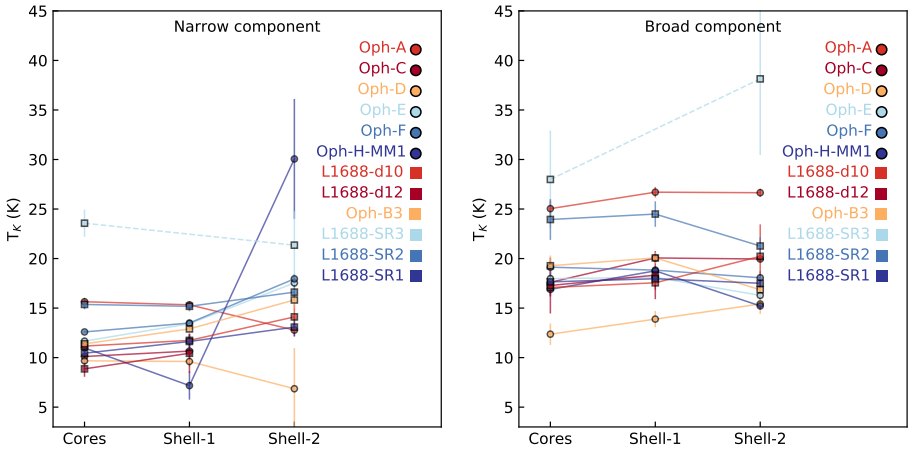

Figure 3.16: Left panel: Kinetic temperature of the narrow component in the cores, shells-1 and shells-2. Shells-1 and shells-2 are defined as two consecutive shells of width equal to one beam around the respective coherent cores. Right panel : Same variation, but for the broad component. We note that as we do not consider the two-component fit to shell-1 of SR3 (see Section 3.6.5), the values for the core and shell-2 are connected by a dashed line.

alternate fit (Figure B.15) indicates that there is no subsonic component in shell-2, but rather, two supersonic components ($\sigma_{\rm v} \approx 0.28\,{\rm km\,s^{-1}}$ for both). Therefore, as already mentioned in Paper I, we need to be cautious while considering the regions with low $\Delta_{\rm AIC}$ values, and need to inspect the fits to the spectra carefully.

In Paper I, we reported that the ambient cloud in L1688 (considered to be represented by the rectangular box shown in Figure 3.2) shows two supersonic components, with a small relative velocity. We suggested that a collision between these two cloud components might result in a local density increase, where the merging of the two broad components locally produces the narrow feature, following a corresponding dissipation of turbulence; thus creating the observed coherent cores with subsonic line widths. The gradual decrease in the dispersion of the narrow component, from shell-2 to core is congruent with this hypothesis.

Figure 3.17 shows the temperature of each coherent core (narrow component) as a function of the relative velocity between the two components towards the core. Here, we have not considered Oph-A, SR2, and SR3 to remove any possible contribution of the external radiation from the west. A general trend can be seen, with the core temperature increasing with the relative velocity of the two components. This might suggest that collision between the two components is responsible for a local temperature increase. However, owing to our relatively large beam, we cannot conclusively comment on the presence of local shocks (e.g. Pon et al. 2012), and would require higher resolution data in the region and observations in shock tracers to confirm or rule out this possibility.

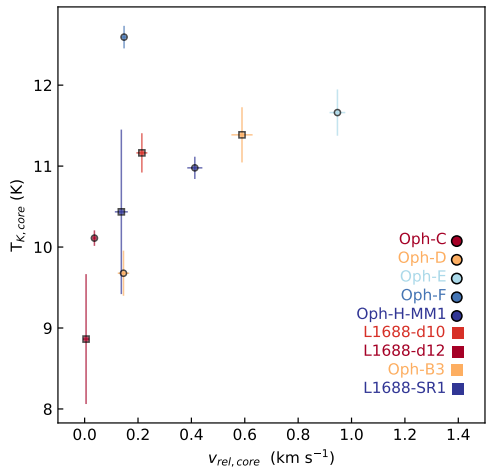

Figure 3.17: Kinetic temperature of the core (narrow) component, against the relative velocity between the core (narrow) component and the cloud (broad) component, towards each core. Oph-A, SR2, and SR3 are affected by the external illumination and are therefore not considered in this analysis.

3.6.6 Evidence of a subsonic component beyond previously identified coherent zones

The subsonic component seen in the cores is also detected in shell-1 for 10 out of the 12 coherent cores (except Oph-E, where there is no subsonic component in shell-1, and SR3, where the two-component fit in shell-1 of SR3 is not well constrained; see Section 3.6.5). Furthermore, in five regions (Oph-A, Oph-D, H-MM1, SR1 and SR2), the component with subsonic turbulence can be detected even in shell-2. This suggests that the subsonic component extends well beyond the typical boundary of the coherent cores, albeit much fainter in intensity (approximately one-fifth of the peak intensity in NH_3 (1,1)) than that towards the cores. This suggests that the transition to coherence is not sharp, as previously reported (e.g. Pineda et al. 2010; Friesen et al. 2017; Chen et al. 2019), but rather gradual. The sharp transition to coherence observed by Pineda et al. (2010) was within a 0.04 pc scale, which is very similar to our spatial resolution ($1'$ at $\approx$138 pc). It is likely that the transition observed by Pineda et al. (2010) in B5 was the transition between the narrow and the broad component. Due to the poorer sensitivity of the data, the broad component towards the core and the subsonic component outside the core boundary were not detected in their work. With averaged spectra, we are able to detect the two components towards the cores and the shells, and we observe that the coherent cores in Ophiuchus are indeed more extended than previously found with a one-component fit.

It should be noted that due to the lack of sensitivity, even with the smoothed data, we are not able to detect the broad component across the entire region; and the two-component analysis is only possible with the stacked spectra in the coherent cores and the shells. Therefore, with our

current sensitivity, we cannot use the narrow component to define the coherent core, which would be the ideal case, as we do not have a map of the narrow (or broad) component. We are therefore limited by the sensitivity to using the one-component fit, to define the coherent boundaries, as is the case in the existing literature. Our present results indicate that with more sensitive data, which would allow for a two-component fit, the coherent boundary could be improved.

We also observe that the core component smoothly broadens up to a supersonic velocity dispersion towards some cores, but the dispersion still does not reach that of the broad component at the corresponding position (see Figure 3.15). Although the value of the broad component could be interpreted as the level of turbulence outside the core, it is more likely that the larger velocity dispersion is due to a change in the scale traced along the line of sight, which could include large-scale velocity structure.

3.6.7 Turbulence–size relation

We observe the subsonic component extending outside the typical boundary of the coherent cores. We also observe this component gradually broadening outwards from the cores (Figure 3.15). Therefore, we looked at the relation between the turbulence (non-thermal velocity dispersion) in the component and the size of the regions. We define the equivalent radius ($r_{\rm eq}$) for each region as $A = \pi r_{\rm eq}^2$, where A is the area inside that region (core, shell-1 or shell-2).

As we could only detect the subsonic component outside the typical coherent core using stacked spectra in the shells with our current data, we only have three data-points for each core with which to fit for the turbulence–size relation. Moreover, the $\sigma_{\rm v,NT}$ for shell-2 often has relatively large errors (see Table B.1). Therefore, with the present sensitivity, we cannot obtain a reliable turbulence–size relation for each core separately, and so, we only fit an average relation considering all cores together. Figure 3.18 shows the turbulence in the narrow component towards each coherent core, shell-1 and shell-2 as a function of the respective equivalent radii.

We fit a power law, $\sigma_{\rm v,NT} = a\, r^b$, to the whole sample using the uncertainty in the derived non-thermal velocity dispersion with `emcee` (Foreman-Mackey et al. 2013). As we fit for an average relation for all the cores, we allow for a Gaussian intrinsic scatter term (with variance V) to the model, to account for the spread due to considering multiple cores. In the calculation of the likelihood parameter, the uncertainty in the model, σ, is then replaced by

$$\sigma_{\rm eff} = \sqrt{\sigma^2 + V}\,. \tag{3.9}$$

We use uniform priors for the exponent (b) and the constant (a) with a range that includes both tails of the individual posterior probability distributions. We then sample the distribution using `emcee` with 32 walkers in a 2D Gaussian around the maximum-likelihood result, and run 5000 steps of Markov Chain Monte Carlo (MCMC). With this, we obtain an auto-correlation time of ≈ 40 steps. We discard the first 200 steps to avoid effects of initialisation, and trim the distribution by half the auto-correlation time (20 steps). From this analysis, we determine the best fit to the data as

$$\sigma_{\rm v,NT} = (0.57 \pm 0.06)\, r_{\rm eq}^{(0.5\pm0.2)}\,. \tag{3.10}$$

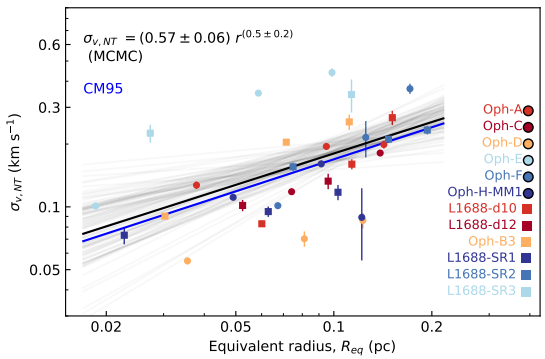

Figure 3.18: Non-thermal velocity dispersions in the narrow component for each core, shell-1, and shell-2 as a function of their equivalent radii. The grey lines show the power-law fits for the range of parameters obtained from a MCMC fit, and the black line shows the best-fit model. The blue line shows the turbulence–size relation from (Caselli & Myers 1995) for low-mass cores.

The derived exponent is consistent with the one reported by Caselli & Myers (1995) within the error bar. However, in that this latter study, the authors use a sample of mixed tracers, including ^{13}CO. Our results focus this relation to a narrow range of small-scale structures, down to $\approx$ 0.02 pc. The similarity of the exponent with the results from Caselli & Myers (1995) suggest that the turbulence–size relation remains approximately the same on scales closer to the core centre. Chen et al. (2020b) also observed similar exponents in line-width–size relations for Phase-I and -II cores in synthetic observations.[13]

3.7 Conclusions

We present a new analysis of the GAS DR1 data with GBT towards L1688 smoothed to 1′ resolution. Our results can be summarised as follows:

1. For the first time, we obtain substantially extended kinetic temperature and velocity dispersion maps, covering 65% and 73.4% of the observed area, respectively, including dense cores and the surrounding molecular cloud, using the same density tracer. This ensures continuity in the physical properties from core to cloud.

2. We identify 12 coherent cores in L1688 (same as Paper I), including 3 previously unidentified subsonic regions, SR1, SR2 and SR3.

3. Using a one-component fit to the data, we observe that both the kinetic temperature and the velocity dispersion gradually increase outwards from the coherent cores. On average, the kinetic temperature 1′ ($\approx$ 8000 au) and 2′ ($\approx$ 16000 au) away from the core boundary is

[13]It should be noted that Chen et al. (2020b) considered $\sigma_{\rm v}$ in their relation. For comparison with their work, we calculated the relation 3.10 for $\sigma_{\rm v}$.

approximately 4 K and 6 K higher than the core temperature. Similarly, the velocity dispersion in these regions is 0.15 km s^{-1}and 0.25 km s^{-1}higher than that in the core, respectively.

4. We find that the external illumination at the western edge of the cloud is not accompanied by turbulence injection.

5. The kinetic temperature towards the coherent cores is, on average, ≈ 1.8 K lower than the dust temperature. Outside the cores, the kinetic temperature of the gas is higher than the dust temperature.

6. We find an average para-ammonia fractional abundance (with respect to H_2) of $4.2\pm0.2\times10^{-9}$ in the coherent cores, and $1.4\pm0.1\times10^{-9}$, at $1'$ from the core. Previous works report a similar abundance within the core for L1544, and a similar drop in abundance for a similar distance outside the core.

7. By stacking the spectra towards the cores and their neighbourhoods, we are able to detect two velocity components, one narrow and one broad, superposed in velocity. For most cores, we observe that the component with subsonic turbulence is extended beyond the previously identified coherent regions. This suggests that the transition to coherence is gradual, in contrast to previous results. We observe that the subsonic component towards the cores becomes fainter and broader outwards, with a turbulence–size relation of $\sigma_{\rm v,NT} \propto r_{eq}^{b}$, with $b = 0.5 \pm 0.2$, similar to what was found in other low-mass dense cores using multiple molecular tracers.

8. In contrast, the broad component shows near-constant intensity and dispersion towards core and cloud. This supports our conclusions from Paper I of the broad component tracing material across the larger scale cloud seen with ammonia.

9. We observe that on average the cores with higher velocities relative to the surrounding cloud show higher temperatures. With higher resolution maps of the region and with adequate sensitivity, it would be possible to determine whether or not there are any local shocks around the coherent cores.

Chapter 4

Infall of Material into the Filaments in B5

The contents of this chapter will be submitted to Astronomy & Astrophysics Journal. Credit : Choudhury et al., in prep.

4.1 Abstract

Aims. We aim to study the structure and dynamics of the two filaments in the subsonic core Barnard 5 in Perseus with high-resolution ($\approx$ 2400 au) NH_3 data using multi-component fit analysis.
Methods. We use combined observations of NH_3 (1,1) and (2,2) inversion transitions using the Very Large Array (VLA) and the Green Bank Telescope (GBT). We smooth the data to a beam of $8''$ to reliably fit multiple velocity components towards the two filamentary structures identified in B5.
Results. Along with the core and cloud components dominating the flux in the line of sight, we detect two components towards the two filaments showing signs of infalling material. We also detect two additional components possibly tracing new material falling into the subsonic core of B5.
Conclusions. Using a criterion based on the velocity gradient orthogonal to the major axis of a filament, we conclude that both the filaments in B5 are formed from gravity-dominated accretion, helped by the significantly high mass-per-unit-length across the filaments ($\sim 75 M_\odot\,\mathrm{pc}^{-1}$). We also estimate infall rates of $1.1 \times 10^{-4} M_\odot\,\mathrm{yr}^{-1}$ and $1.8 \times 10^{-4} M_\odot\,\mathrm{yr}^{-1}$ for the material contracting in the two filaments.

4.2 Introduction

Stars form in cold dense cores embedded in molecular clouds. These cores are characterised by higher density and lower temperatures compared to the parental cloud (Myers 1983; Myers & Benson 1983; Caselli et al. 2002). Studies with high-density ($n(H_2) > 10^4\,\mathrm{cm}^{-3}$) tracers reveal subsonic levels of turbulence inside cores (Barranco & Goodman 1998; Rosolowsky et al. 2008),

in contrast to the supersonic linewidths observed in the ambient cloud (traced by lower density tracers, like CO; Larson 1981).

NH_3 is a very useful tracer to observe dense cores in molecular clouds. Even though it has a relatively lower critical density (few times $10^3 cm^{-3}$), the hyperfine structure of the NH_3 inversion transitions allows the individual hyperfines to remain optically thin even at high column densities (Caselli et al. 2017b). Fitting the multiple hyperfines simultaneously also gives a very precise constraint on the dynamical information. Moreover, if the NH_3 (2,2) line is reliably detected along with the (1,1), it allows for a direct measurement of the gas temperature (Friesen et al. 2017).

Previous observations have shown filaments to be widely present in molecular clouds in star forming regions and connected to subsonic dense cores (Goldsmith et al. 2008; André et al. 2010b; Polychroni et al. 2013). These filamentary structures have been extensively observed using *Herschel* (Ward-Thompson et al. 2010; André et al. 2014; Arzoumanian et al. 2019) and studied regarding physical properties including density and temperature. Molecular line observations of filaments revealed complex kinematical structures (Kirk et al. 2007; Henshaw et al. 2013; Hacar et al. 2013).

Chen et al. (2020a) suggested the use of a dimensionless parameter, C_v to distinguish between two scenarios resulting in the formation of filaments, namely, turbulent-driven and gravity-dominated compression. They defined this parameter to be proportional to the square of the velocity gradient orthogonal to the major axis of the filament and inversely proportional to the mass per unit length of the filament. This parameter has been used to identify the formation scenarios of filaments in observations of different regions (e.g. Zhang et al. 2020; Gong et al. 2021; Hsieh et al. 2021). However, in these studies, a single value is calculated representing the entire filament, and no distribution along the filament is reported. Analysis of velocity gradients along the filament could highlight the robustness of this use of the parameter and study the overall structure of the filaments.

We study the subsonic core Barnard 5 (hereafter B5) in the Perseus molecular cloud with combined Very Large Array (VLA) and Green Bank Telescope (GBT) observations using NH_3 (1,1) and (2,2) transitions. B5 is located at a distance of 302±21 pc (Zucker et al. 2018), and hosts a young stellar object (YSO), the Class-I protostar B5-IRS1 (Fuller et al. 1991). Using NH_3 hyperfine transitions, Pineda et al. (2010) revealed the turbulence inside the core to be subsonic and nearly constant, with a sharp transition to coherence at the core boundary. Further interferometric observations with high spatial resolution ($\approx$ 1800 au, or 6″) revealed two filaments embedded in the subsonic core (Pineda et al. 2011a) and three gravitationally bound condensations (Pineda et al. 2015; Schmiedeke et al. 2021). In this project, we use this high-resolution data, smoothed to a slightly larger beam (8″), to study detailed structure within B5 with multi-component analysis.

4.3 Ammonia maps

We use single-dish observations of B5 with the GBT combined with interferometric observations with the VLA using NH_3 hyperfine transitions (1,1) and (2,2). The GBT observations were performed under project 08C-088 with on-the-fly (OTF) mapping (Mangum et al. 2007b) in

frequency switching mode. The data have a spectral resolution of about 3 kHz (or 0.04 km s^{-1}). More details of the data processing can be found in Pineda et al. (2010), where the data were first published. The interferometric data were obtained with the VLA (project 11B-101) in the D-array configuration on 16-17 October 2011 and in DnC-array configuration on 13-14 January 2012. The spectral resolution of the data was 0.049 km s^{-1}. For a detailed description of the data, see Pineda et al. (2015). The resolution of the combined data is 6″.

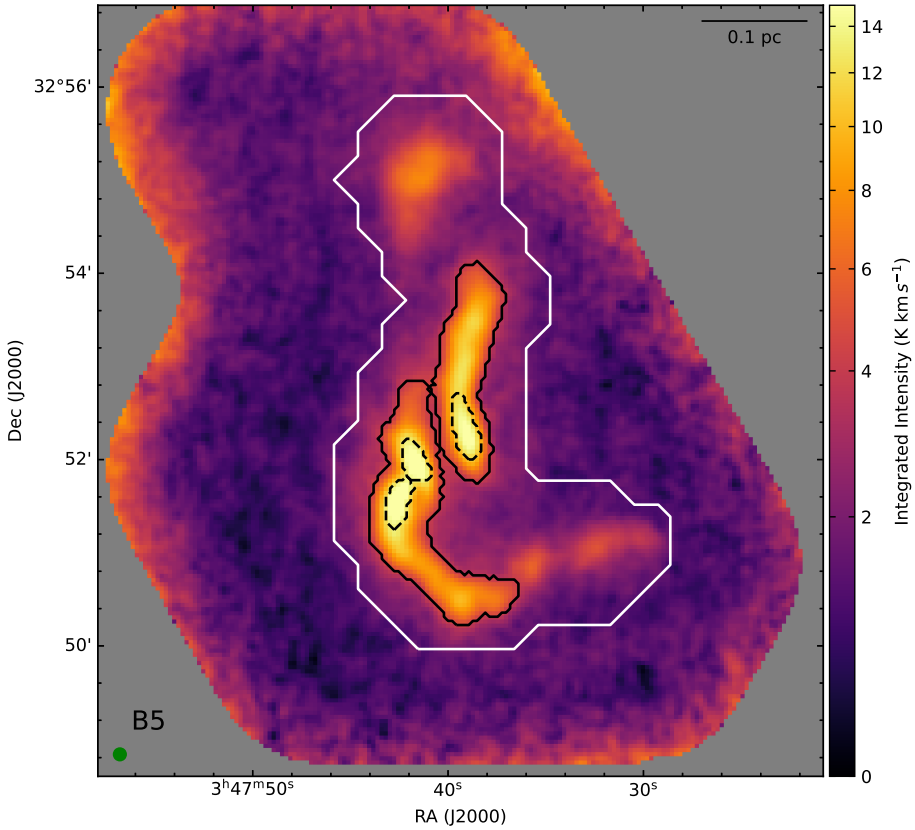

Figure 4.1: Integrated intensity of NH_3 (1,1) in Barnard 5. The black-solid and black-dotted contours show the two filaments and the three condensations in B5, respectively (contours adapted from Schmiedeke et al. 2021). The beam size and scale bar are shown in the bottom-left and top-right corners, respectively. The white-solid contour shows the core boundary calculated with single-dish observations by Pineda et al. (2010).

We smooth the data to a beam of 8″ to increase the sensitivity. This enables us to identify and fit multiple components towards the filaments. The pixel-to-beam ratio is kept at 3 to avoid oversampling. In this work, we follow the nomenclature of Pineda et al. (2015) and Schmiedeke et al. (2021) regarding the different regions in B5 (clumps 1 and 2, filaments 1 and 2, and condensations 1, 2 and 3). Figure 4.1 shows the integrated intensity map for in NH_3 (1,1).

4.4 Analysis

4.4.1 Line fitting

We use the `cold_ammonia` model in the python package `pyspeckit` (Ginsburg & Mirocha 2011; Ginsburg et al. 2022) to fit the NH_3 (1,1) and (2,2) data. This model is appropriate for regions with temperatures $< 40\,K$, and presented by Friesen et al. (2017). The model fits the NH_3(1,1) and (2,2) spectra simultaneously with kinetic and excitation temperatures (T_K and T_{ex}), NH_3 column density (N(NH_3)), velocity dispersion (σ_v), centroid velocity (v_{LSR}), and the ortho-NH_3 fraction of the total NH_3column density (f_{ortho}) as parameters. We follow the Bayesian approach detailed in Sokolov et al. (2020) to fit multiple components and select the optimum number of components in the model.

In classical line fitting procedures, the best-fit model is obtained by minimising the χ^2 parameter:

$$\chi^2(\theta) = \sum_i \frac{(I_i - \mathcal{M}_i(\theta))^2}{\sigma^2} \,, \tag{4.1}$$

where I_i and $\mathcal{M}_i(\theta)$ are the observed and model intensity in channel i, and σ is the noise in the data. θ represents the parameters (see above) that define the model. χ^2 is related to the likelihood function as follows:

$$ln\ \mathcal{L}(\theta) = \frac{\chi^2}{2} + const. \tag{4.2}$$

In the model selection employed in our work, the Bayes factor K^a_b gives the estimate of whether model $\mathcal{M}_a$ is favoured over model $\mathcal{M}_b$:

$$K^a_b = \frac{P(\mathcal{M}_b)Z_a}{P(\mathcal{M}_a)Z_b} \,, \tag{4.3}$$

where $P(\mathcal{M}_\updownarrow)$s are the posterior probability densities and Z_ls are the likelihood integrals over the parameter space :

$$Z = \int_\theta p(\theta)\mathcal{L}(\theta)d\theta \,, \tag{4.4}$$

where $p(\theta)$ are the prior probability densities of the parameters represented by θ. The posterior probability densities can be calculated using the likelihood function as :

$$P(\theta) \propto p(\theta) \times \mathcal{L}(\theta) \,. \tag{4.5}$$

We adopt a threshold of $\ln K^a_b = 5$ to indicate whether model $\mathcal{M}_a$ is preferred over $\mathcal{M}_b$ (following Sokolov et al. 2020).

The initial priors were estimated to accommodate the ranges of these parameters in B5 known from previous works with single-component fits (Pineda et al. 2011a, 2021; Schmiedeke et al. 2021), and further modified if found to be inadequate for the ranges required by the multi-component fits. As the priors in the model, we use uniformly distributed ranges of $6 - 15$ K for T_K, $4 - 12$ K for T_{ex}, $10^{13.2} - 10^{15}$ cm^{-2} for N_{NH_3}, $0.04 - 0.3$ km s^{-1} for σ_v and $9 - 11$ km s^{-1} for v_{LSR}.

Since we only have detections of the ortho-NH_3(1,1) and (2,2) lines, we cannot fit for f_{ortho}. Therefore, for each fit, the ortho-ammonia fraction was fixed at 0.5 (for an assumed ortho-para ratio of unity). Additionally, to reduce the likelihood of spurious components, the minimum separation between two components was required to be 0.1 km s^{-1} (approx. twice the spectral resolution); while the maximum separation between two components was set at 2 km s^{-1} (more than two times the largest velocity gradient across B5) to reduce the parameter space to be covered in the likelihood calculations. After initial runs, we identified that all pixels with a good 1-, 2- and 3-component fits are within a signal-to-noise ratio (SNR) of 4, 7, and 10; respectively [1]. We attempted to fit up to four components to the data and found that three was the maximum number of components in the best-fit model for a region significantly larger than a beam. Figure 4.2 shows the number of components in the best-fit model in different parts of B5. Throughout the core, we are able to fit at least one component (see Figure 4.2); towards the two filaments and the north clump, we could fit two components, and in some regions inside the filaments, we obtain three-component fit as the optimal model.

4.4.2 Component assignment

We detect a single continuous component in the majority of the coherent core, except the two filaments and clump 1. Figure 4.2 shows the number of components towards different parts of B5 core. Since each pixel is fitted independently, and the number of components varies across the map, the identification of spatially coherent features is non-trivial. For this purpose, we start by first grouping the component with the largest extent. To do this, in the regions with two and three components, we search for the fitted component which provides the smoothest map of velocity and the brightness temperature, when combined with the single component in the outer region (see Appendix C.1 for details). This gives us a map of the 'component 1', which has the largest extent. This component shows very similar results as those presented in the single-dish analysis of the region, which is more sensitive to the extended emission, (see Figure 2 in Pineda et al. 2010). We are then left with one or two more components in positions close or towards the filaments. Upon visual inspection of these two components, we find that they are either red- or blue-shifted with respect to the median velocity (v_{med} = 10.15 km s^{-1}) of the extended component. Therefore, we group the remaining two components into red-shifted and blue-shifted components. Each of these two components shows indications of further subdivision in velocity, and therefore, they are split into two components each to give four patchy but dynamically coherent maps. Note that these different velocity components are not shown separately in Figure 4.2, which only shows the number of components in the best-fit model at each pixel.

[1] From visual inspection of the fits at different pixels, we found these SNR cuts to be a good indication of pixels with reliable fits with the respective number of components

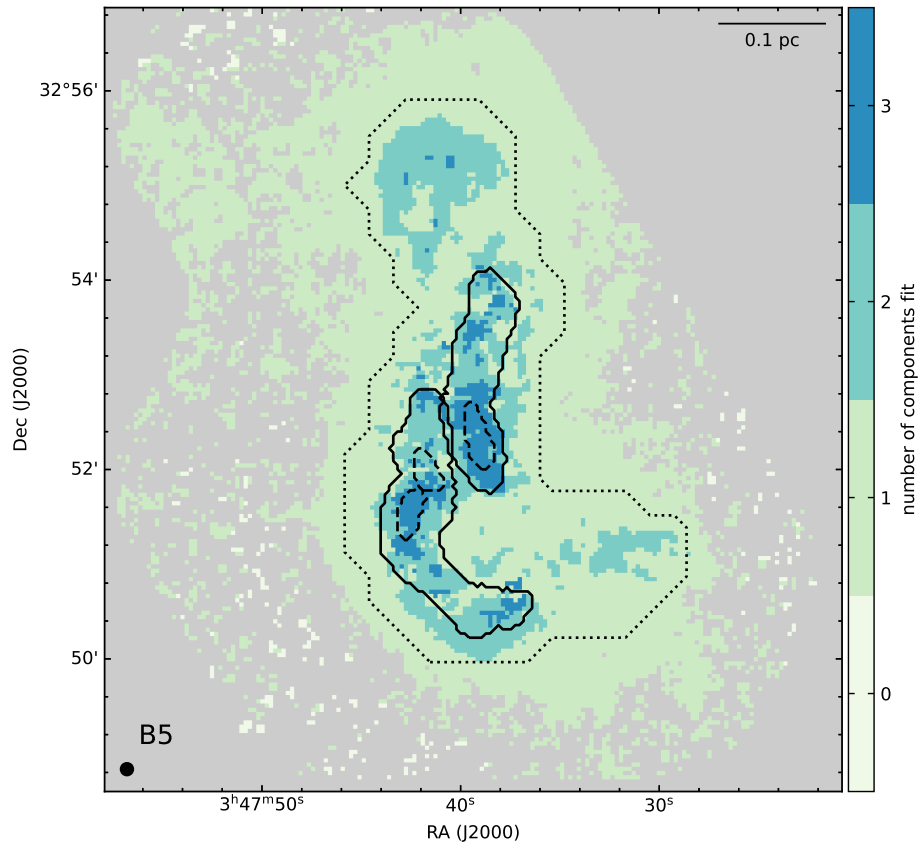

Figure 4.2: Number of components detected towards different parts of B5, as decided by the Bayesian approach described in Section 4.4.1. These components are then grouped according to their velocities (see Section 4.4.2). The black-solid and black-dotted contours show the two filaments and the three condensations in B5, respectively (contours adapted from Schmiedeke et al. 2021). The black-dotted contour shows the boundary of the coherent core in Pineda et al. (2010). The beam size and scale bar are shown in the bottom-left and top-right corners, respectively.

4.5 Results

4.5.1 Identified velocity components

As can be seen from the left panel of Figure 4.3, the extended component shows a smooth and periodic velocity field. As this is also the brightest component, it dominates the velocity obtained from a single component fit to the data. Therefore, this velocity map is very similar to those obtained with a single component fit (Pineda et al. 2011a; Schmiedeke et al. 2021). Inside the core boundary, we link this component to the dense core material, and outside the core boundary, to the ambient cloud.

The four panels on the right of Figure 4.3 show the velocities of the additional components we identify in B5. We refer to these components as ‘far-red’, ‘mid-red’, ‘mid-blue’, and , ‘far-blue’

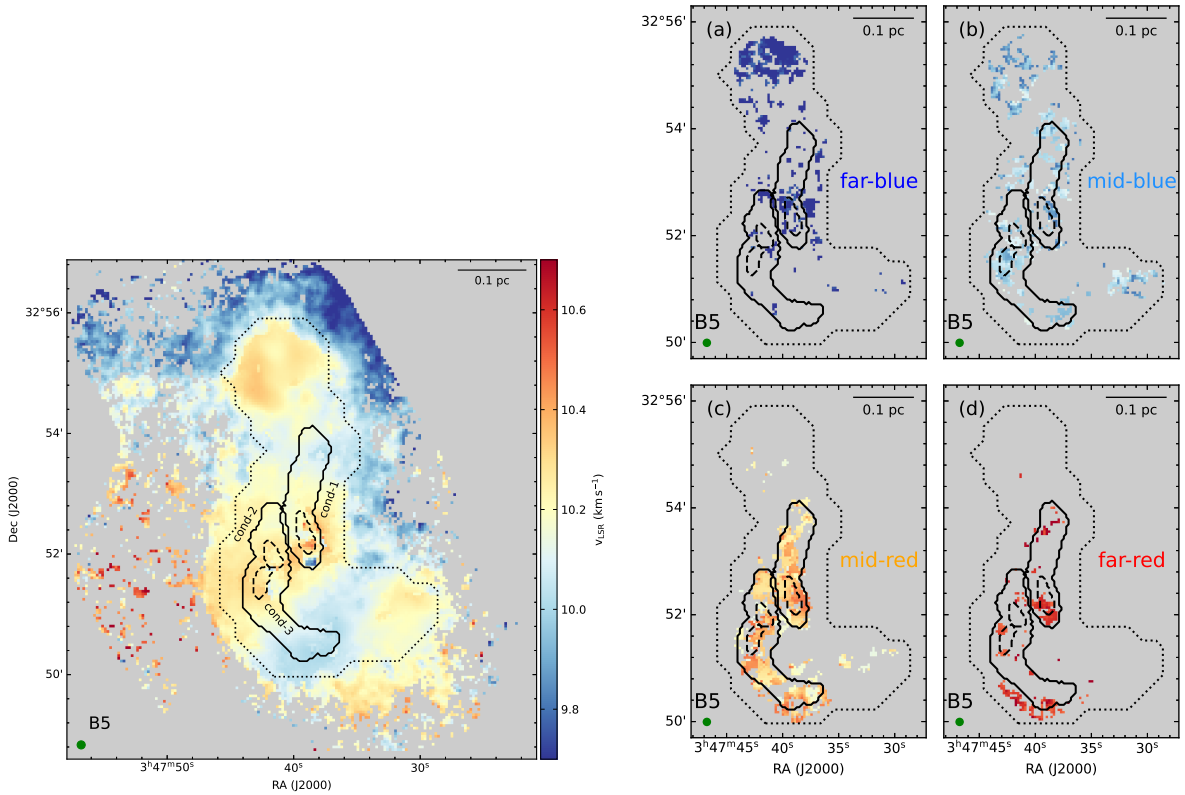

Figure 4.3: *Left* : Velocity map of the extended component. *Right* : Velocity map of 4 additional components. The black-solid and black-dotted contours show the two filaments and the three condensations in B5, respectively. The black-dotted contours show the boundary of the coherent core in Pineda et al. (2010). The scalebar and beam size are shown in the top-right and bottom-left corners, respectively.

(as shown in the figure) according to their red- or blue-shifted velocities. We are cannot detect all four components towards all positions, with a maximum of two (out of the four) components being detected at a given location. This is most likely due to insufficient sensitivity in the map. The mid-blue and the mid-red components seem to trace roughly the two filaments. In the case of filaments showing infall, these two components could be tracing the two opposite sides of material undergoing infall.

The top-left component shows an almost constant velocity around 9.6 km s^{-1}. The location and velocity of this component is consistent with those of the methanol hotspot, which is indicative of gas collision (Wirström et al. 2014; Taquet et al. 2017, observations with *Herschel*, Onsala, and IRAM 30m observatories). Therefore, this component could be tracing material flowing towards B5 from north and north-west. We note that there is a significant apparent gap in the velocity map of this component between the north clump and the central region. This

could be due to some of the material in this component merging with the core material, making it difficult to distinguish from the core component.

The bottom-right component, which is red-shifted at a velocity of $\approx 10.4\,\mathrm{km\,s^{-1}}$, could be largely divided into two parts: the arc-like structure just south of the boundary of filament-2 and a region near condensation 1. The arc-like structure might show material falling into B5 from that direction, similar to the aforementioned scenario towards north, as the velocity in this component is systematically different from the core and filament components (Figure 4.3 left panel and top-right & bottom-left of right panels, respectively). The region near B5-cond-1 might trace material falling towards the condensation due to gravitational collapse.

4.5.2 Filament formation scenarios

Chen et al. (2020a) proposed an analysis to determine whether the filament formation in B5 is dominated by isotropic self-gravitational collapse, or from a slab of gas in a preferred direction. They define the dimensionless parameter C_v to differentiate between the two cases as

$$C_\mathrm{v} \equiv \frac{\Delta \mathrm{v}_h^2}{GM(r)/L}\,, \tag{4.6}$$

where $\Delta \mathrm{v}_h$ is half of the velocity gradient across the filament out to a distance r from the centre, G is the gravitational constant, and $M(r)/L$ is the mass per unit length of the filament at location r. The shape of the velocity profile across the filament constrain the geometry of the gas surrounding the filament, while the parameter C_v determines whether gravity or turbulence/flow dynamics dominates the filament formation.

We determine the boundaries and the spine of the filaments following the analysis of Schmiedeke et al. (2021). We define orthogonal cuts to each filament spines with a separation of roughly one beam between each cut. We calculate the difference in the velocity at the two ends (at the filament boundaries) and the mass per unit length for each of these cuts. We calculate the mass using an NH_3 intensity to mass conversion factor of $1.5\pm0.7\ M_\odot\ (\mathrm{Jy\,beam^{-1}})^{-1}$, derived in Schmiedeke et al. (2021) by comparing the NH_3 (1,1) emission and the 450 μm continuum flux from SCUBA2.

Figure 4.4 shows a few selected examples of the gradient in velocity across the orthogonal cuts to the filaments 1 and 2. The gradients in velocity across all the cuts are shown in Appendix C.3. Figure 4.5 shows the distribution of C_v values across the two filaments. Overall, we find C_v values less than 0.03, and therefore, across these two filaments, the parameter is $\ll 1$. Following the proposed classifications by Chen et al. (2020a), we conclude that both filaments in B5 are formed via collapse dominated by gravity. This is not so surprising, as the M/L in these two filaments is very high, with values above the thermal critical support ($\sim 75\ M_\odot\ \mathrm{pc^{-1}}$, Schmiedeke et al. 2021).

From Figures 4.4, C.2, and C.3, we find velocity gradients across some orthogonal cuts to either filaments suggestive of inclined slab geometry described in Chen et al. (2020a) (8 out of the 34 orthogonal cuts show a difference in velocity of $\geq 0.2\,\mathrm{km\,s^{-1}}$ between the filament boundaries). The fact that we obtain C_v values $\ll 1$ in spite of this geometry, highlights the effect

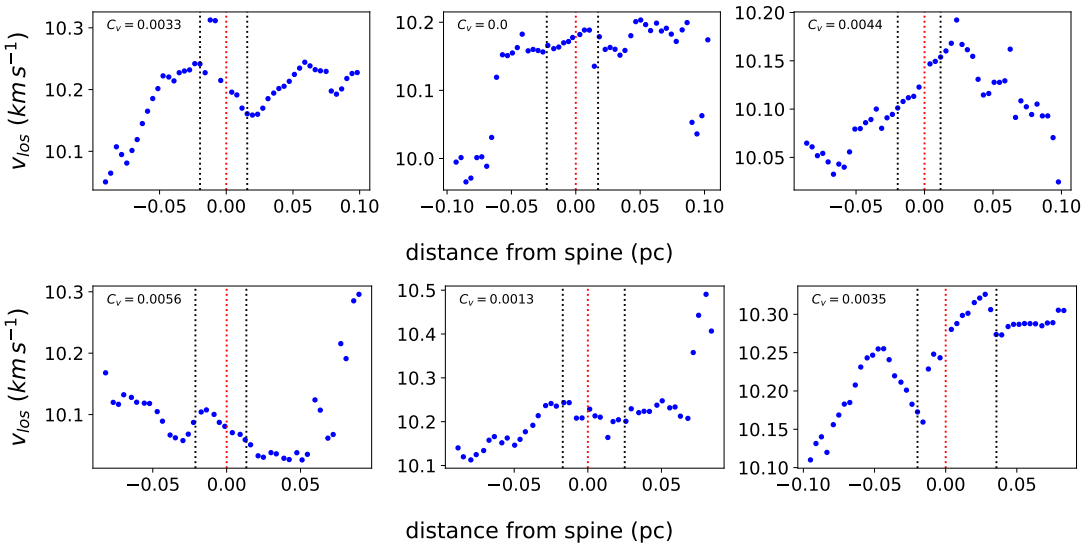

Figure 4.4: Selected examples of the line-of-sight velocity profiles in the orthogonal cuts in Filament-1 (top) and Filament-2 (bottom). The red-dotted vertical lines show the position of the filament spine, and the black-dotted vertical lines show the boundary of the filament for the respective orthogonal cuts shown. The $C_{\rm v}$ parameter (Equation 4.6) calculated for each cut is also shown in the top-left corner.

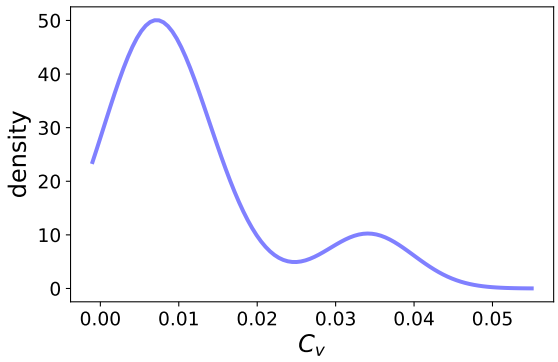

Figure 4.5: Kernel density estimate of the distribution of the $C_{\rm v}$ values across both filaments.

of significantly large M/L. If the slab containing the filament is inclined at an angle with the plane of the sky, the inclination angle, θ, will affect the observed velocity difference across the filament. If $\Delta {\rm v}_h$ is the true velocity difference, and $\Delta {\rm v}_{h,\ obs}$ is the observed velocity difference, then we have

$$\Delta {\rm v}_{h,\ obs} = \Delta {\rm v}_h\ sin\theta\ . \tag{4.7}$$

The true $C_{\rm v}$ value would then be $C_{{\rm v},obs}/sin^2\theta$, where $C_{{\rm v},obs}$ is what we report here. Considering that the largest $C_{\rm v}$ value we obtain across any of the filaments is ≈ 0.03, then the *true* $C_{\rm v}$ value is <1 for any inclination angle $|\theta| > 1.72°$. Therefore, we conclude that it is very unlikely

for the estimated low values of $C_{\rm v}$ to be due mostly to inclination effects.

We derive the intrinsic distribution of $C_{\rm v}$ for both filaments together by using the Kernel Density Estimate (KDE) technique. This distribution, shown in Figure 4.5, highlights how the values have a strong distribution peak below $C_{\rm v} = 0.01$, while there is a smaller secondary peak at ≈ 0.035 which also falls in gravity-dominated regime. This shows that the filament formation was dominated by gravity and that there is little variation in $C_{\rm v}$ along the filaments.

4.5.3 Infall in the filaments

Assuming that both mid-blue and mid-red velocity components (see Section 4.5.1) trace the two opposite sides of infalling material, we can estimate the rate of infall onto the two filaments. The infall rate is then given by

$$\dot{m} = S \times \rho \times {\rm v}_{infall}, \tag{4.8}$$

where S is the surface area of the filament, ρ is the volume density inside the core, and ${\rm v}_{infall}$ is the velocity of the infall, taken to be the mean difference between the red- and blue-shifted filament components. As both the red- and blue-shifted filament components have roughly constant velocities of 10.3 km s^{-1} and 9.9 km s^{-1}, respectively, we take

$${\rm v}_{infall} = \frac{< {\rm v}_{red} - {\rm v}_{blue} >}{2} = 0.2 \text{ km s}^{-1} \tag{4.9}$$

Figure 4.6 shows a schematic of the geometry considered to calculate the approximate surface area of the two filaments. In case of Filament 1, we estimate the surface area assuming the filament to roughly be cylindrical with a diameter, d=0.05 pc and a length, l=0.2 pc. The surface area then is $S = 2\pi(\frac{d}{2})l$. For Filament-2, we estimate the surface area by dividing the filament into two roughly cylindrical regions with diameters d_1=0.07 pc and d_2=0.05 pc, and with lengths l_1=0.14 pc and l_2=0.13 pc, respectively. The total surface area is $S = S1 + S2 = 2\pi(\frac{d_1}{2})l_1 + 2\pi(\frac{d_2}{2})l_2$.

Using the filament masses from Schmiedeke et al. (2021), and the geometry described above, we get a number density of n$\sim 3 \times 10^5$cm^{-3} for the two filaments. With these estimates, we get infall rates of $1.1 \times 10^{-4}\, M_\odot\, {\rm yr}^{-1}$ for Filament 1 and $1.8 \times 10^{-4}\, M_\odot\, {\rm yr}^{-1}$ for Filament 2, which are comparable to the mass infall rate for a Class-0/I protostar (Dunham et al. 2014). For comparison, the total masses of the two filaments are $9.4 M_\odot$ and $13.4 M_\odot$, respectively (Schmiedeke et al. 2021), and therefore it is not a dominant effect on the filament mass budget.

4.5.4 Mass infall onto B5

Assuming the blue-shifted component at a nearly constant velocity of ≈ 9.6 km s^{-1} (top left panel in the right of Figure 4.3) to trace material falling onto B5, we can similarly estimate its rate of infall. We assume that this material flowing through a cylindrical region shown in Figure 4.7, although only one-third of it is detected [2].

[2]For this component, the relatively poor coverage is presumably due to lack of sensitivity (see Section 4.5.1).

Figure 4.6: The geometry considered for mass infall onto Filament-1 (top) and Filament-2 (bottom).

We then estimate the rate of infall of material onto B5 using Equation 4.8. We assume a number density of n$\sim 10^4$cm^{-3}, characteristic for core material. As the mean velocity in the core around this region is $\approx 10.2\,\mathrm{km\,s^{-1}}$ (Figure 4.3), we take the infall velocity to be $0.6\,\mathrm{km\,s^{-1}}$ (as the blue-shifted material is at v = $9.6\,\mathrm{km\,s^{-1}}$). We then obtain a mass infall rate of $2.9 \times 10^{-5}\,M_\odot\,\mathrm{yr^{-1}}$ onto B5. We note that this is an upper limit of the mass infall rate, as this component is sparsely sampled.

Using observations with HC_7N, Friesen et al. (2013) calculated a lower limit of $2 - 5 \times 10^{-6} M_\odot\,\mathrm{yr^{-1}}$ for accretion onto dense filaments in the Serpens South, which is a cluster-forming region. As HC_7N traces a lower density compared to NH_3, the infall observed by Friesen et al. (2013) is likely at a different region in the line of sight. The observation of different regions of mass infall with comparable rates might point to the existence of a mechanism through which new material is being delivered to coherent cores. In Choudhury et al. (2021), we also discuss possible material accretion onto coherent cores. Could we observe infall onto cores with suitable tracers of different densities in different star-forming regions? If accretion of new material onto the core is observed in more regions, there could be a need for a significant update to the current core evolution models, where cores are assumed to evolve in isolation.

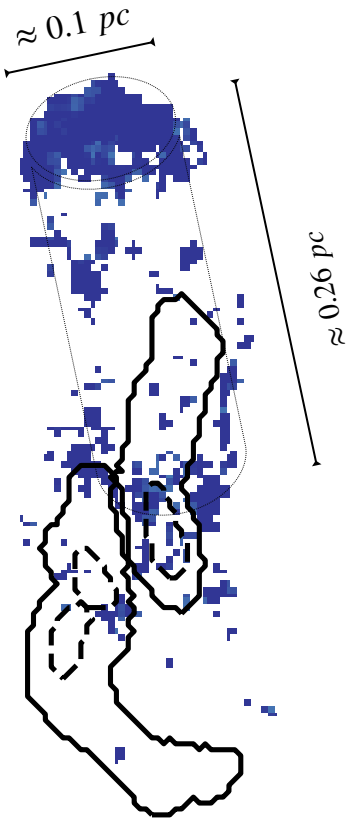

Figure 4.7: The geometry considered for mass infall onto B5.

4.6 Conclusions

We use combined GBT and VLA observations of star-forming core Barnard 5 in Perseus to study the multi-component structure of the core. our results can be summarised as follows:

1. By smoothing the data to a beam of 8″ (the original beam was 6″), we are able to fit the different components. Apart from the brightest component (which dominates the properties of the single component fit), we detect four separate velocity components.

2. We detect two components, separated by 0.4 km s^{-1}, towards both the filaments in B5. We postulate that these two components likely trace the two opposite sides in the line of sight of material contracting within the filaments.

3. Following the criteria described by Chen et al. (2020a), we conclude that the infall in both the filaments appears to be isotropic and gravity-dominated, as opposed to filament formation in a slab.

4. Assuming simple geometry and uniform density inside the core, we estimate the rate of infall of material onto the two filaments to be 1.1×10^{-4} M$_\odot$ yr^{-1} and 1.8×10^{-4} M$_\odot$ yr^{-1},

respectively for Filament-1 and Filament-2. These rates are comparable to mass accretion rates in Class-0/I protostars.

5. We also obtain an upper limit of $2.9 \times 10^{-5}\,M_{\odot}\,yr^{-1}$ for the rate of infall of mass onto B5 from north. This rate is comparable to the rate of infall onto dense filaments in Serpens South.

Chapter 5

Summary and Future Work

In this thesis, I have presented results from three projects using molecular line observations of dense gas tracers in nearby star-forming regions with a focus on studying the properties of dense cores, which are the progenitors of stars. Here, my findings are briefly summarised.

5.1 Conclusions

In Chapter 2, we carried out a detailed analysis of the cores and their surrounding environment. We separated the cloud component from the dense core component to study, for the first time, both components simultaneously. We studied the effect of the ambient cloud component in the line-of-sight towards the cores in the molecular cloud L1688 in Ophiuchus. Using stacked spectra, we increased the sensitivity significantly at the cost of spatial resolution, and were able to detect and disentangle the faint cloud component towards all the coherent cores in L1688. We showed that if inadequate sensitivities do not allow for the detection of this faint cloud component, the resultant one-component fit to the core spectra leads to overestimate of the core properties including temperature and velocity dispersion, which are overestimated by 10% and 28%, respectively. At the low temperatures of dense cores, this temperature overestimate is significant, as it affects the chemistry on surfaces of dust grains significantly. Also, overestimates of these parameters affect our calculation of the dynamic stability of the cores. We also see evidence of two velocity components in the L1688 cloud, and suggest that collision between these two components might result in a local density increase and aid in the formation of the coherent cores. Our results highlight the need for high-sensitivity observations.

Next, we take a closer look at the transition from turbulent molecular cloud to coherent cores in L1688 in Chapter 3. We use NH_3 observations and obtain, for the first time, an extended map of the gas kinetic temperature map that includes the dense cores as well as the surrounding molecular cloud, using a single density tracer. Using a single-component fit to the data, we are able to reproduce previous results in low-mass regions for the changes in temperature, velocity dispersion and abundance from core to cloud. We then stack the spectra towards the coherent cores and their immediate neighbourhood, and study the transition by separating the core and cloud components. Contrary to previous results, we find that the transition to coherence at the

core boundary is rather gradual. We also detect the subsonic material to extend up to 0.1 pc outside the boundaries of dense cores, which has not been previously observed. This extended subsonic material could be accreted by the core, thereby changing its mass. It also modifies our picture of dense cores to a more dynamic scenario, where mass is added to the core even in its later evolution stages. This will alter the currently used core evolution models, where cores are treated as isolated structures with fixed mass.

The third part, presented in Chapter 4, focuses on filamentary structures inside the coherent core Barnard 5 in Perseus. We used combined data from a single-dish telescope and an interferometer to obtain high-resolution observations towards the core. With multi-component analysis, we were then able to detect two velocity components associated with the two filaments. These components likely show evidence of infall of material onto the filaments. We also showed that, primarily due to the significantly large mass-per-unit-length, the formations of the filaments were likely dominated by collapse due to gravity and not by turbulent contractions. We also find hints of material falling into the core, mainly from the north. Our results suggest that with high-sensitivity, high-resolution observations, we could better characterise the internal structure of the core and possibly look at the ongoing mass infall in detail.

In summary, this thesis used the kinematical information obtained from different NH_3 observations to modify our picture of dense cores. Emission in the line-of-sight towards dense cores could still be contaminated with emission from the surrounding molecular cloud, which results in overestimate of the temperature and level of turbulence inside the core. We also show that dense cores can show evidence of accretion, indicating that they still receive more material from their surroundings.

5.2 Future Outlook

Our results from Chapters 2 and 3 show that with adequate sensitivities, we are able to detect the core and cloud components in the same line-of-sight towards the vicinity of the coherent cores in L1688. This provides a unique possibility to explore the physical properties and their transition individually in these two components. However, it remains to be seen whether such observations could be reproduced in other star forming regions. Due to relatively higher ambient density in L1688, the NH_3 emission in this cloud is significantly more extended than similar regions in other molecular clouds, such as Perseus and Taurus. So a natural follow-up would be to look at available data towards other nearby molecular clouds to see if this study could be repeated. Some such observations are already available from the Green Bank Ammonia Survey (GAS). Similar observations towards other regions will strengthen the result being ubiquitous in molecular clouds. I plan to conduct a statistical survey of these nearby star forming regions to see how often, and to what extent, the subsonic material is observed outside the dense core boundaries.

In our study of L1688 cores, we had to stack the spectra towards cores and their neighbourhood to achieve the required sensitivity. This meant that we had a poor resolution in our two detected components. Therefore, we could not look at the spatial distribution and variance of the components. High-sensitivity observations are required to complement our findings and explore,

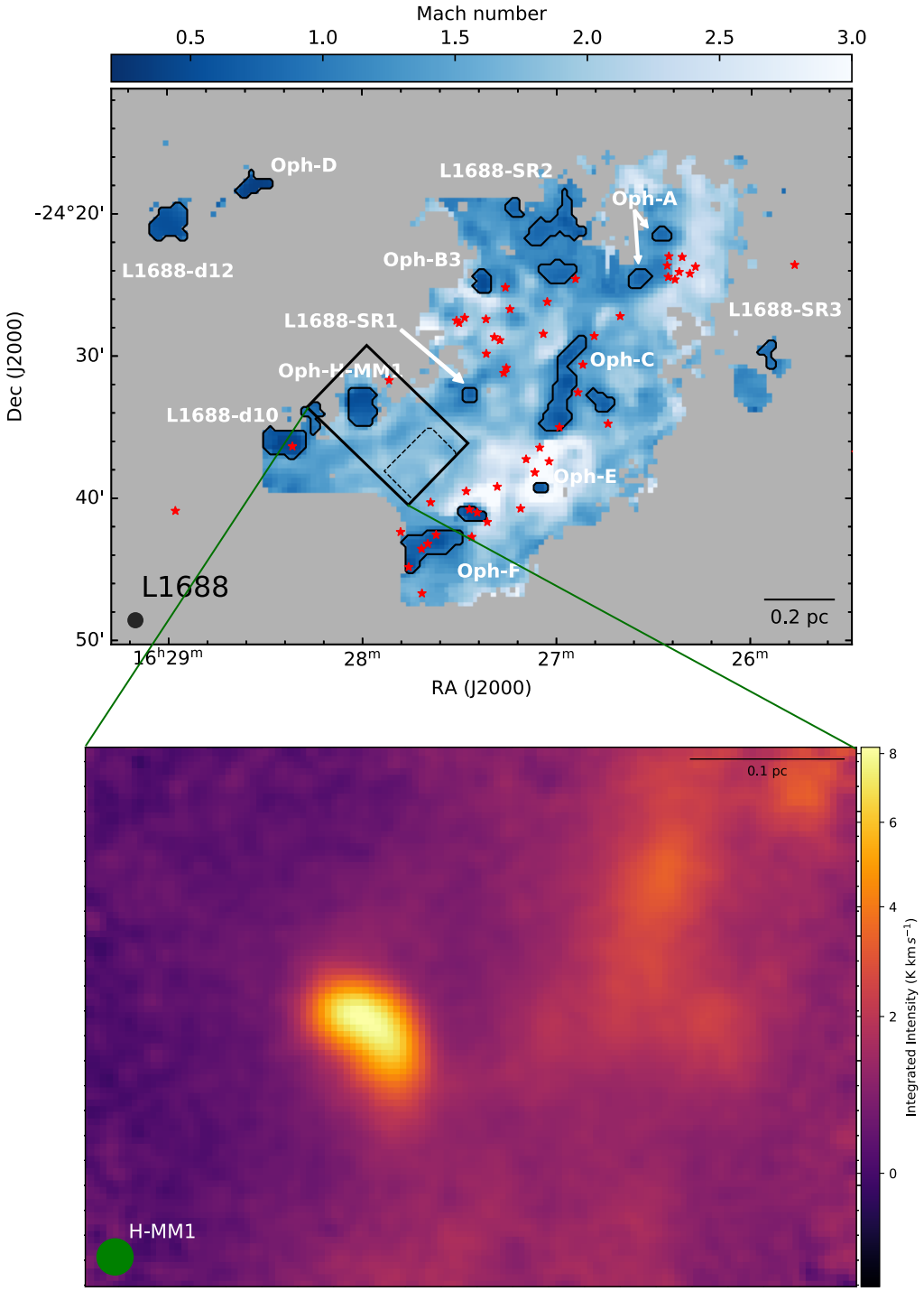

Figure 5.1: *Top*: Mach number in L1688, with the coherent cores and the protostars shown; same as Figure 2.1. The black-solid rectangle shows the area targeted in the new GBT observations. *Bottom*: Integrated intensity of the NH_3 (1,1) spectra. The beam and the scale-bar are shown in the bottom-left and top-right corners, respectively.

for instance, the distribution of the subsonic component outside the cores. This will enable us to observe if the subsonic material is present in narrow, fibre-like structures connecting the cores to the cloud (Pineda et al. 2011b; Hacar et al. 2018). The existence of such structures connecting the cloud to the core will be an important addition to our current understanding of cores, as it challenges the generally accepted picture of dense cores evolving in isolation, kinematically disentangled from the natal cloud. This could also help us connect to the recent observations of streamers feeding material from outside the dense cores into early protoplanetary disks (e.g. Pineda et al. 2020). With this objective, I recently completed high-sensitivity observations of the neighbourhood of a prestellar core in L1688 with the Green Bank Telescope (GBT). Figure 5.1 shows the area observed during this project, as well as the NH_3 (1,1) integrated intensity map from the observation. The total time allotted for this observation was 72h, and we targeted the prestellar core H-MM1 and its neighbouring molecular cloud. The data from these deeper GBT observations will allow for the detection of the two components in the native resolution in the vicinity of the core. We will be able to look for the presence of substructures and quantify the amount of material in the extended subsonic component beyond the core boundaries.

Another exciting follow-up to our results presented here would be observations of these regions with other density tracers such as HCO^+, HCN and CH_3OH. For this purpose, proposals will be submitted to GBT, IRAM 30m, Taeduk Radio Astronomy Observatory (TRAO), and James Clerk Maxwell Telescope (JCMT). The data from these observations will make use of the tools developed in the course of the projects presented in this thesis so that we can make similarly complete and detailed analyses. This will allow for a study of the densities associated with the structures we observe inside and around dense cores. For our results from Chapter 4, such a follow-up will also allow us to look for the source of the material possibly being accreted onto the core and the filaments inside it. One key result from these future studies would be the quantification of the mass that could be accreted by the core and the protostar throughout their evolution. This could imply the necessity of a significant update to our understanding of the dense core evolution and star formation process.

Appendix A

Appendices for Chapter 2

A.1 Calculation of non-thermal velocity dispersion, $\sigma_{\rm NT}$

The non-thermal component of the velocity dispersion is calculated by removing the thermal dispersion for the observed molecule ($\sigma_{\rm T}$) from the total observed velocity dispersion ($\sigma_{\rm v}$) :

$$\sigma_{NT}{}^2 = \sigma_{\rm v}{}^2 - \sigma_{T,{\rm NH_3}}{}^2 - \sigma_{chan}{}^2 \,, \tag{A.1}$$

where σ_{chan} is the contribution due to the width of the channel and the thermal component of the dispersion observed in NH_3 is

$$\sigma_{T,{\rm NH_3}} = \sqrt{\frac{k_B T_k}{\mu_{\rm NH_3}}} \,, \tag{A.2}$$

with $\mu_{\rm NH_3}$ = 17 amu, being the mass of the ammonia molecule. The typical values of $T_{\rm K}$ and $\sigma_{\rm v}$ in this study are 14 K and 0.2 km s^{-1}, respectively (see Section 2.5.1). At $T_{\rm K}$=14 K, the thermal component, $\sigma_{T,{\rm NH_3}}$ is 0.082 km s^{-1}.

When a Hann-like kernel is used in the spectrometer, then the correction factor for the measured velocity dispersion is given by (see Leroy et al. 2016; Koch et al. 2018)

$$\sigma_{chan} = \frac{\Delta}{\sqrt{2\pi}}(1.0 + 1.18k + 10.4k^2) \,, \tag{A.3}$$

where Δ is the spectral resolution and k is dependent on the Hann-like function applied. In the case of the VEGAS spectrometer used in the GAS observations, k is 0.11, which corresponds to a correction term of

$$\sigma_{chan} = \frac{\Delta}{1.994} = 0.036\,{\rm km\,s^{-1}} \,. \tag{A.4}$$

After applying this small correction, we obtain a typical non-thermal component of the velocity dispersion, σ_{NT} = 0.182 km s^{-1}.

A.2 Coherent cores

As mentioned in Section 2.4.2, we identify 12 regions in L1688 as coherent cores. These include:

- five cores, Oph-A, Oph-C, Oph-D, Oph-E and Oph-F, which were identified in continuum emission (Motte et al. 1998),
- one DCO^+ core, Oph-B3 (Loren et al. 1990; Friesen et al. 2009)
- two coherent 'droplets', L1688-d10 and L1688-d12, (Chen et al. 2019), and
- one prestellar core, Oph-H-MM1 (Johnstone et al. 2004).

Apart from these previously identified cores, we also identified three more subsonic regions : L1688-SR1 (south of Oph-B1 in Motte et al. 1998), L1688-SR2 (three islands east of Oph-A), and L1688-SR3 (near the western edge of the map). Ladjelate et al. (2020a) identifies a prestellar core at the position of SR1 and an unbound starless core at the position of SR3. SR1 and SR3 are associated with a local peak in NH_3 integrated intensity. SR2 does not contain any bound core in the Herschel data, nor does it show a local NH_3 peak.

Oph-B3, Oph-D and H-MM1 are also identified as L1688-c4, L1688-d11 and L1688-d9, respectively, in Chen et al. (2019). The two structures that we identify as Oph-A are likely associated with Oph A-N2 and Oph A-N6, as identified in N_2H^+ by Di Francesco et al. (2004). The continuum cores Oph-B1 and Oph-B2 from Motte et al. (1998) are not subsonic (Friesen et al. 2009) and, therefore, they are not considered as 'coherent cores' by our definition.

A.3 Checking effect of smoothing the data on the final results

To check if there is any effect due to smoothing the data (see Section 2.3), we performed the same averaging on the original GAS data, using the velocity map published in DR1 for aligning the spectra. Since the DR1 velocity map was not as extensive, this test could not be performed for all the cores, as we need the velocity information to align the spectra. In the cores where this check was possible, the results from the new fits were not significantly different (≈1.4% change in T_K and ≈4.7% change in σ_v). In comparison, the difference in the estimates from the narrow component and from single-component fit results were 10% in T_K and 28% in σ_v (Section 2.5.4).

A.4 Fitting the average spectra in the cores

To fit the average spectra in cores, we followed the same process as described in Section 2.4.1. We used the module `specfit` in `pyspeckit` to fit single spectra. Since we were fitting the spectra towards the cores, we used, as our initial guess, slightly lower values of 12 K and 4 K for T_K and T_{ex}, respectively. As the spectra are aligned at v=0, we used v_{LSR}=0.0 km s^{-1} as our initial guess. For σ_v, we used the mean value inside all cores, which is $\sigma_v \approx 0.19$ km s^{-1}, from the extended velocity dispersion map obtained from the fit process described in Section 2.4.1.

While fitting two components to the spectra, we added a two-component `cold_ammonia` model as a new model in the fitter. We then used this model to fit the spectra. As the residuals from single-component fits suggest the presence of a narrow and a broad component, we used two values, one from each side of the guess used in the single-component fit (0.19 km s^{-1}) as our

initial σ_v guesses for the two components. After checking the fit with varying initial guesses, we found that small differences in T_K and v_{LSR} in the initial guesses also aid in arriving at a stable fit. Therefore, we used the following initial guesses in the two-component fits:

- $(T_K)_1 = 11$ K
- $(T_{ex})_1 = 4$ K
- $(\sigma_v)_1 = 0.15$ km s^{-1}
- $(v_{LSR})_1 = 0.0$ km s^{-1}
- $(T_K)_2 = 16$ K
- $(T_{ex})_2 = 4$ K
- $(\sigma_v)_2 = 0.3$ km s^{-1}
- $(v_{LSR})_2 = 0.25$ km s^{-1}

A.5 Model selection using AIC estimator

We fitted the averaged spectra considering models with a different number of components in ammonia, with each component being modelled as a `cold_ammonia` spectrum in `pyspeckit`. The number of parameters used in the models is five per component. To select the best model to fit a spectra, we checked the Akaike Information Criterion (AIC), which determines if the quality of the model significantly improves considering the increase in the number of parameters used. Assuming that each channel in the spectra has a constant Gaussian error, which is equal to the noise in the spectra, AIC is related to the χ^2 of the data as :

$$AIC = 2k + \chi^2 + C, \tag{A.5}$$

where k is the number of parameters used to model the data and C is a constant, which depends on the noise in the spectra, and is given by :

$$C = -2N \times \ln\left(\frac{1}{\sqrt{2\pi\sigma^2}}\right), \tag{A.6}$$

where N is the number of channels in the spectra.

The model with the lowest AIC value is considered to be the best model. In our case, the channels are not completely independent and, therefore the actual number of independent channels is different. This effect, however, is systematic and it does not change for models with different number of components. The change in the AIC value from one model to another is the important term, and the actual AIC values are less significant.

Using Equation A.5 we can rewrite the change in AIC value from a single-component fit to a two-component fit, Δ_{AIC}, as

$$\Delta_{AIC} = 2\Delta k + \Delta\chi^2 \, , \tag{A.7}$$

where Δk is the change in number of parameters and $\Delta\chi^2$ is the change in χ^2, from a single-component fit to a two-component fit. Each model component uses five independent parameters and, therefore $\Delta k = -5$. Also, $\Delta\chi^2$ can be divided into two groups: channels with and without emission, or

$$\Delta\chi^2 = (\Delta\chi^2)_{\textit{with emission}} + (\Delta\chi^2)_{\textit{without emission}} \, . \tag{A.8}$$

Outside the emission region the models are identical and, therefore,

$$\Delta\chi^2 = \frac{n_{line}}{\sigma^2}\left(rms^2_{emission,\ 1-comp} - rms^2_{emission,\ 2-comp}\right) , \tag{A.9}$$

where, n_{line} is the number of channels with emission, σ is the noise in the spectra, and $rms_{emission}$ is the residual root mean square (rms) of the model in the emission region. The comparison of the $\sigma_{emission}$ and the noise, σ, is taken as a measure of determining the goodness of the fit in line-fitting software, such as CLASS in GILDAS[1]. Then, in our comparison of single- and two-component fits, we have

$$\Delta_{AIC} = -10 + \frac{n_{line}}{\sigma^2}\left(rms^2_{emission,\ 1-comp} - rms^2_{emission,\ 2-comp}\right) . \tag{A.10}$$

We note thatn_{line} depends on the width of the spectra and, therefore, it is different for each coherent core. From Equation A.10, we see that for a low variation in the AIC, the improvement in the residuals of the fit is also small. We find that for the two coherent cores with low Δ_{AIC} (<30), d12 and SR3, the improvement in the $rms_{emission}$ is less than 10% of the noise in the respective spectra. For the ambient cloud spectra, with Δ_{AIC} =94, $rms_{emission}$ improves by 10% of the noise level, from a single-component to a two-component fit. For every other region, we see an improvement in $rms_{emission}$ by >15%.

Owing to our limited number of data points, it is not possible to definitively determine what change in AIC represents a significant improvement in the fit upon the addition of the second component. From the corresponding improvement in $rms_{emission}$, we note that in our current work, only the regions with $\Delta_{AIC} > 150$ show a significant improvement in the fit.

A.6 Average spectra of the whole cloud

Figure A.1 shows the average (1,1) and (2,2) spectra in the whole L1688, which was mapped by the Green Bank Ammonia Survey (GAS). These spectra were used to determine the range of centroid velocity, for which a fit is attempted with `pyspeckit`.

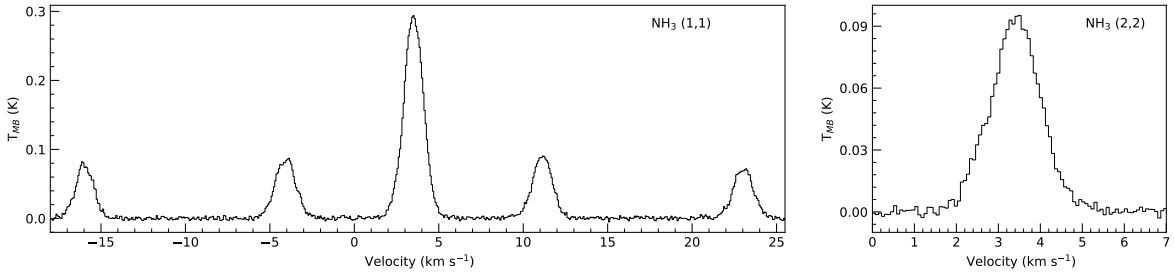

Figure A.1: Average NH_3 (1,1) and (2,2) spectra in L1688.

[1] `http://www.iram.fr/IRAMFR/GILDAS`

A.7 Averaged spectra towards cores

Figures A.2 to A.12 show the average spectra in all of the other coherent cores studied here, with single- and two-component fits, similar to Oph-F in Figure 2.2. The kinetic temperature, velocity dispersion, centroid velocity and para-ammonia column densities determined from these single- and two-component fits are presented in Table A.1. The rms noise in the spectra of each core is also shown in the same table.

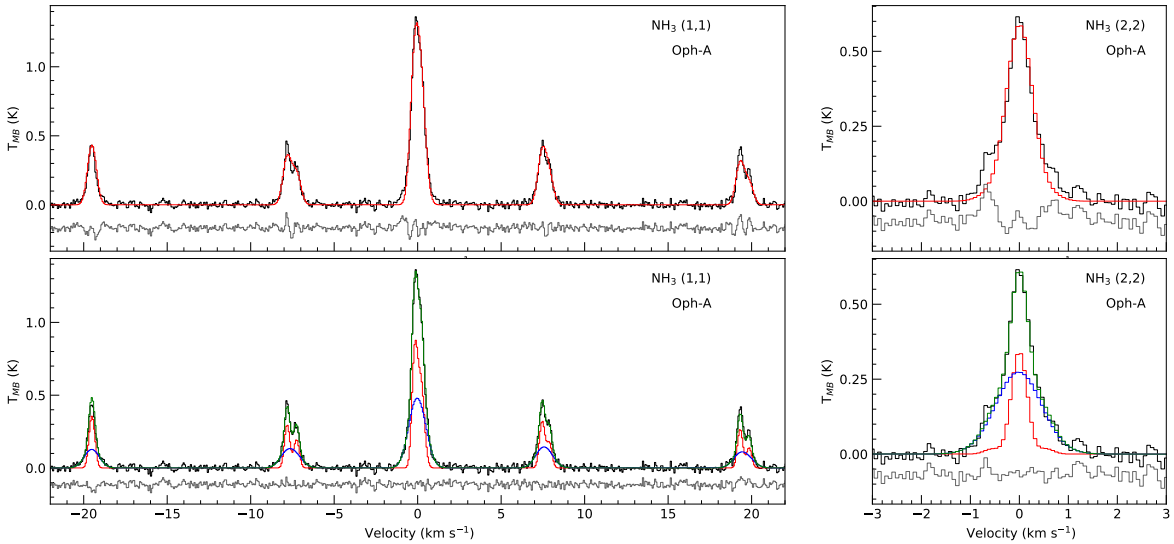

Figure A.2: Top panels: Average NH_3 (1,1) and (2,2) spectra of Oph-A core, with a single-component fit. Bottom panels: Same spectra, with two-component fit (green). The narrow (red) and broad (blue) components are also shown separately.

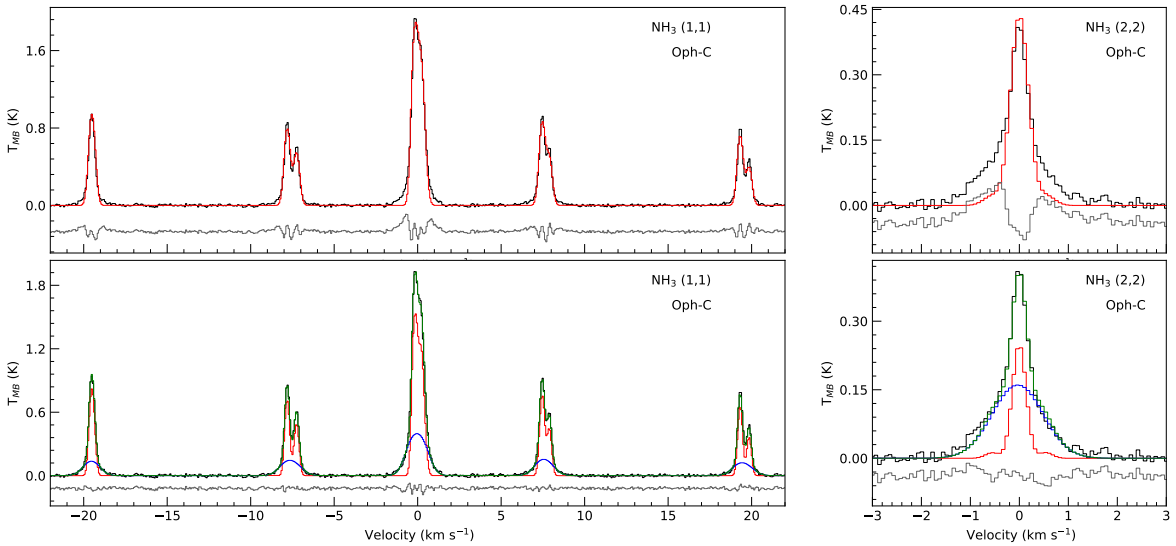

Figure A.3: Same as Figure A.2, but for Oph-C.

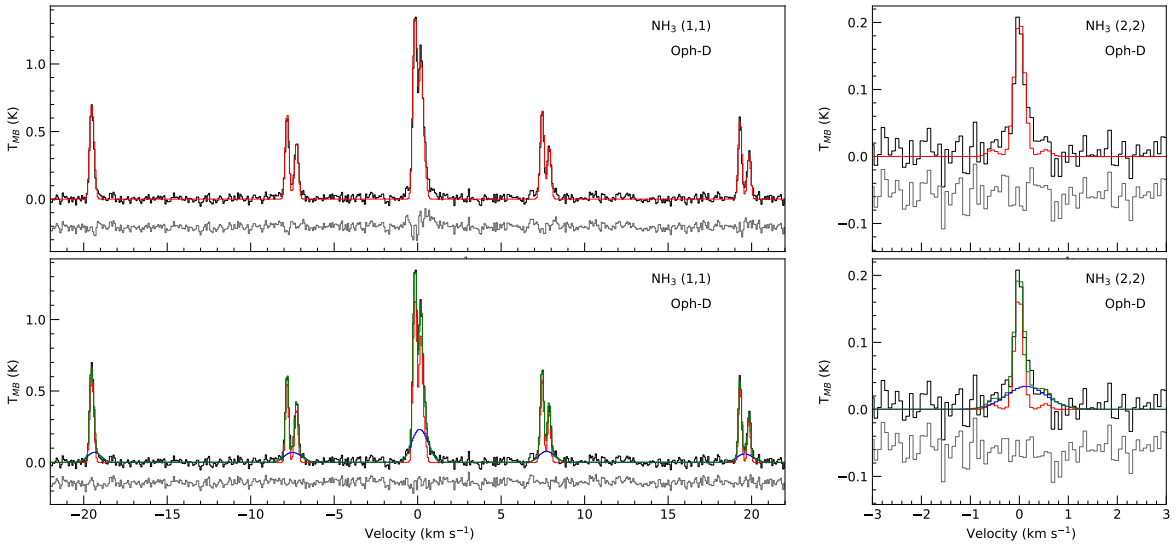

Figure A.4: Same as Figure A.2, but for Oph-D.

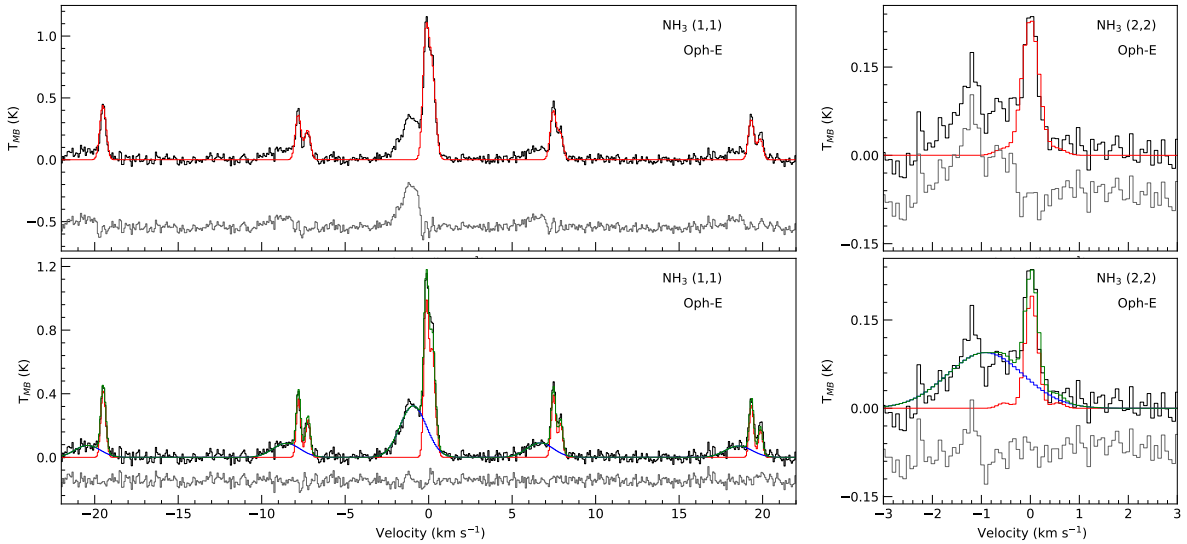

Figure A.5: Same as Figure A.2, but for Oph-E.

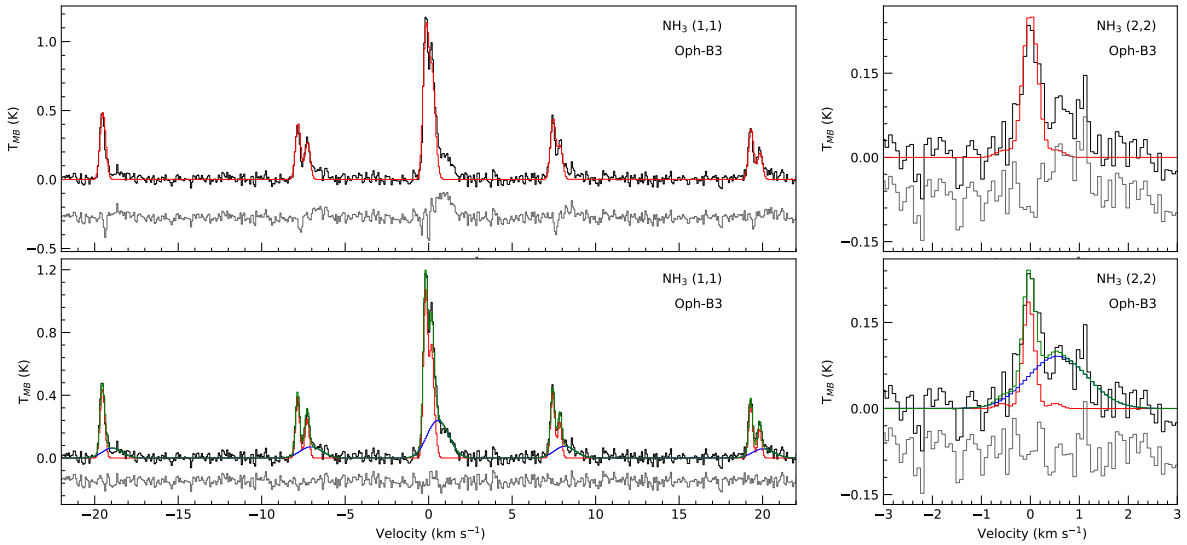

Figure A.6: Same as Figure A.2, but for Oph-B3.

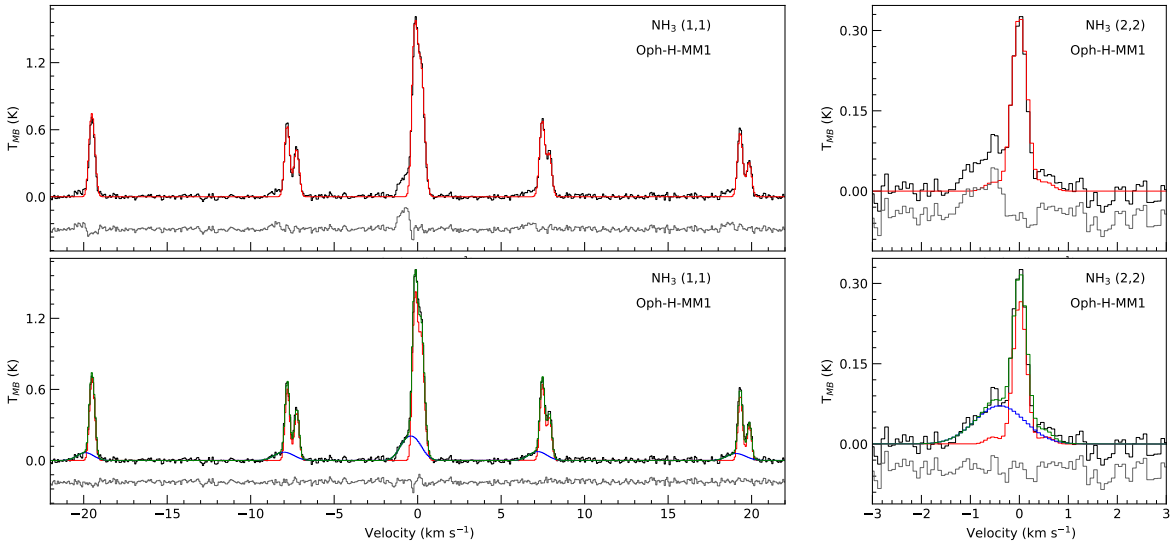

Figure A.7: Same as Figure A.2, but for Oph-H-MM1.

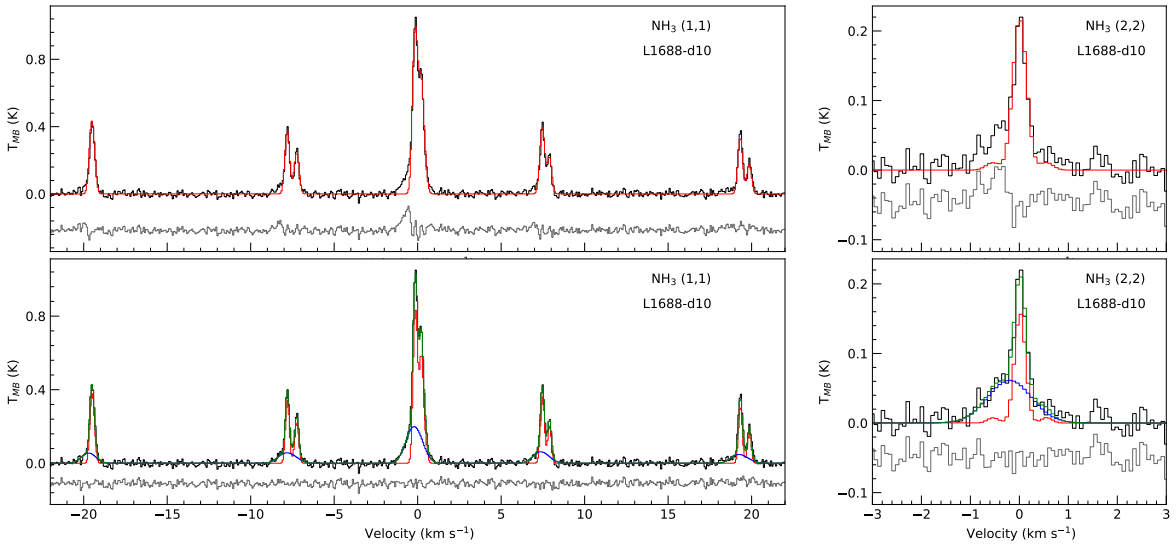

Figure A.8: Same as Figure A.2, but for L1688-d10.

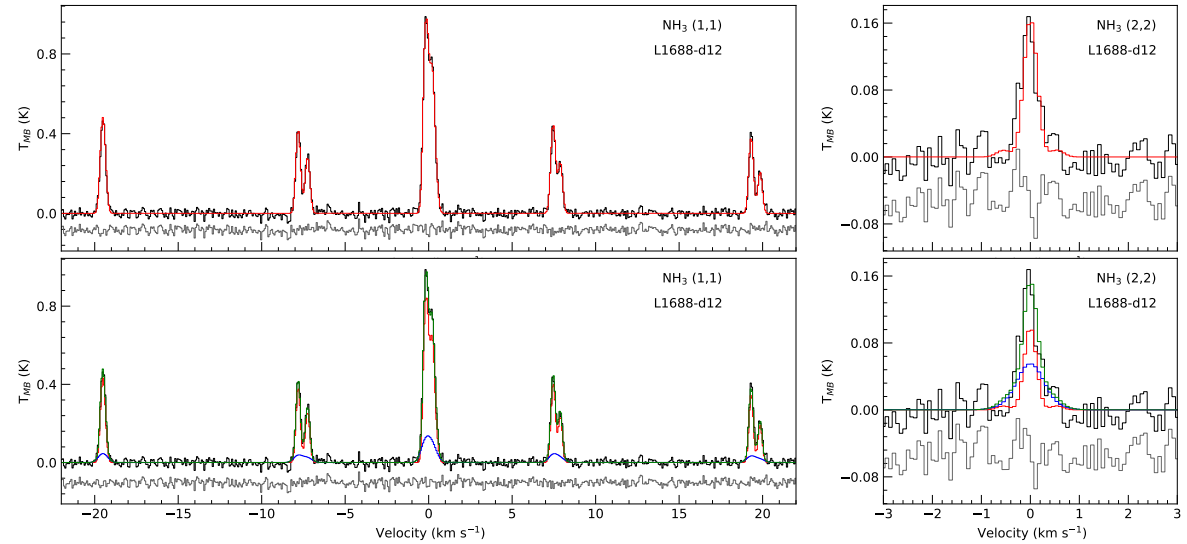

Figure A.9: Same as Figure A.2, but for L1688-d12.

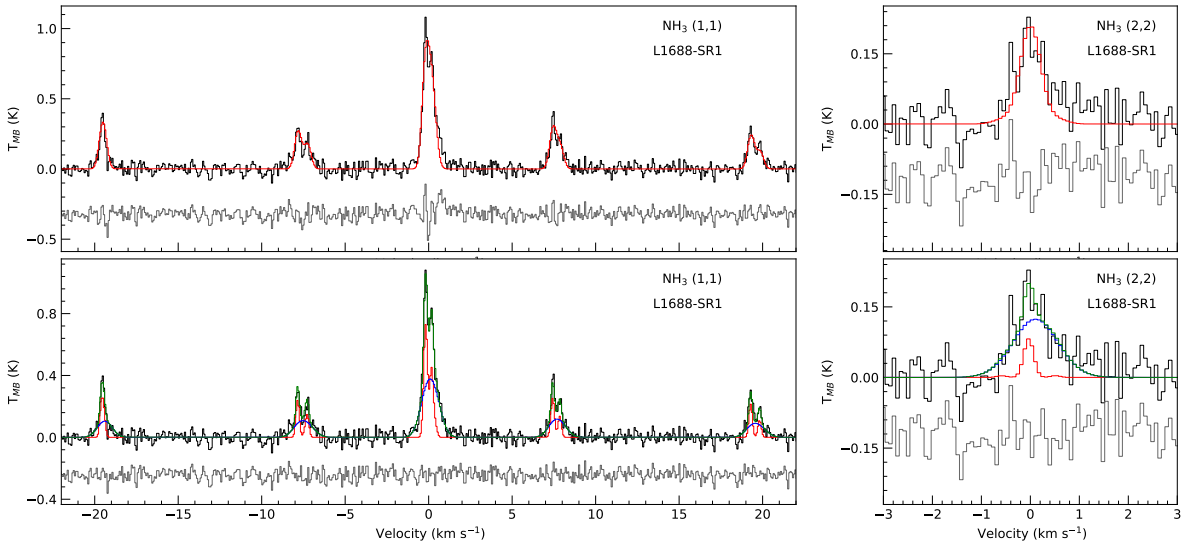

Figure A.10: Same as Figure A.2, but for L1688-SR1.

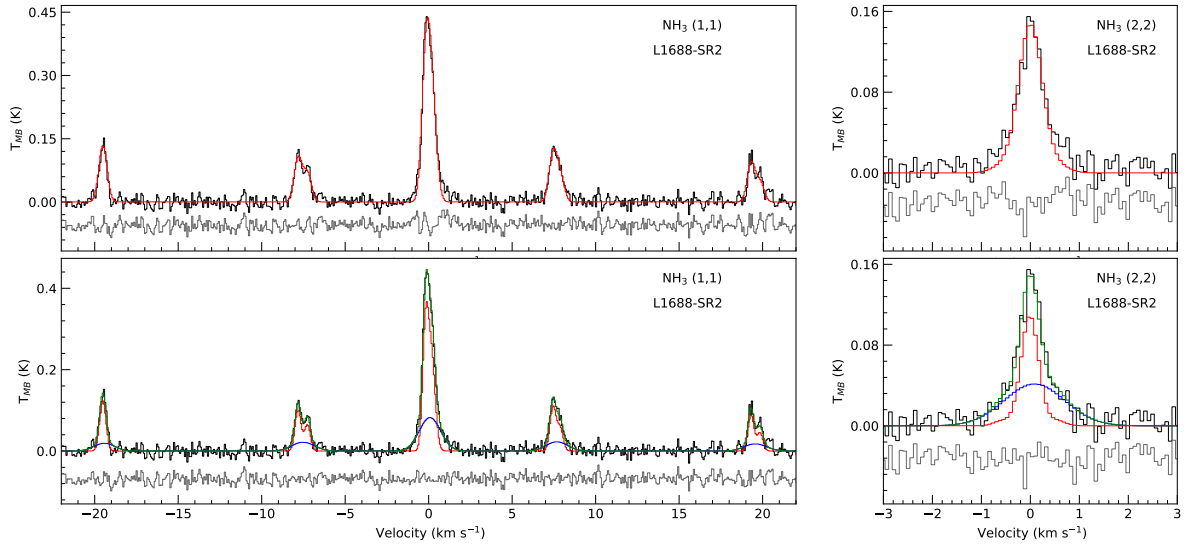

Figure A.11: Same as Figure A.2, but for L1688-SR2.

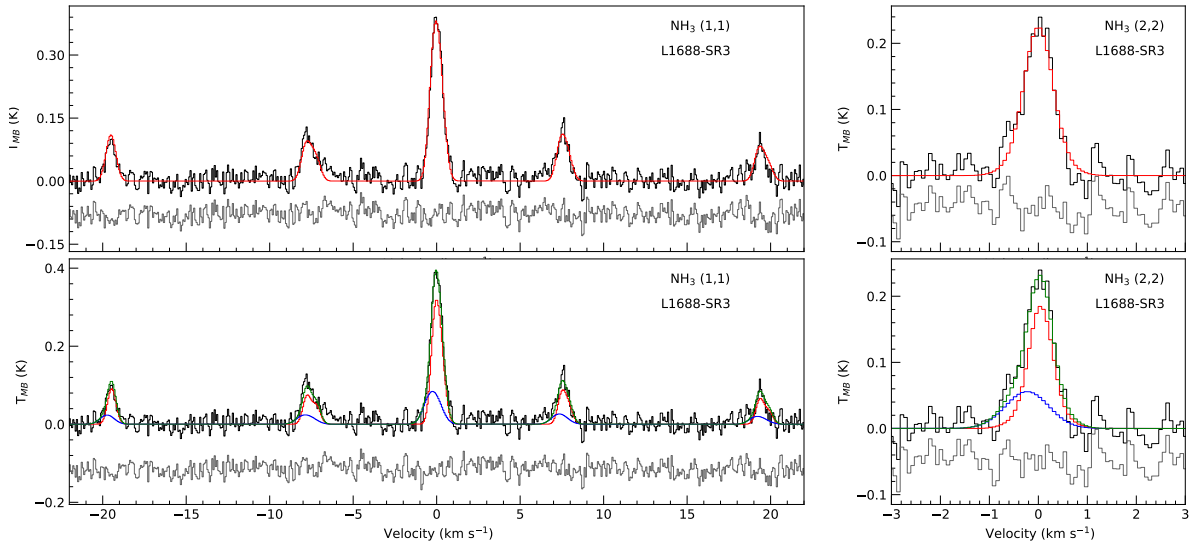

Figure A.12: Same as Figure A.2, but for L1688-SR3.

Table A.1: Best-fit parameters for one- and two-component fits in cores

Core	Component [a]	T_K (K)	σ_v [b] (km s^{-1})	v_{rel} [c] (km s^{-1})	log(N(p-NH_3) /(cm^{-2}))	$\mathcal{M}_s$	noise[d] (mK)	Δ_{AIC} [e]	$T_{K,GAS}$ (K)	$\sigma_{v,GAS}$ (km s^{-1})
	Single	19.1(2)	0.253(3)	0.0[f]	13.86(2)	0.9			19(1)	0.23(1)
Oph-A	Narrow	15.8(4)	0.156(4)	-0.001(2)	13.74(4)	0.6	17	761		
	Broad	24.9(8)	0.44(1)	-0.014(6)	– [g]	1.5				
	Single	11.72(9)	0.177(1)	0.0[f]	14.168(5)	0.8			12.1(5)	0.174(8)
Oph-C	Narrow	10.13(9)	0.1376(8)	-0.0015(4)	14.088(6)	0.6	9	6724		
	Broad	17.7(3)	0.477(7)	-0.033(5)	14.13(3)	1.9				
	Single	9.9(2)	0.104(1)	0.0005(5)	13.94(1)	0.4			10.2(4)	0.116(7)
Oph-D	Narrow	9.7(3)	0.088(1)	-0.006(1)	13.89(2)	0.3	22, 21	383		
	Broad	12.0(1)	0.39(2)	0.14(2)	13.8(1)	1.8				
	Single	12.5(4)	0.168(4)	0.000(2)	13.77(4)	0.7			12.3(5)	0.171(8)
Oph-E	Narrow	11.7(3)	0.126(2)	0.023(2)	13.73(3)	0.5	24	3698		
	Broad	17.9(6)	0.76(2)	-0.92(3)	– [g]	3.0				
	Single	13.9(1)	0.174(2)	0.0003(5)	13.91(1)	0.7			14.9(8)	0.19(1)
Oph-F	Narrow	12.6(1)	0.128(1)	0.006(1)	13.81(1)	0.5	9, 11	5244		
	Broad	19.1(4)	0.55(1)	-0.144(9)	13.87(7)	2.1				
	Single	11.6(1)	0.15(1)	0.0008(5)	14.0(9)	0.6			12.4(4)	0.16(1)
Oph-	Narrow	11.0(1)	0.133(1)	0.012(1)	13.971(9)	0.6	16	1489		
H-MM1	Broad	16.9(7)	0.47(2)	-0.4(3)	13.99(8)	1.9				
	Single	12.1(2)	0.137(2)	0.005(1)	13.79(2)	0.6			12.2(2)	0.160(8)
L1688-d10	Narrow	11.2(2)	0.111(2)	0.015(2)	13.76(2)	0.4	14	826		
	Broad	17.1(8)	0.42(2)	-0.2(2)	13.6(2)	1.7				
	Single	10.6(2)	0.135(1)	-0.0004(4)	13.92(1)	0.6			10.4(1)	0.129(6)
L1688-d12	Narrow	9.4(6)	0.123(4)	-0.0009(7)	13.91(3)	0.6	16	30		
	Broad	18.0(3)	0.26(5)	0.0(1)	13.6(4)	1.0				

Table A.1: (continued)

Core	Component [a]	T_K (K)	σ_v [b] (km s^{-1})	v_{rel} [c] (km s^{-1})	log(N(p-NH_3) /(cm^{-2})	$\mathcal{M}_s$	noise[d] (mK)	Δ_{AIC} [e]	$T_{K,GAS}$ (K)	$\sigma_{v,GAS}$ (km s^{-1})
	Single	12.4(3)	0.149(3)	-0.002(2)	13.81(3)	0.6			12.5(5)	0.14(1)
Oph-B3	Narrow	11.4(3)	0.117(2)	-0.028(2)	13.67(3)	0.5	26, 28	1083		
	Broad	19.0(1)	0.58(3)	0.56(4)	13.8(2)	2.2				
	Single	13.5(4)	0.209(6)	0.000(1)	13.75(5)	0.9			14.2(5)	0.18(2)
L1688-SR1	Narrow	10(1)	0.102(5)	-0.033(4)	13.3(1)	0.4	35	308		
	Broad	18.0(1)	0.43(2)	0.11(2)	13.7(2)	1.7				
	Single	17.2(3)	0.239(4)	0.000(2)	13.35(8)	0.9			16.70(6)	0.222(3)
L1688-SR2	Narrow	15.4(5)	0.178(6)	-0.009(4)	13.2(1)	0.7	11	164		
	Broad	24.0(2)	0.6(5)	0.08(3)	13.0(4)	2.0				
	Single	24.6(6)	0.295(8)	0.0[f]	– [g]	0.9			– [h]	– [h]
L1688-SR3	Narrow	24(1)	0.24(2)	0.05(2)	– [g]	0.8	18	12		
	Broad	27.0(5)	0.41(7)	-0.2(2)	– [g]	1.3				
	Single	16.9(2)	0.451(4)	0.0002(0)	13.79(2)	1.8			– [h]	– [h]
Ambient	Broad-1	16.9(2)	0.35(2)	-0.16(4)	13.74(3)	1.4	9	94		
cloud [i]	Broad-2	17.0(5)	0.35(3)	0.45(7)	13.2(3)	1.4				

Notes. Kinetic temperatures, velocity dispersions and p-NH_3 column densities, derived from single-component fits, and two-component fits, in the coherent cores and the ambient cloud [i]. The values in parentheses represent the fit-determined error in the final decimal place of the corresponding parameter. These uncertainties do not include the calibration uncertainty, which is ∼10 %. The noise level achieved in the average spectra are also shown. The final two columns show the average kinetic temperature and velocity dispersions inside the cores, from GAS DR1 (Friesen et al. 2017) results (single-component fit).

(a) single-component fit, or the individual components of the two-component fit.

(b) The channel response, σ_{chan} (see Section 2.4.2), is not removed from the σ_v value reported here (The contribution from σ_{chan} is very small, changes only in the third decimal place in σ_v).

(c) Velocity from the fit. Since we align the spectrum in the core by the velocity at each pixel (determined from single-component fit), the velocities reported in this Table are relative to the mean velocity in the corresponding core.

(d) Noise level estimated for both NH_3 (1,1) and (2,2). In cases where two values are reported, the noise in NH_3 (1,1) and (2,2) are not the same, and the values correspond to the noise in (1,1) and (2,2), respectively.
(e) Change in AIC, from 1-component fit to 2-component fit ($\Delta_{AIC} = AIC_{1-comp.} - AIC_{2-comp.}$).
(f) Value and error smaller than 10^{-4} km s^{-1}.
(g) Excitation temperature could not be well-constrained from the fit (fit determined error > 30%), and therefore, the column density estimate is not very reliable.
(h) Velocity dispersion and temperature maps from GAS DR1 did not include any pixel inside SR3, or ambient cloud box.
(i) Represents the average spectra in the "ambient cloud box" shown in Figure 2.1.

Appendix B

Appendices for Chapter 3

B.1 Selection of cores, and shells

Figures B.1 and B.2 show the cores, with shell-1 and shell-2 around each of them, similar to Figure 3.8, but with kinetic temperature and sonic Mach number as the background colour-scale.

B.2 Averaged spectra in the cores, shell-1 and shell-2

Figures B.3 to B.14 shows the average spectra in the respective coherent cores, used in Section 3.6.2. The final model determined by the fit is overlaid (in green) on the spectra.

Figure B.15 shows an alternate two-component fit to shell-2 of H-MM1. Here, we have restricted the relative positions of the narrow and the broad components, so that the narrow component is always at a higher velocity than the broad component (Section 3.6.5).

B.3 Fit parameters for average spectra

In Table B.1, we present the kinetic temperature, velocity dispersion and p-NH_3 column densities for the cores and shells-1 and -2, from one-component fits and two-component fits to the average spectra in the respective regions. We also show the improvement in the fit (as change in AIC value) from one- to two-component fit, and the noise level, for each spectrum.

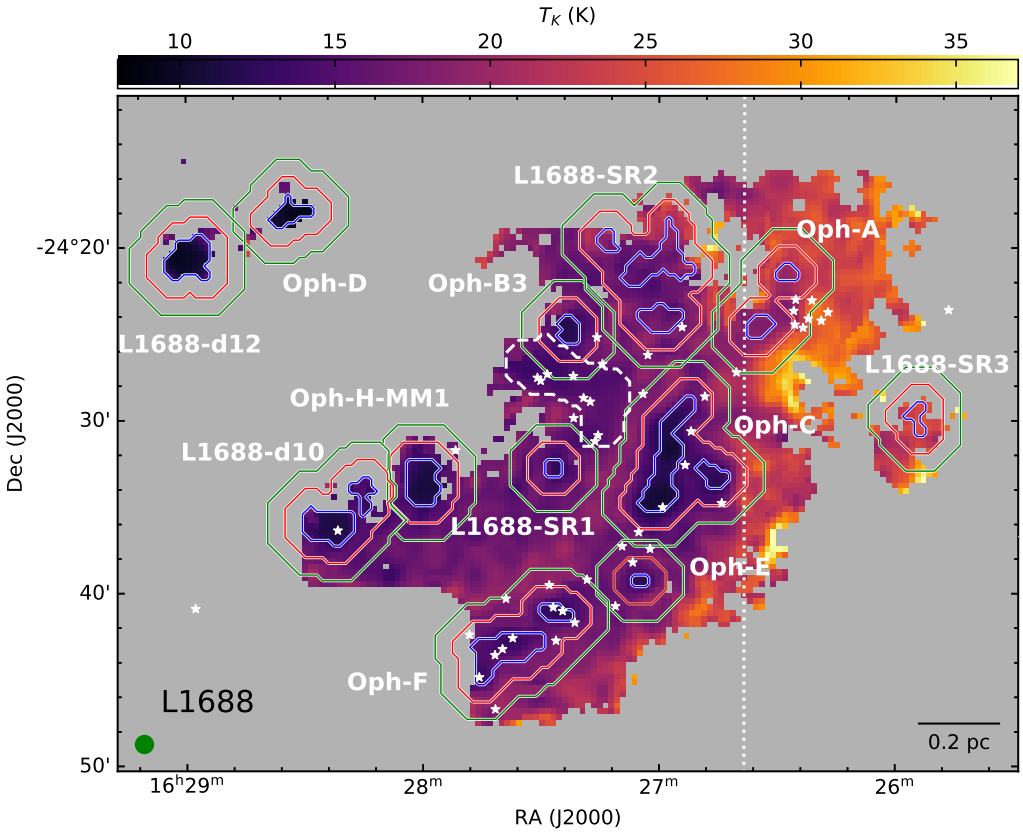

Figure B.1: Coherent cores and shells-1 and -2, as defined in Section 3.5.4, are shown on the kinetic temperature map, with blue, red and green contours, respectively. The white stars show the positions of Class 0/I and flat-spectrum protostars in the cloud. The white dashed contour shows a rough boundary for Oph-B1 and Oph-B2 (see Section 3.5.4). The white dotted line roughly separates the dark cloud to the left from the molecular material affected by the external illumination to the right.

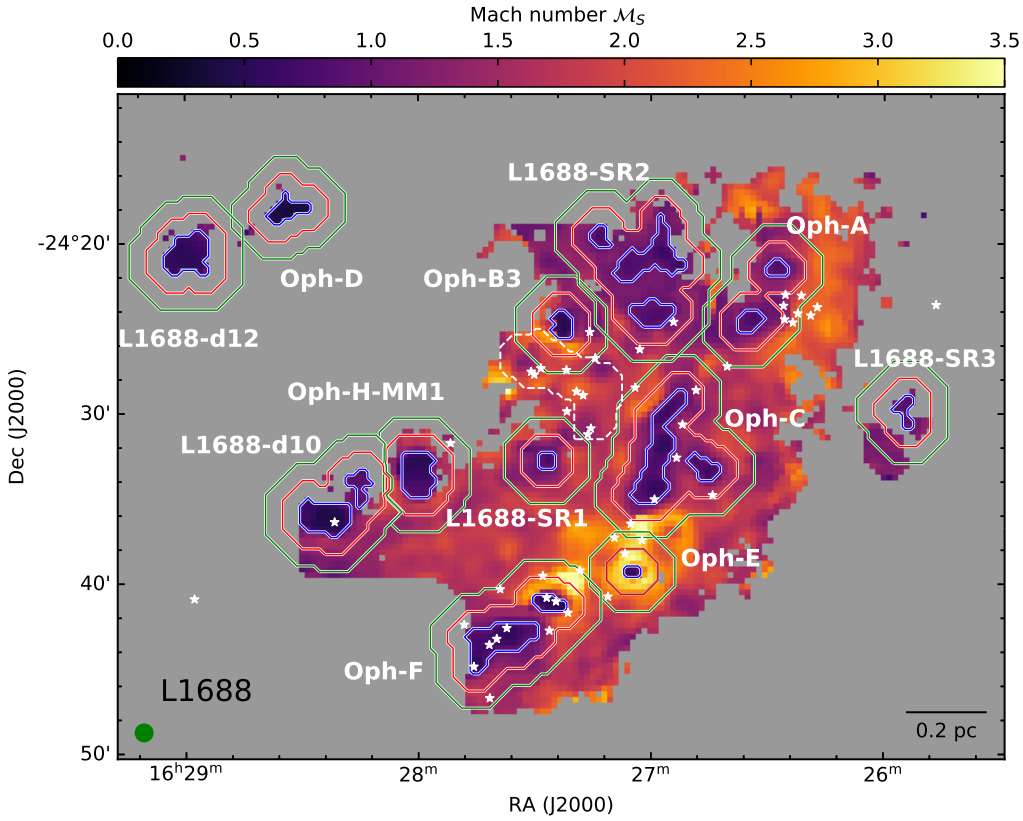

Figure B.2: Similar to Figure B.1, but with sonic Mach number as the background colour map.

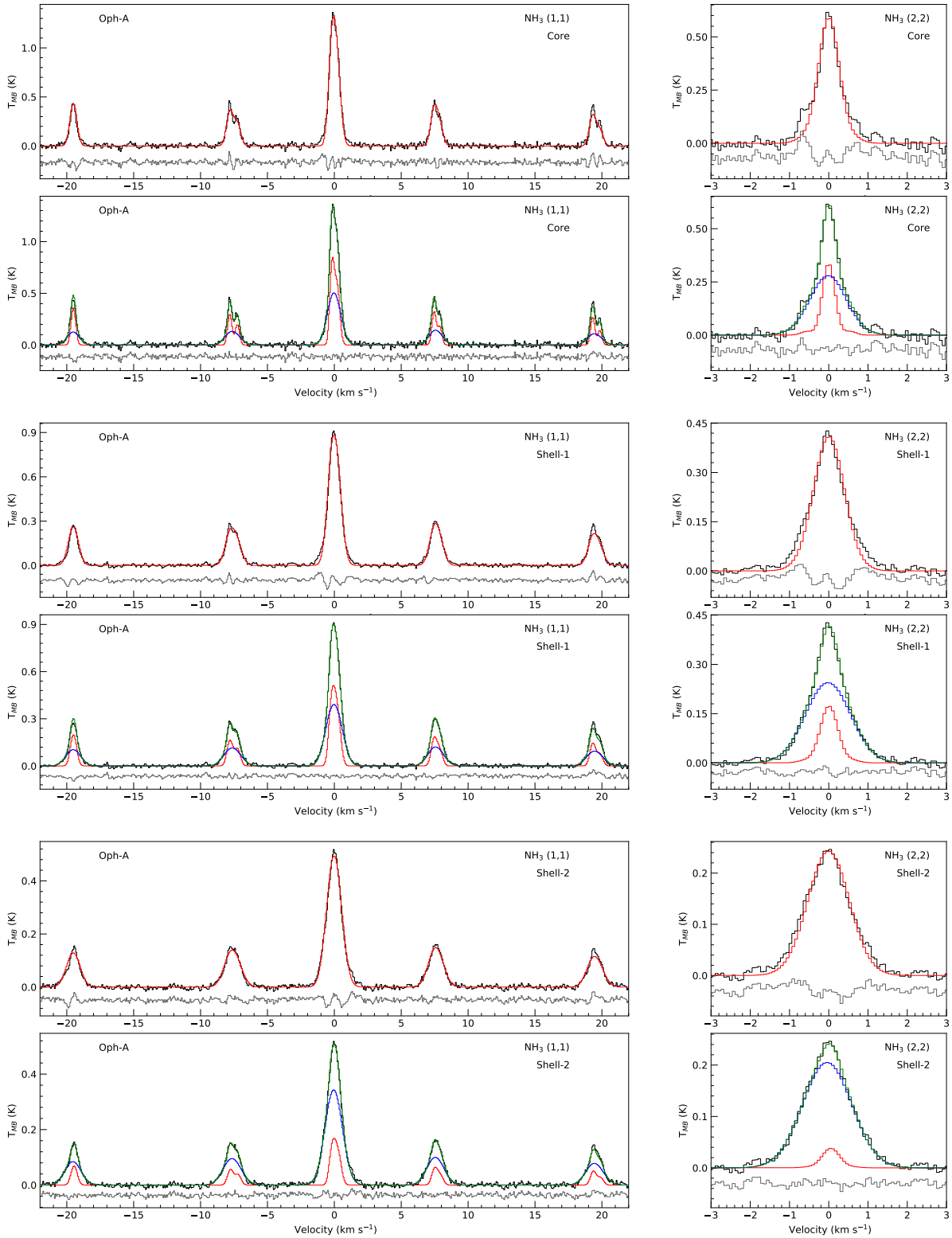

Figure B.3: Top panels: Average NH_3 (1,1) and (2,2) spectra of Oph-A core, shell-1 and shell-2 with a one-component fit. Bottom panels: Same spectra, but with a two-component fit (green). The narrow (red) and broad (blue) components are also shown separately.

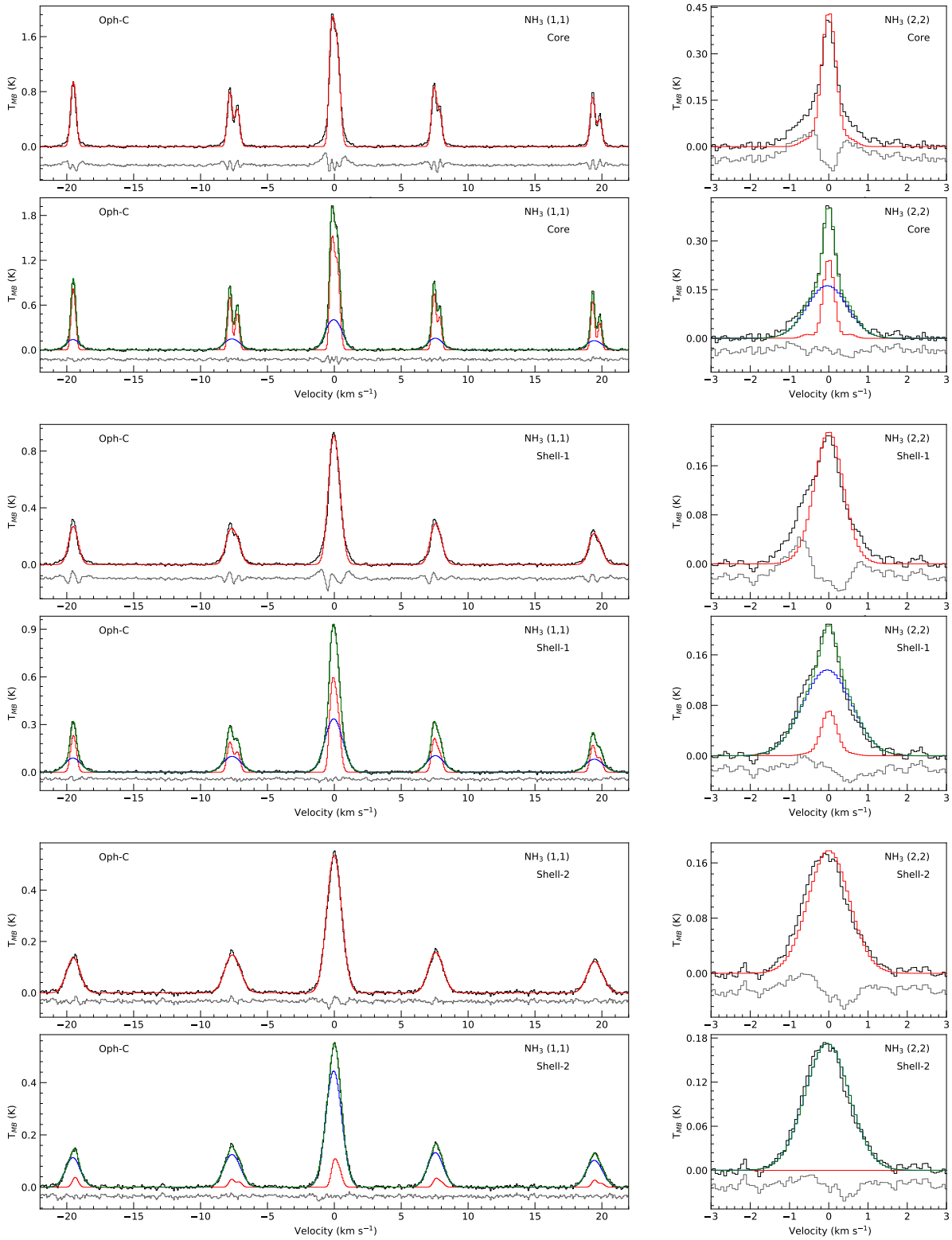

Figure B.4: Same as Figure B.3, but for Oph-C

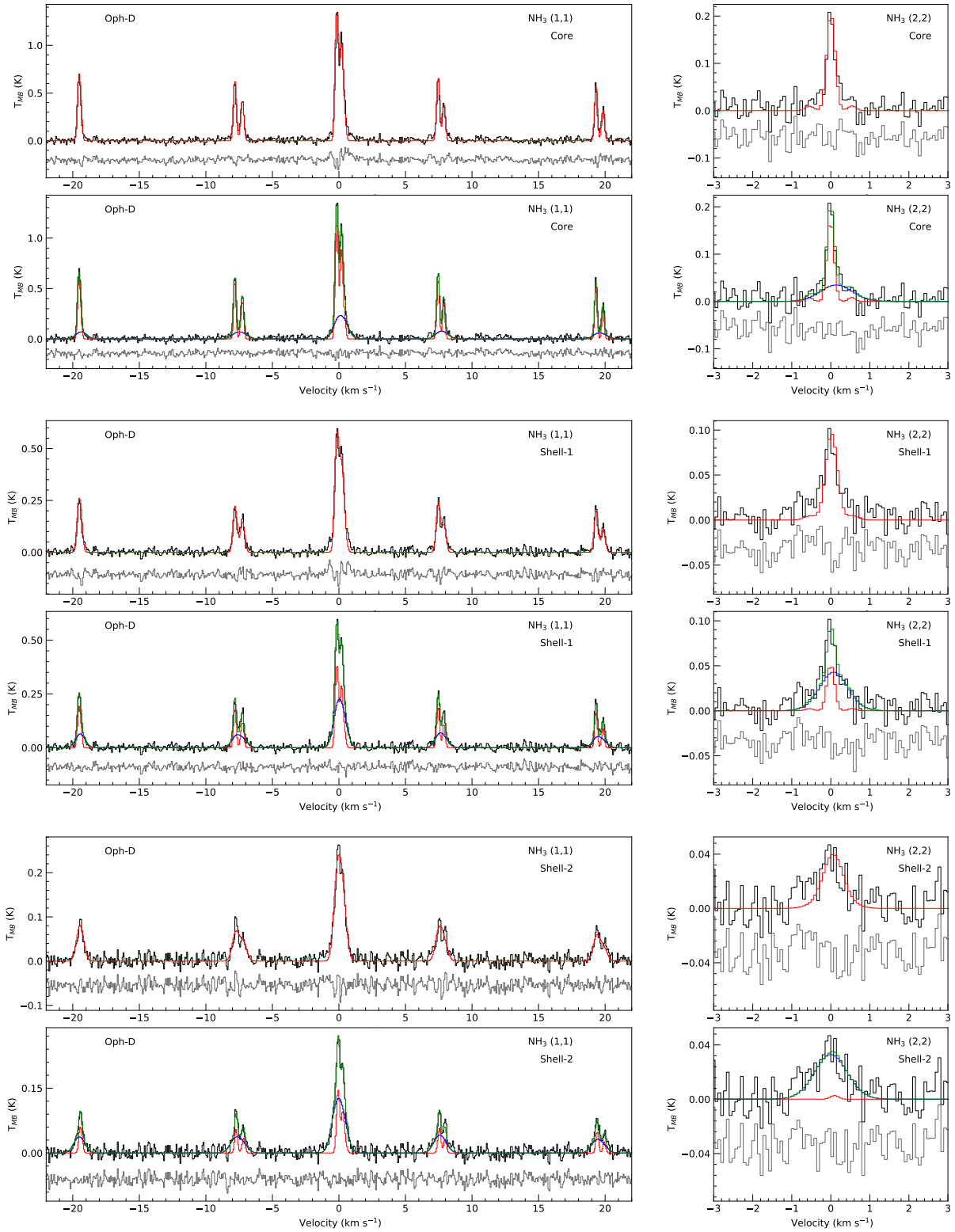

Figure B.5: Same as Figure B.3, but for Oph-D

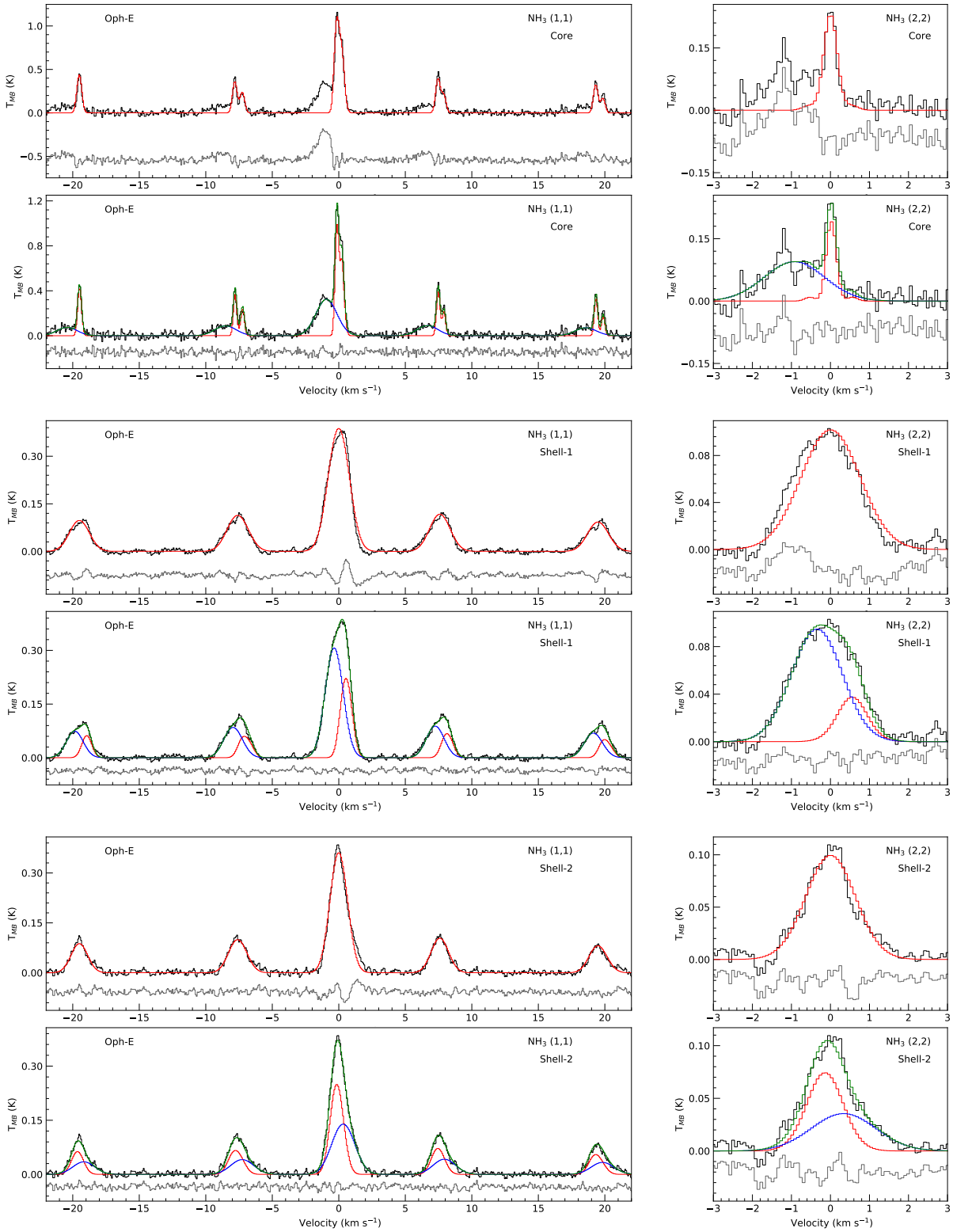

Figure B.6: Same as Figure B.3, but for Oph-E

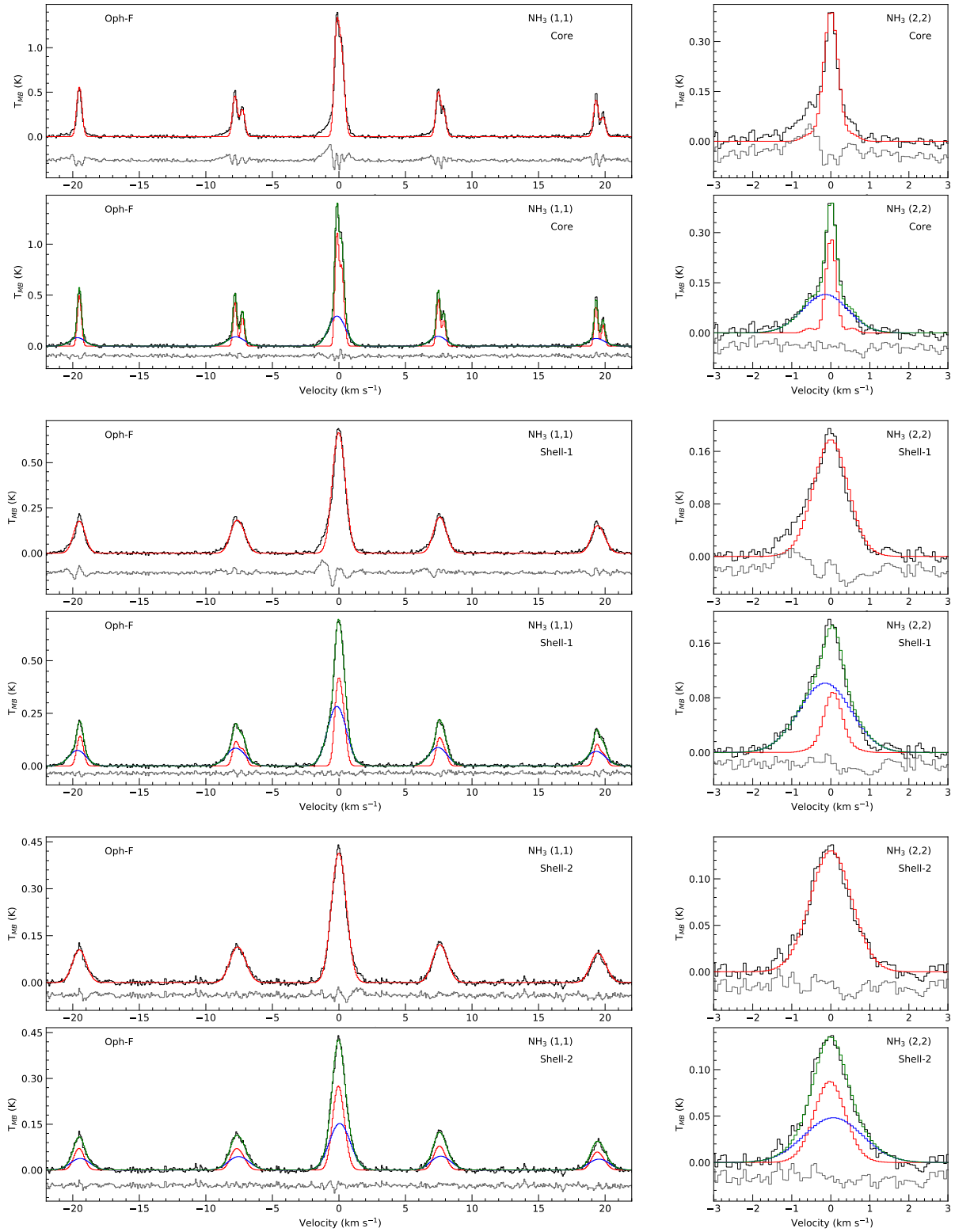

Figure B.7: Same as Figure B.3, but for Oph-F

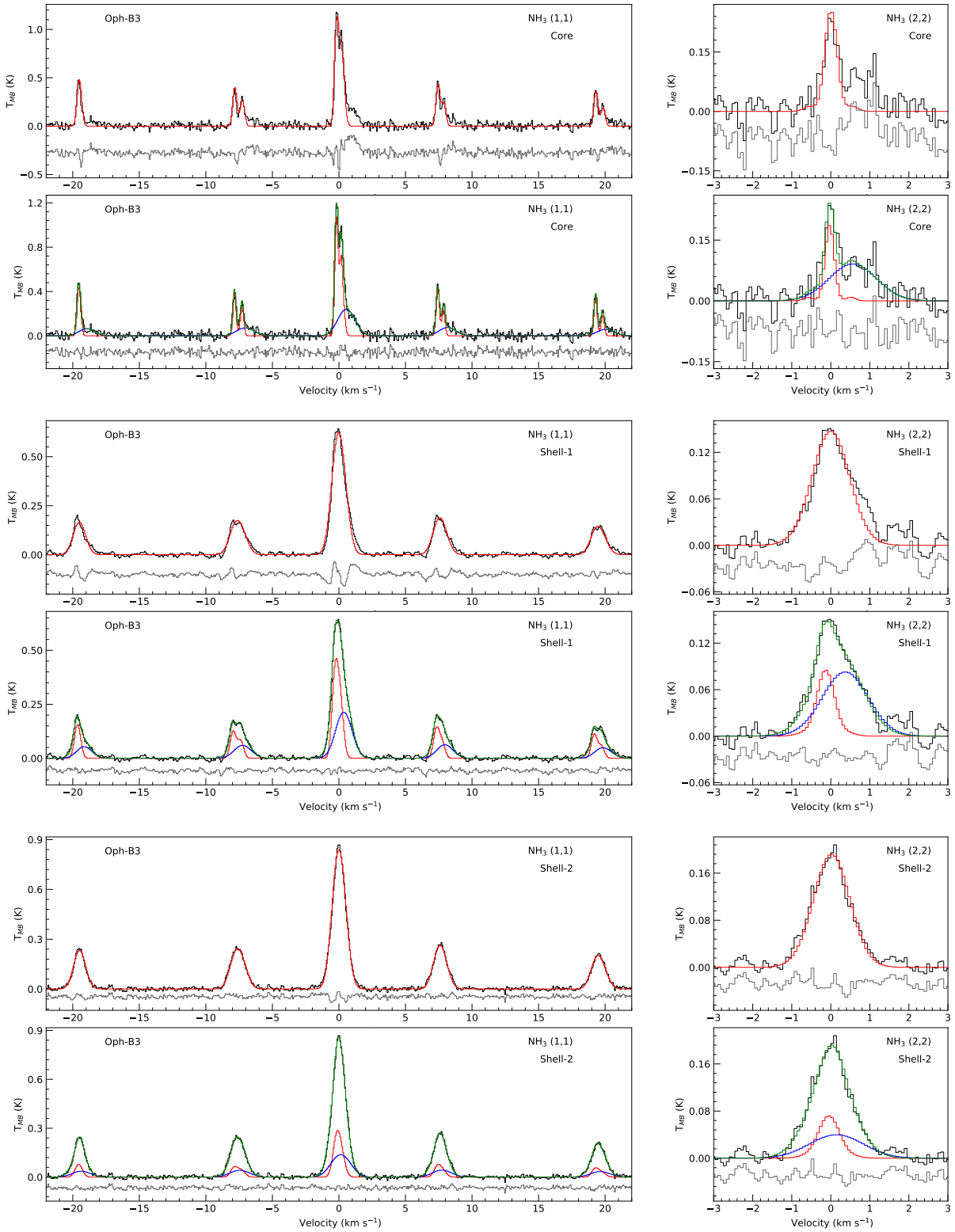

Figure B.8: Same as Figure B.3, but for Oph-B3

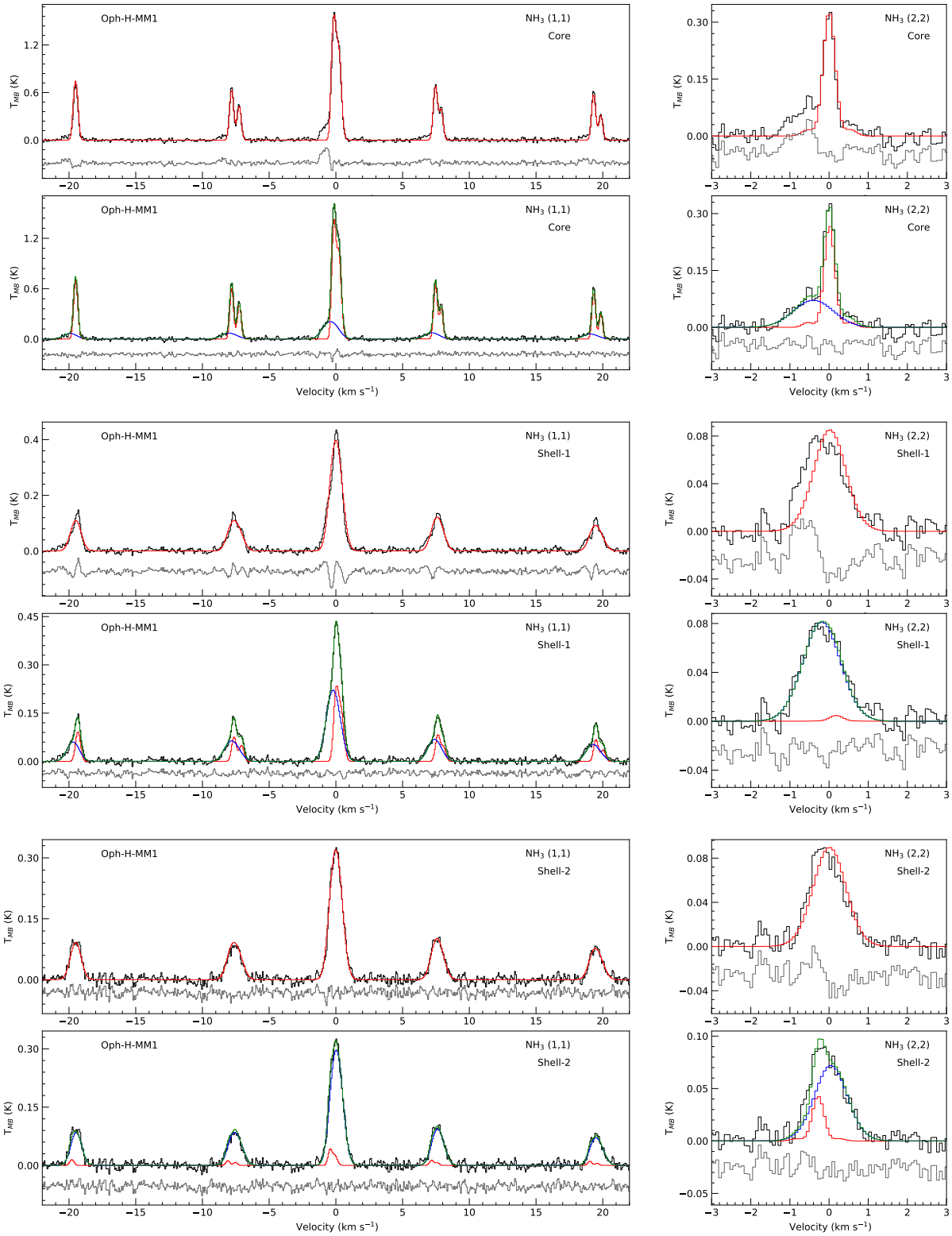

Figure B.9: Same as Figure B.3, but for Oph-H-MM1

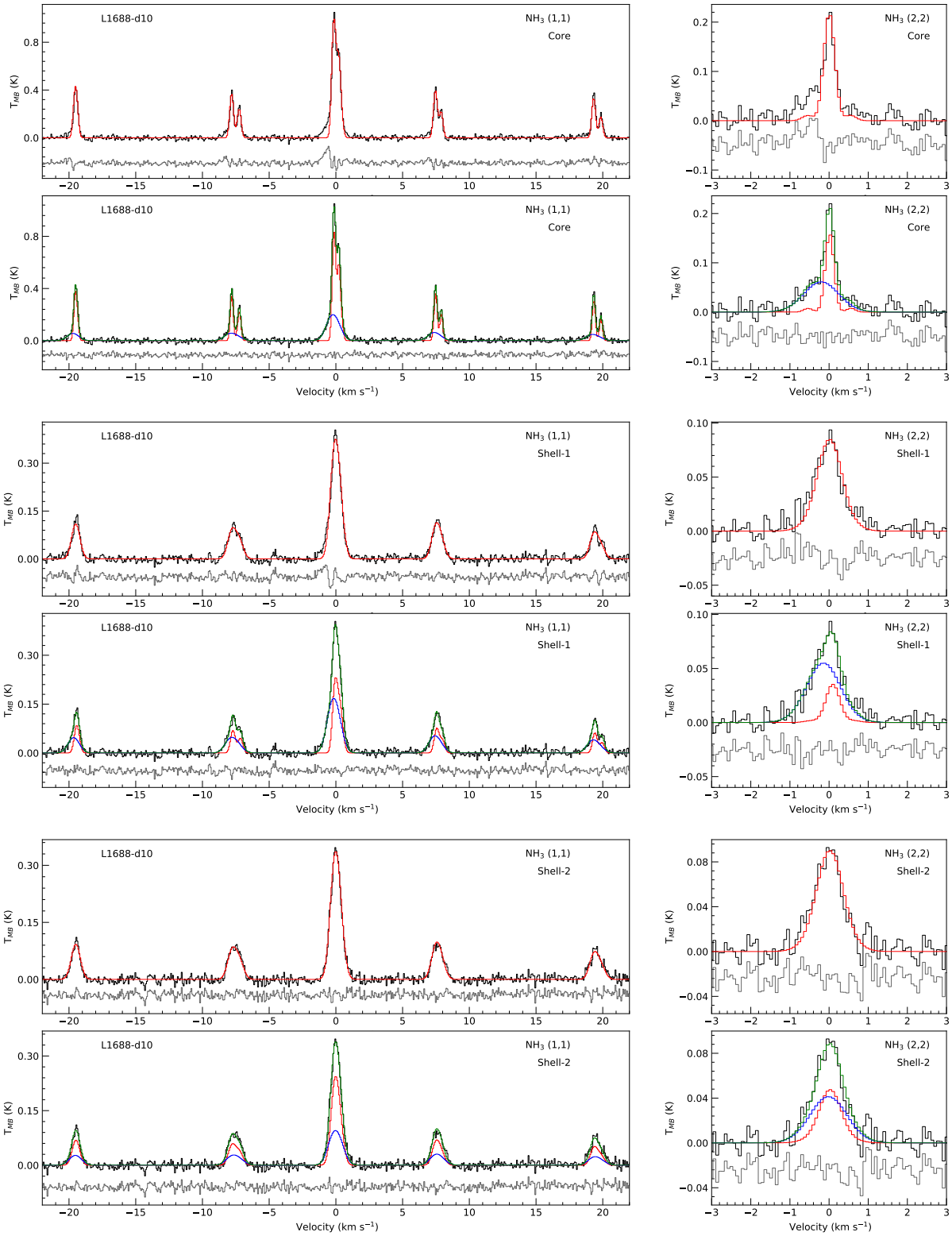

Figure B.10: Same as Figure B.3, but for L1688-d10

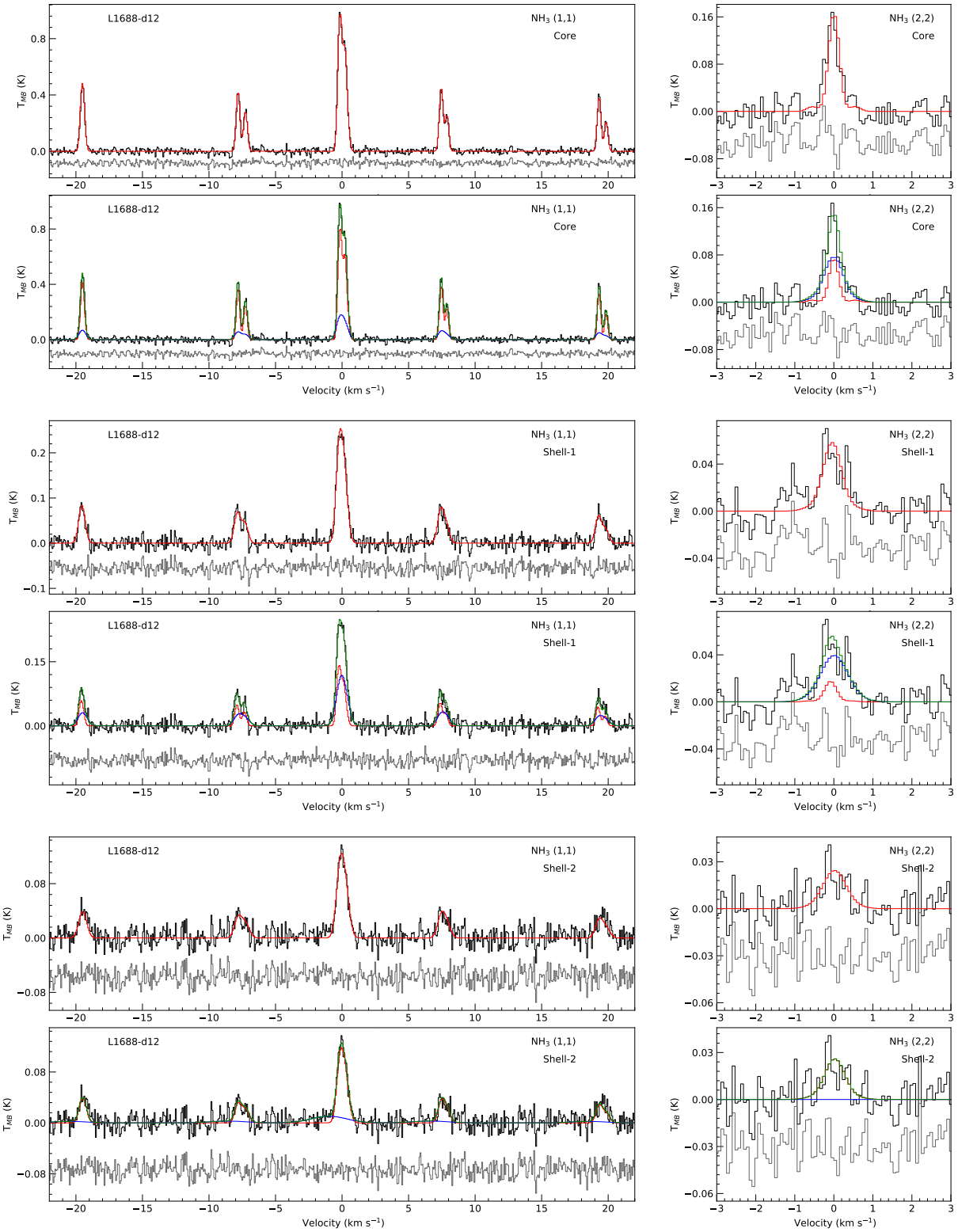

Figure B.11: Same as Figure B.3, but for L1688-d12

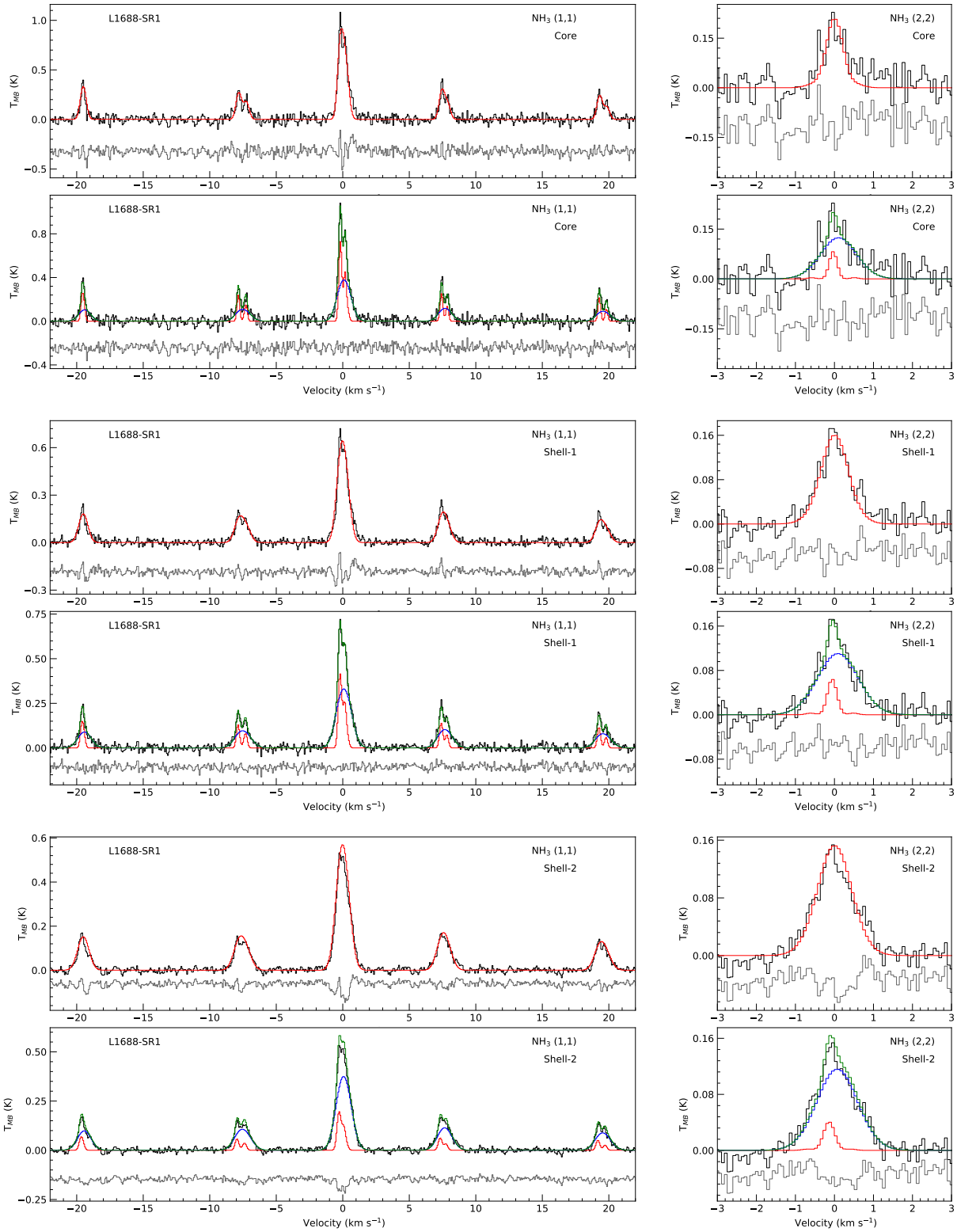

Figure B.12: Same as Figure B.3, but for L1688-SR1

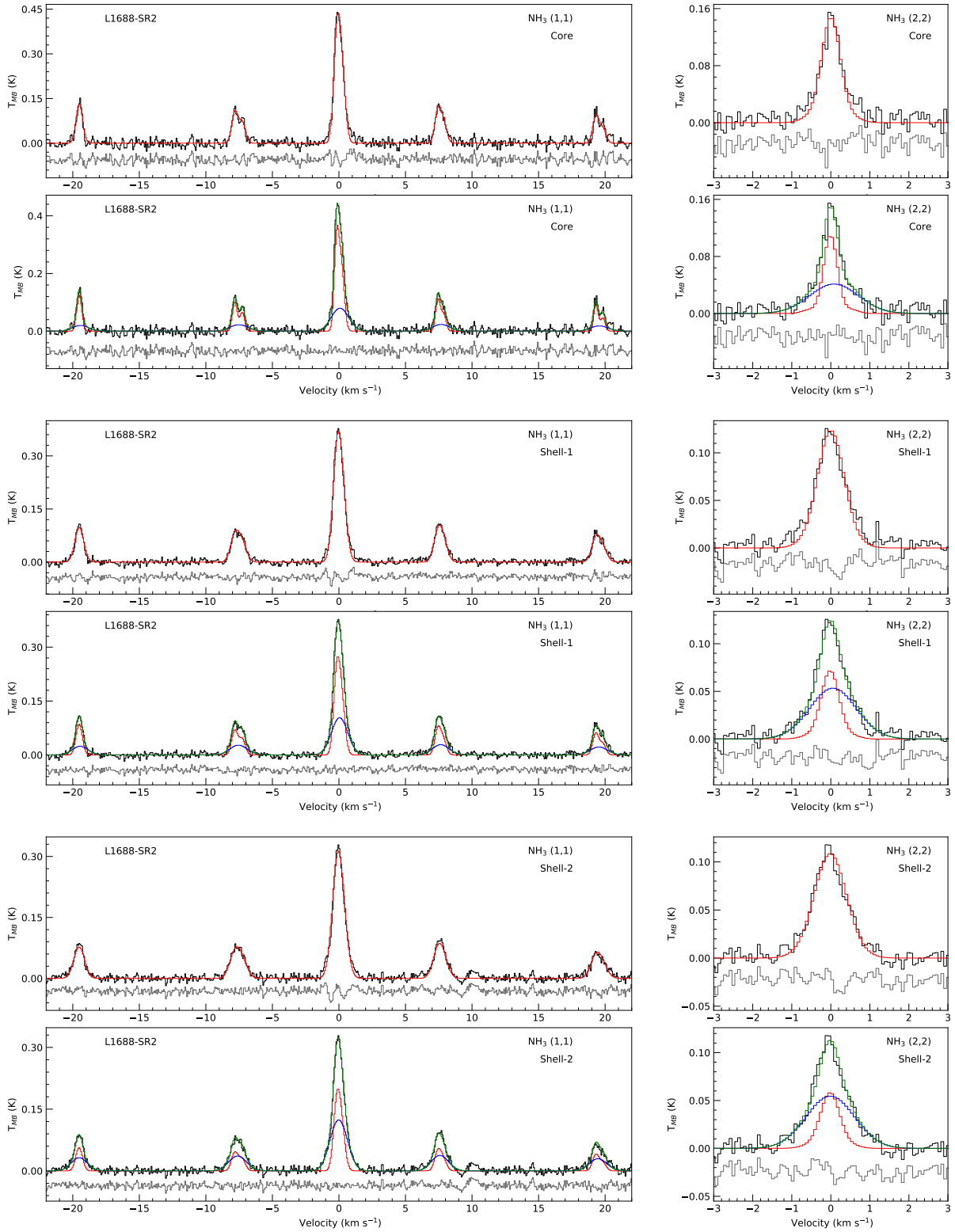

Figure B.13: Same as Figure B.3, but for L1688-SR2

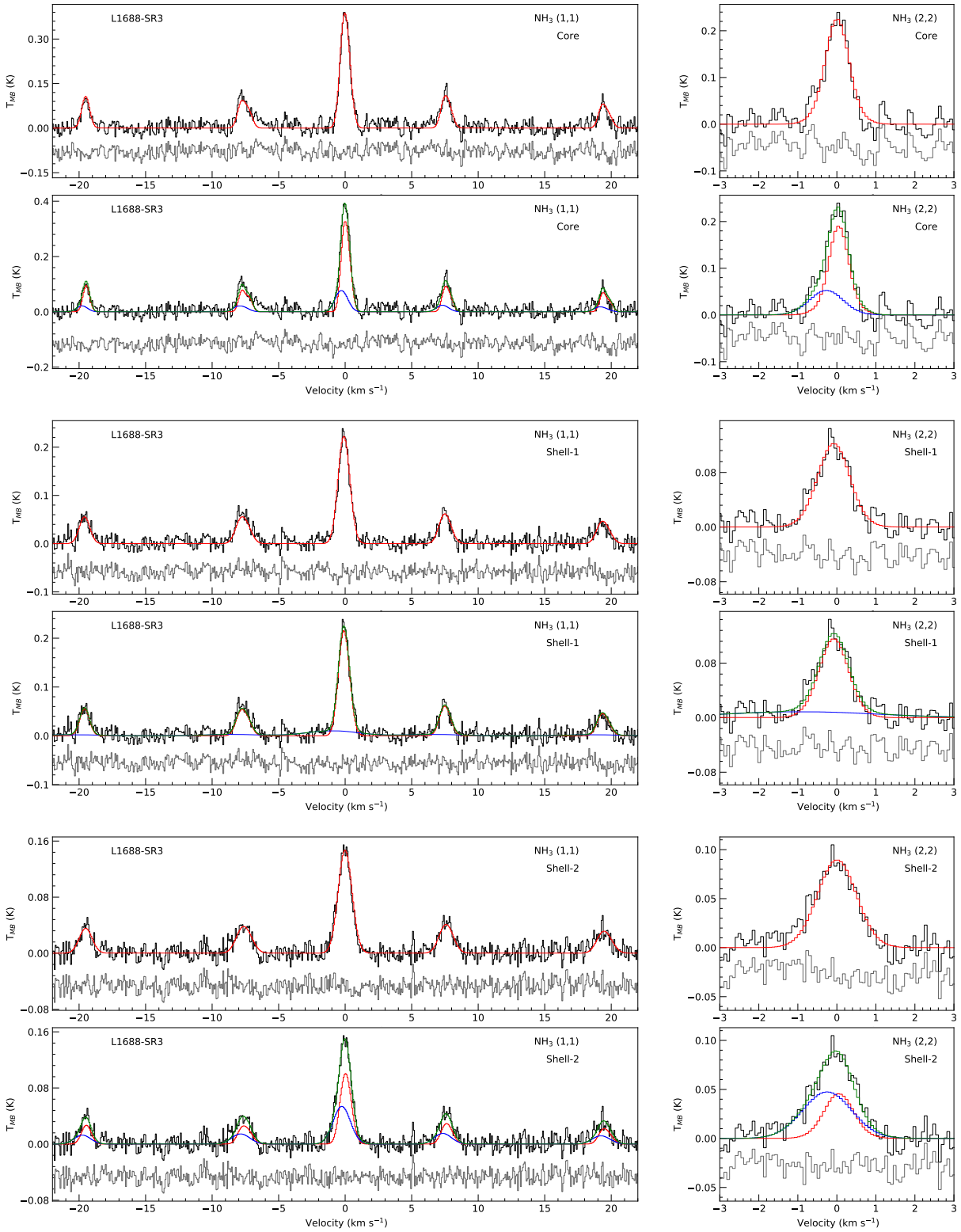

Figure B.14: Same as Figure B.3, but for L1688-SR3

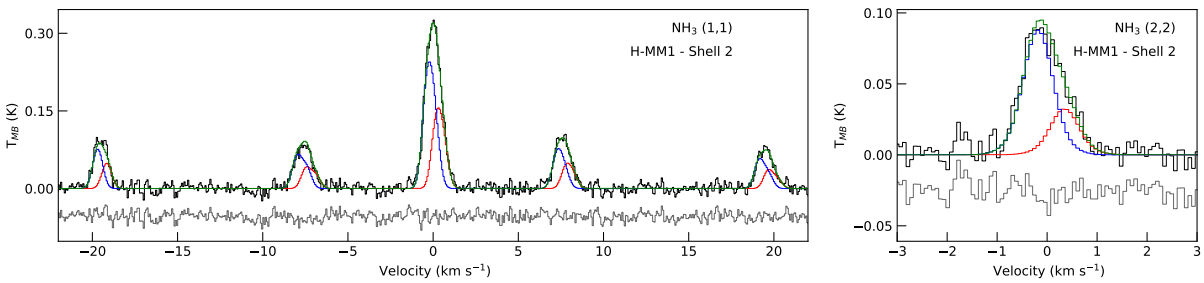

Figure B.15: Alternate two-component fit to the average spectra in shell-2 of H-MM1 (see Section 3.6.5).

Table B.1: Best-fit parameters for one- and two-component fits in cores and shells.

	Component [a]	$T_{\rm K}$ (K)	$\log_{10}(N(p-{\rm NH_3})/{\rm cm^{-2}})$	$\sigma_{\rm v}$ [b] (km s^{-1})	$v_{\rm rel}$ [c] (km s^{-1})	$\mathcal{M}_S$	noise [d] (mK)	Δ_{AIC}
Oph-A : core	Single	19.1(2)	13.86(2)	0.253(3)	0.0 [f]	0.9	17	761
	Narrow	15.8(4)	13.74(4)	0.156(4)	-0.001(2)	0.6		
	Broad	24.9(8)	– [e]	0.44(1)	-0.014(6)	1.5		
Oph-A : shell-1	Single	20.7(1)	13.88(1)	0.366(2)	0.001(2)	1.3	8, 7	1404
	Narrow	15.3(3)	13.81(3)	0.213(5)	0.009(3)	0.8		
	Broad	26.7(5)	13.8(7)	0.54(1)	-0.019(5)	1.7		
Oph-A : shell-2	Single	22.7(2)	13.72(3)	0.5(3)	-0.008(3)	1.7	6	671
	Narrow	12.8(6)	– [e]	0.214(8)	0.054(6)	0.9		
	Broad	26.6(4)	13.6(7)	0.598(8)	-0.042(5)	1.9		
Oph-C : core	Single	11.72(9)	14.168(5)	0.177(1)	0.0 [f]	0.8	9	6724
	Narrow	10.13(9)	14.088(6)	0.1376(8)	-0.0015(4)	0.6		
	Broad	17.7(3)	14.13(3)	0.477(7)	-0.033(5)	1.9		
Oph-C : shell-1	Single	14.9(1)	13.81(1)	0.346(2)	0.0(9)	1.5	5	5664
	Narrow	10.7(2)	13.74(2)	0.195(2)	0.008(2)	0.9		
	Broad	20.1(2)	13.79(5)	0.59(7)	-0.038(4)	2.2		
Oph-C : shell-2	Single	18.5(1)	13.63(2)	0.501(2)	-0.003(2)	1.9	5	427
	Narrow	– [g]	13.4(2)	0.2(1)	0.139(9)	– [g]		
	Broad	20.0(2)	13.66(4)	0.538(4)	-0.04(4)	2.0		
Oph-D : core	Single	9.9(2)	13.94(1)	0.104(1)	0.0005(5)	0.4	22, 21	383
	Narrow	9.7(3)	13.89(2)	0.088(1)	-0.006(1)	0.3		
	Broad	12.0(1)	13.8(1)	0.39(2)	0.14(2)	1.8		
Oph-D : shell-1	Single	11.0(3)	13.8(2)	0.148(2)	0.016(3)	0.7	13	351
	Narrow	9.6(6)	13.77(4)	0.098(4)	-0.001(2)	0.4		
	Broad	13.9(8)	13.5(2)	0.34(2)	0.07(1)	1.5		

Table B.1: (continued)

	Component [a]	$T_{\rm K}$ (K)	$\log_{10}(N(p-{\rm NH_3})/{\rm cm^{-2}})$	$\sigma_{\rm v}$ [b] (km s^{-1})	$v_{\rm rel}$ [c] (km s^{-1})	$\mathcal{M}_S$	noise [d] (mK)	Δ_{AIC}
Oph-D : shell-2	Single	12.4(5)	13.62(7)	0.255(8)	0.058(6)	1.2	11	123
	Narrow	7.0(4)	– [e]	0.104(6)	0.091(6)	0.6		
	Broad	15.0(1)	13.7(1)	0.39(2)	0.0(3)	1.6		
Oph-E : core	Single	12.5(4)	13.77(4)	0.168(4)	0.002(4)	0.7	24	3698
	Narrow	11.7(3)	13.73(3)	0.126(2)	0.023(2)	0.5		
	Broad	17.9(6)	– [e]	0.76(2)	-0.92(3)	3.0		
Oph-E : shell-1	Single	16.5(1)	13.79(3)	0.735(5)	0.0(1)	3.0	5, 6	1574
	Narrow	13.4(5)	13.48(6)	0.36(1)	0.56(1)	1.6		
	Broad	18.1(2)	13.49(7)	0.63(2)	-0.34(4)	2.5		
Oph-E : shell-2	Single	17.1(2)	13.52(7)	0.615(5)	0.0(9)	2.5	6	634
	Narrow	17.5(4)	13.3(1)	0.45(2)	-0.14(1)	1.8		
	Broad	16.3(6)	13.7(1)	0.8(2)	0.34(5)	3.3		
Oph-F : core	Single	13.9(1)	13.91(1)	0.174(2)	-0.0003(5)	0.7	9, 11	5244
	Narrow	12.6(1)	13.81(1)	0.128(1)	0.006(1)	0.5		
	Broad	19.1(4)	13.87(7)	0.55(1)	-0.144(9)	2.1		
Oph-F : shell-1	Single	16.3(1)	13.67(3)	0.423(3)	-0.004(3)	1.7	5, 6	3536
	Narrow	13.5(2)	13.59(3)	0.23(4)	0.058(3)	1.0		
	Broad	18.8(3)	13.79(5)	0.638(8)	-0.148(7)	2.5		
Oph-F : shell-2	Single	18.0(1)	13.57(4)	0.507(3)	0.002(4)	2.0	6	220
	Narrow	18.0(5)	– [e]	0.38(2)	-0.025(6)	1.5		
	Broad	18.1(7)	13.6(2)	0.72(3)	0.06(2)	2.9		
Oph-H-MM1 : core	Single	11.6(1)	14.0(9)	0.15(1)	0.0008(5)	0.6	16	1489
	Narrow	11.0(1)	13.971(9)	0.12(1)	0.012(1)	0.6		
	Broad	16.9(7)	13.99(8)	0.47(2)	-0.4(3)	1.9		
Oph-H-MM1 : shell-1	Single	14.7(2)	13.6(5)	0.387(5)	0.015(4)	1.7	6, 7	1513
	Narrow	7.0(1)	13.54(5)	0.171(5)	0.182(5)	1.0		
	Broad	18.8(4)	13.65(7)	0.451(8)	-0.19(1)	1.7		

Table B.1: (continued)

	Component [a]	T_K (K)	$\log_{10}(N(p-NH_3)/cm^{-2})$	σ_v [b] (km s^{-1})	v_{rel} [c] (km s^{-1})	$\mathcal{M}_S$	noise [d] (mK)	Δ_{AIC}
Oph-H-MM1 : shell-2	Single	16.2(2)	13.68(4)	0.391(5)	0.007(4)	1.6	9	41
	Narrow	30.0(6)	– [e]	0.15(2)	-0.28(2)	0.3		
	Broad	15.2(3)	13.66(5)	0.392(6)	0.05(1)	1.7		
L1688-d10 : core	Single	12.1(2)	13.79(2)	0.137(2)	0.005(1)	0.6	14	826
	Narrow	11.2(2)	13.76(2)	0.111(2)	0.015(2)	0.4		
	Broad	17.1(8)	13.6(2)	0.42(2)	-0.2(2)	1.7		
L1688-d10 : shell-1	Single	14.7(2)	13.51(5)	0.304(5)	0.011(4)	1.3	8	303
	Narrow	11.7(7)	13.4(1)	0.177(8)	0.097(7)	0.8		
	Broad	17.6(7)	13.6(1)	0.41(1)	-0.14(2)	1.6		
L1688-d10 : shell-2	Single	16.2(2)	13.39(7)	0.328(5)	0.017(4)	1.3	9, 8	4
	Narrow	14.0(1)	– [e]	0.28(2)	0.03(1)	1.2		
	Broad	20.0(3)	– [e]	0.44(6)	-0.02(3)	1.6		
L1688-d12 : core	Single	10.6(2)	13.92(1)	0.135(1)	-0.0004(4)	0.6	16	30
	Narrow	9.4(8)	13.91(3)	0.123(4)	-0.0009(7)	0.6		
	Broad	18.0(3)	13.6(4)	0.26(5)	0.0(1)	1		
L1688-d12 : shell-1	Single	14.1(5)	13.49(9)	0.231(7)	-0.046(6)	1.0	11,12	23
	Narrow	10.0(2)	– [e]	0.15(1)	-0.08(1)	0.7		
	Broad	18.0(2)	– [e]	0.33(4)	0.01(3)	1.3		
L1688-d12 : shell-2	Single	13.6(9)	13.5(2)	0.29(2)	0.01(1)	1.3	12, 11	9
	Narrow[h]	–	–	–	–	–		
	Broad[h]	–	–	–	–	–		
Oph-B3 : core	Single	12.4(3)	13.81(3)	0.149(3)	-0.002(2)	0.6	26, 28	1083
	Narrow	11.4(3)	13.67(3)	0.117(2)	-0.028(2)	0.5		
	Broad	19.0(1)	13.8(2)	0.58(3)	0.56(4)	2.2		
Oph-B3 : shell-1	Single	15.6(2)	13.59(5)	0.379(5)	-0.012(4)	1.6	8, 9	1586
	Narrow	12.9(3)	13.54(4)	0.219(6)	-0.131(4)	1.0		
	Broad	20.1(6)	13.5(2)	0.56(2)	0.37(3)	2.1		

Table B.1: (continued)

	Component [a]	$T_{\rm K}$ (K)	$\log_{10}(N(p-{\rm NH_3})/{\rm cm^{-2}})$	$\sigma_{\rm v}$ [b] (km s^{-1})	$v_{\rm rel}$ [c] (km s^{-1})	$\mathcal{M}_S$	noise [d] (mK)	Δ_{AIC}
Oph-B3 : shell-2	Single	16.5(3)	– [e]	0.417(7)	-0.005(6)	1.7	8, 9	266
	Narrow	15.8(8)	– [e]	0.27(2)	-0.05(9)	1.1		
	Broad	17.0(1)	13.8(2)	0.66(4)	0.14(3)	2.7		
L1688-SR1 : core	Single	13.5(4)	13.75(5)	0.209(6)	0.000(1)	0.9	35	308
	Narrow	10(1)	13.3(1)	0.102(5)	-0.033(4)	0.4		
	Broad	18.0(1)	13.7(2)	0.43(2)	0.11(2)	1.7		
L1688-SR1 : shell-1	Single	15.5(3)	13.61(5)	0.334(6)	0.002(6)	1.4	16	582
	Narrow	11.6(7)	13.2(1)	0.121(4)	-0.058(4)	0.5		
	Broad	18.0(6)	13.7(1)	0.49(1)	0.09(1)	1.9		
L1688-SR1 : shell-2	Single	16.6(2)	13.6(5)	0.432(5)	0.002(7)	1.8	10, 12	373
	Narrow	13.1(9)	13.1(3)	0.142(8)	-0.136(7)	0.6		
	Broad	17.5(4)	13.67(7)	0.498(9)	0.072(8)	2.0		
L1688-SR2 : core	Single	17.2(3)	13.35(8)	0.239(4)	-0.000(2)	0.9	11	164
	Narrow	15.4(5)	13.3(1)	0.178(6)	-0.009(4)	0.7		
	Broad	24.0(2)	13.0(4)	0.6(5)	0.08(3)	2.0		
L1688-SR2 : shell-1	Single	18.2(2)	13.24(8)	0.328(4)	-0.002(2)	1.2	6, 7	251
	Narrow	15.2(5)	13.3(1)	0.228(8)	-0.018(4)	0.9		
	Broad	24.0(1)	– [e]	0.58(3)	0.05(2)	1.9		
L1688-SR2 : shell-2	Single	19.1(2)	– [e]	0.398(5)	-0.017(4)	1.5	6	219
	Narrow	16.6(7)	– [e]	0.25(1)	-0.02(6)	1.0		
	Broad	21.3(9)	13.6(2)	0.59(3)	-0.01(1)	2.1		
L1688-SR3 : core	Single	24.6(6)	– [e]	0.295(8)	0.0 [f]	0.9	18	12
	Narrow	24(1)	– [e]	0.24(2)	0.05(2)	0.8		
	Broad	27.0(5)	– [e]	0.41(7)	-0.2(2)	1.3		
L1688-SR3 : shell-1	Single	24.9(6)	– [e]	0.39(1)	-0.084(7)	1.3	9	54
	Narrow [h]	–	–	–	–	–		
	Broad [h]	–	–	–	–	–		

Table B.1: (continued)

	Component [a]	T_K (K)	$\log_{10}(N(p-NH_3)/cm^{-2})$	σ_v [b] (km s^{-1})	v_{rel} [c] (km s^{-1})	$\mathcal{M}_S$	noise [d] (mK)	Δ_{AIC}
L1688-SR3 : shell-2	Single	27.2(7)	– [e]	0.48(1)	0.0(0) [f]	1.5	9	40
	Narrow	21.0(3)	– [e]	0.36(6)	0.05(4)	1.3		
	Broad	38.0(8)	– [e]	0.61(6)	-0.2(1)	1.6		

Notes. Kinetic temperatures, p-NH_3 column densities, velocity dispersions, and velocities, derived from one-component and two-component fits in the coherent cores and the shells. The values in parentheses represent the fit-determined error in the final decimal place of the corresponding parameter. These uncertainties do not include the calibration uncertainty, which is ∼10 %. Also shown are the Mach numbers for each component, the rms noise in the averaged spectra, and the decrease in AIC parameter, from a one-component fit to two-component fit ($\Delta_{AIC} = AIC_{1-comp.} - AIC_{2-comp.}$).

(a) One-component fit, or the individual components of the two-component fit.
(b) The channel response, σ_{chan} (see Section 3.5.4), is not removed from the σ_v value reported here(The contribution from σ_{chan} is very small, changes only in the third decimal place in σ_v).
(c) Velocity from the fit. Since we align the spectrum in the core by the velocity at each pixel (determined from one-component fit), the velocities reported in this Table are relative to the mean velocity in the corresponding core or shell.
(d) Noise level estimated for both NH_3 (1,1) and (2,2). In cases where the noise in NH_3 (1,1) and (2,2) are not the equal, the noise in both the line are shown.
(e) Excitation temperature could not be well-constrained from the fit (fit determined error > 30%), and therefore, the column density estimate is not very reliable.
(f) Value and error smaller than 10^{-4} km s^{-1}.
(g) Kinetic temperature not could not be determined. See Section 3.6.5
(h) Two-component fit not reliable, see Section 3.6.5

Appendix C

Appendices for Chapter 4

C.1 Clustering method used in component assignment

As mentioned in Section 4.4.2, in the pixels with more than one component in the best fit model, we select the component that results in smooth maps of centroid velocity (v_{LSR}) and the brightness temperature (T_{MB}). In other words, our grouping is done to minimise sudden and sharp changes in these two parameters between nearby pixels. For this purpose, we define a weighted parameter distance, d_p, for two pixels as

$$d_p = \sqrt{(w_v \times \Delta v_{LSR})^2 + ((1 - w_v) \times \Delta T_{MB})^2}\,, \tag{C.1}$$

where $\Delta(v_{LSR})$ and $\Delta(T_{MB})$ are the differences in the two parameters at the two pixels, and w_v is the fractional weight ($0 < w_v < 1$) applied to $\Delta(v_{LSR})$. Starting with a pixel in the region with a one-component fit, we look at each of the neighbouring pixels and search for the component with lowest d_p. We group that component to the one-component map. We then move radially outward and repeat this process for the neighbours of each new pixel until the entire region is covered. Thus, we obtain the extended component, 'component 1'. We explore clustering with different relative weights in the parameters (w_v = 0.2-0.8) and different starting points but find that it has no significant change in the maps of component 1.

We then have one or two additional components in some pixels. Using different clustering methods as mentioned above, we are unable to get smooth parameter maps for these two components, which indicated the need of further subgroups. The additional components are then grouped according to their velocity, as described in Section 4.4.2.

C.2 Velocity dispersion maps

Figure C.1 shows the velocity dispersion in the four components identified in B5.

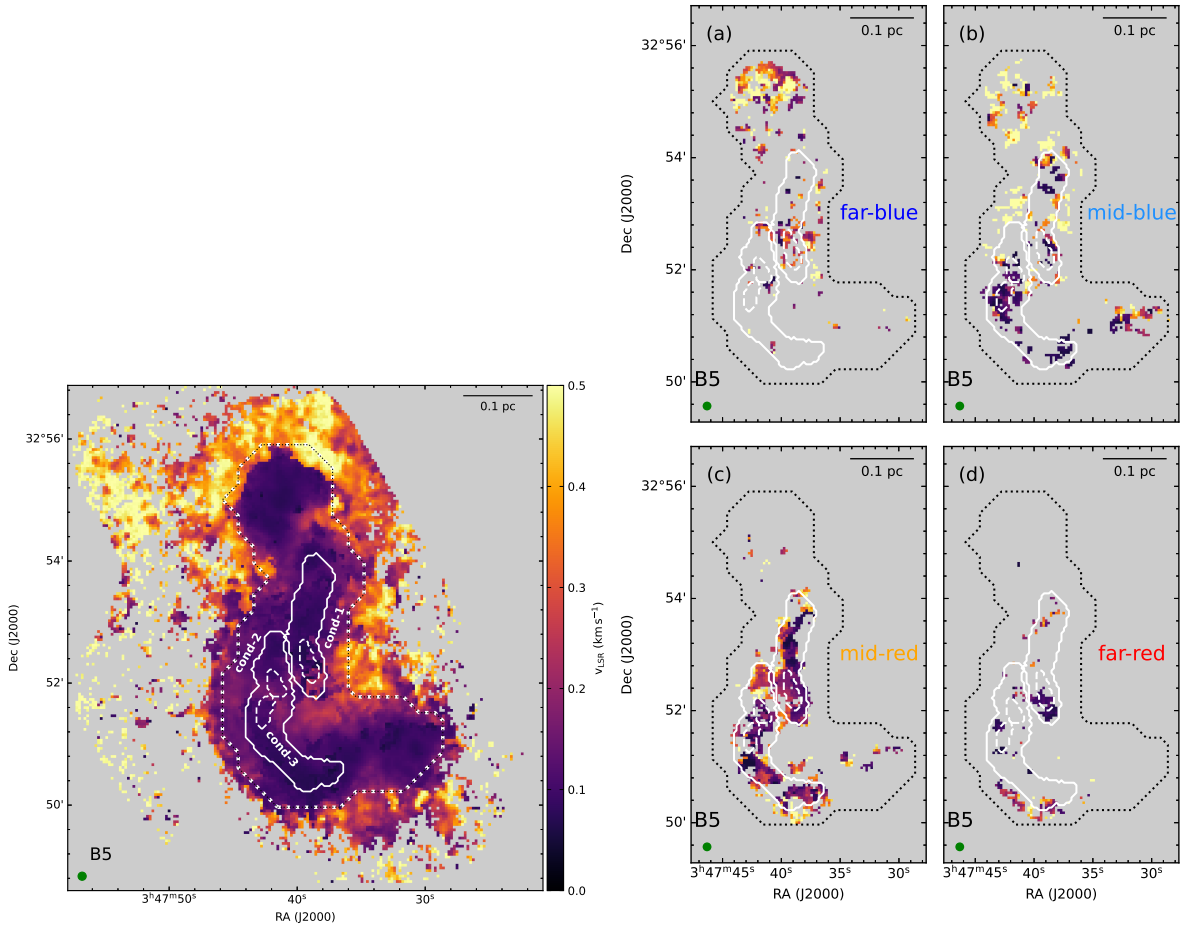

Figure C.1: *Left*: Velocity dispersion of the extended component. *Right*: Velocity dispersion of 4 additional components. The black-solid and black-dotted contours show the two filaments and the three condensations in B5, respectively. The white/black-dotted contours show the boundary of the coherent core in Pineda et al. (2010). The scale bar is shown in the top-right corner, and the beam is shown in the bottom-left corner.

C.3 Line-of-sight velocities along orthogonal cuts through major axes of the filaments

Figures C.2 and C.3 show the gradient in velocity across cuts orthogonal to the major axes of the the filaments 1 and 2, respectively. These cuts are spaced roughly one beam apart and are perpendicular to the filament spine at that location.

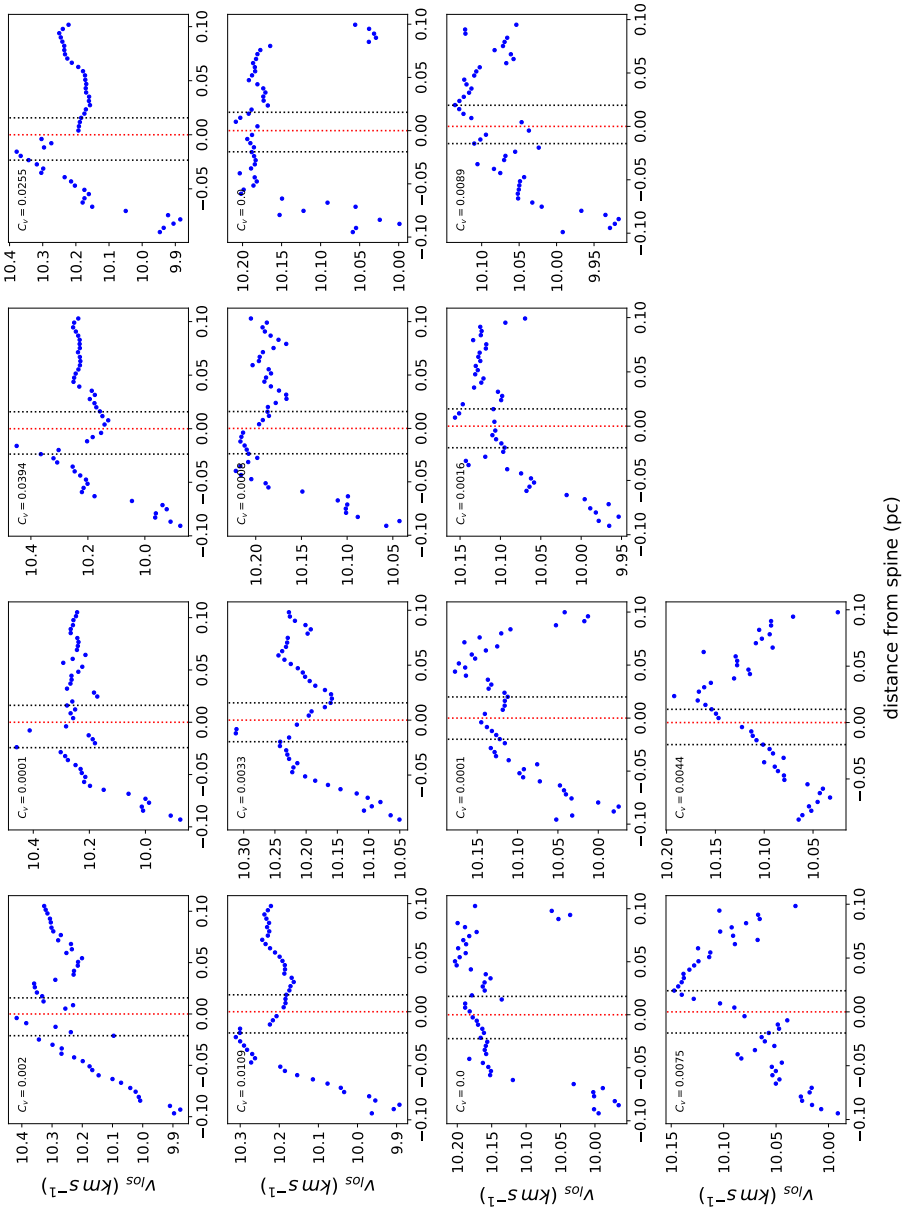

Figure C.2: The line-of-sight velocity profiles in the orthogonal cuts in Filament-1. The red-dotted vertical lines show the position of filament spine and the black-dotted vertical lines show the boundary of the filament for the respective orthogonal cuts shown. The C_v parameter (Equation 4.6) calculated for each cut is also shown in the top-left corner.

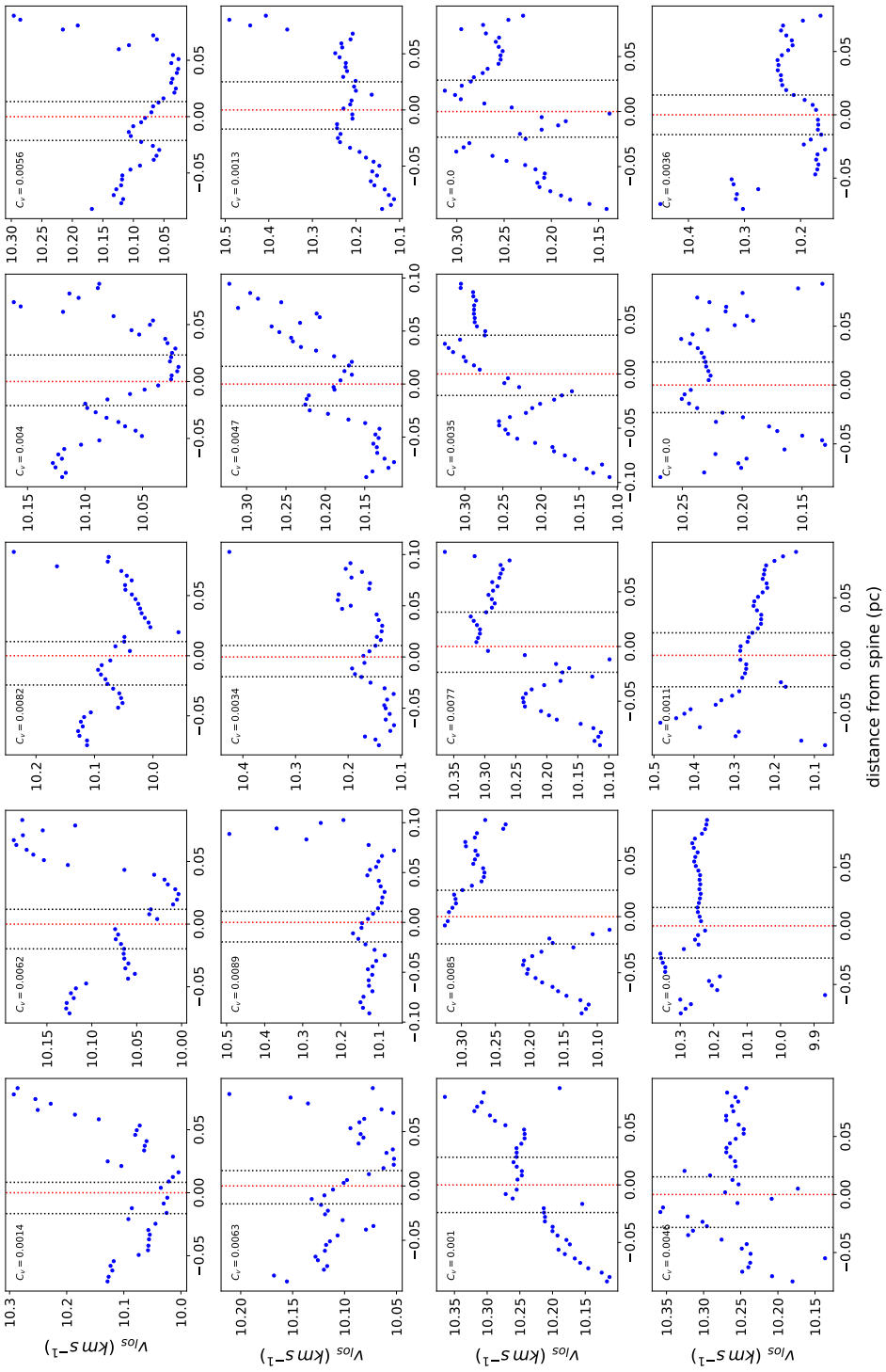

Figure C.3: Same as Figure C.2, but for Filament-2

Appendix D

Robustness of Number of Components Fit Using Bayesian Approach

D.1 Motivation

In the work presented in this thesis, I use multi-component analysis to study the gas kinematics in great detail using high-sensitivity observations. One systematic way to fit multiple components and determine the best-fit model across a large number of pixels is the Bayesian approach presented by Sokolov et al. (2020). We use this method exclusively to select the optimal model for each pixel in our data in Chapter 4. This approach is much more time-consuming than selecting the best fit with χ^2 or the Akaike Information Criterion (AIC), but it is a better method with a more robust statistical foundation. All our subsequent analysis depends on the best-fit components determined by this method. Therefore, it is necessary to show the reliability of this approach across the ranges of parameters usually probed. In this section, we quantify the robustness of this approach with synthetic spectra to mimic the observed spectra by comparing the input model to the one selected by the Bayesian approach. We primarily examine two key aspects :

1. How reliable is the number of components determined to be optimal by this method? How often can it reliably distinguish between a one-component and a two-component input spectrum?

2. How accurate are the fitted parameters compared with the input parameters?

D.2 Method

To perform this check, we generate $\approx 5 \times 10^4$ synthetic spectra for NH_3 (1,1) and (2,2) lines, which are the spectral lines used in our analysis in the previous chapters. We generate one- and two-component spectra on a grid of parameters typical of the interior of dense cores, where we have focused our study. We then add different levels of noise to study how the signal-to-noise ratio (SNR) in the observations affects the results of this fitting technique. We use the

`cold_ammonia` model from the python package `pyspeckit` to generate the synthetic spectra from the input parameters. We selected this model as it was exclusively used for the fits in our projects. As mentioned in Section 4.4.1, the parameters considered in this model are: kinetic and excitation temperatures (T_K and T_{ex}), NH_3 column density ($N(NH_3)$), velocity dispersion (σ_v), centroid velocity (v_{LSR}), and the ortho-NH_3 fraction with respect to the total NH_3 column density (f_{ortho}).

For the one-component spectra, we vary the T_{ex} and $N(NH_3)$, as they determine the intensity of the hyperfines in the NH_3 (1,1) line, which is important for the kinematics. Further, we vary $\sigma_v$to study if broad lines could be mistakenly taken to be two separate components by the method. For two-component spectra, we keep the parameters of one of the components constant, and for the other components, vary T_{ex} and $N(NH_3)$. We also vary v_{LSR} for the second component to determine whether two nearby components can be recovered as two separate components, or the lines are blended together. All the other parameters are kept constant to reduce the grid size, and their values are taken to represent typical physical conditions in the interior of dense cores (see Chapter 4). Tables D.1 and D.2 shows the grid of parameters and noises used in generating the one- and two-component synthetic spectra. These values were considered keeping in mind the values we observed in Chapter 4 in the regions with multi-component fits so that we can directly compare the results from this analysis to that in Chapter 4.

Parameters	Values considered in the grid
T_K (K)	10
T_{ex} (K)	3.5, 4.5, 5.5, 6.5, 7.5
$\log_{10}$ ($N(NH_3)$, cm^{-2})	13.5, 13.7, 13.9, 14.1, 14.3, 14.5, 14.7, 14.9, 15.1
σ_v ($km\,s^{-1}$)	0.11, 0.14, 0.17, 0.2, 0.23
v_{LSR} ($km\,s^{-1}$)	10
f_{ortho}	0.5
noise (K)	0.1, 0.13, 0.18, 0.2, 0.23

Table D.1: Parameter grid used for the one-component synthetic spectra, along with the noise added.

For each combination of parameters and noises considered, we generate a signal spectrum, and then add to it 20 realisations of randomly generated Gaussian noise using `random.normal` function in the `numpy` python package. Then, the sample size generated is reasonable for statistical analysis. Finally, for each synthetic spectra, we attempt to fit up to three components, using the exact same procedure described in Section 4.4.1, but modifying the parameter ranges for the priors, to cover our grid. We use uniformly distributed ranges of $7 - 13$ K for T_K, $3.3 - 11$ K for T_{ex}, $10^{13.4} - 10^{15.4}$ cm^{-2} for $N(NH_3)$, $0.05 - 0.7$ $km\,s^{-1}$ for σ_v, and $9.8 - 10.7$ $km\,s^{-1}$ for v_{LSR}. These ranges are wide enough to cover the ranges of values considered here, and also typically observed in dense cores.

Parameters	Values for the first component	Values considered in the grid for the second component
T_K (K)	11	9
T_{ex} (K)	9	3.5, 4.8, 5.1, 6.4, 7.7
$\log_{10}$ (N(NH_3), cm^{-2})	15.1	13.5, 13.7, 13.9, 14.1, 14.3, 14.5, 14.7, 14.9
σ_v ($km\,s^{-1}$)	0.08	0.11
v_{LSR} ($km\,s^{-1}$)	10.6	10, 10.2, 10.3, 10.4, 10.43, 10.47, 10.5, 10.53
f_{ortho}	0.5	0.5
noise (K)	0.1, 0.13, 0.18, 0.2	

Table D.2: Parameter grid used for the two-component synthetic spectra, along with the noise added.

D.3 Results

D.3.1 Optimal number of components decided by Bayesian model selection

Figure D.1 shows the number of components in the best model determined with the Bayesian model selection method to the one-component synthetic spectra across the range of values in T_{ex}, N(NH_3) and σ_v considered (see Table D.1). Instead of showing this result against different noise levels added, we instead show the variation with the peak signal-to-noise ratio (SNR) in the NH_3 (1,1) spectra, which is defined as the ratio between the peak NH_3 (1,1) intensity and the noise level. For most of the spectra across the parameter space considered, the number of components is correctly determined to be one. As expected, for lower intensity (low T_{ex} and/or small N(NH_3)), a small number of spectra could not be fit well with one component. As seen from the comparison with SNR, these spectra without a reliable fit are a small fraction (<10%) of the sample with SNR<5. However, the most important result here is that **there are no false positives**, i.e., for the parameter ranges considered, none of the spectra is falsely fit with two components. This result shows that the two-component fits in our results (e.g. in Chapter 4) are reliable. Overall, 98% of the one-component spectra are correctly identified with a one-component fit by the model.

Similarly, the number of components identified by the model in the two-component synthetic spectra is shown in Figure D.2 across the grid of T_{ex}, N(NH_3) and Δv considered (where Δv is the difference in velocity of the two components), as well as the different levels of added noises. Similarly to the results for the one-component spectra, the number of components is correctly determined for the high-intensity (high T_{ex} and/or large N(NH_3)) and low noise. We also see that for closely separated components (small Δv), the model has difficulties separating the two components, and the lower the Δv, the higher the probability of a two-component spectrum being identified as having one-component by the model. We again note that **there are no instances of**

a false positive, i.e., a two-component spectrum is never identified as a three-component one by the model, regardless of the noise, intensities, and the separation between the two components in the parameter space we probe. Overall, 83% of the two-component spectra are correctly identified with a two-component fit by the model.

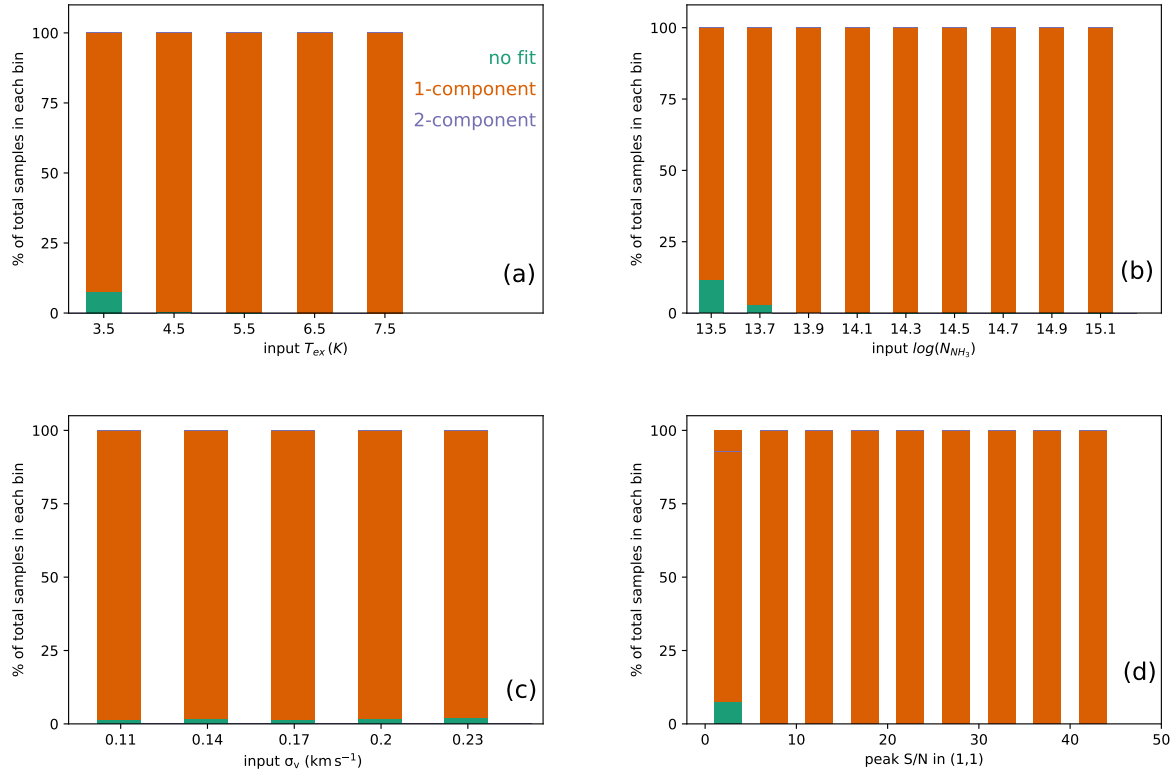

Figure D.1: Number of components fit by the Bayesian method to the one-component input spectra, with variation of T_{ex}, N(NH_3), σ_v, and SNR in panels (a)-(d), respectively. It shows that only data with very low SNR (<5) are poorly fitted, which also relates to models with low T_{ex} or N(NH_3).

D.3.2 Comparison of input and output parameters

Next, we look at the parameters given by the best fit model and compare them to the parameters considered to generate the spectra. This gives us an idea of how well-constrained the different parameters are. For the distribution of each output parameters, we calculate the 50th, 16th, and the 84th percentiles. The first gives us the median of the output values, and the other two provide the one standard deviation (SD) spread around the median. We define the uncertainty in the output values as the 16th and the 84th percentile values relative to the input value of the parameter.

Figure D.3 shows the violin plots comparing different values of T_{ex}, N(NH_3) and σ_v from the fit against the input values. For T_{ex} and σ_v, we have very good agreement between the input and

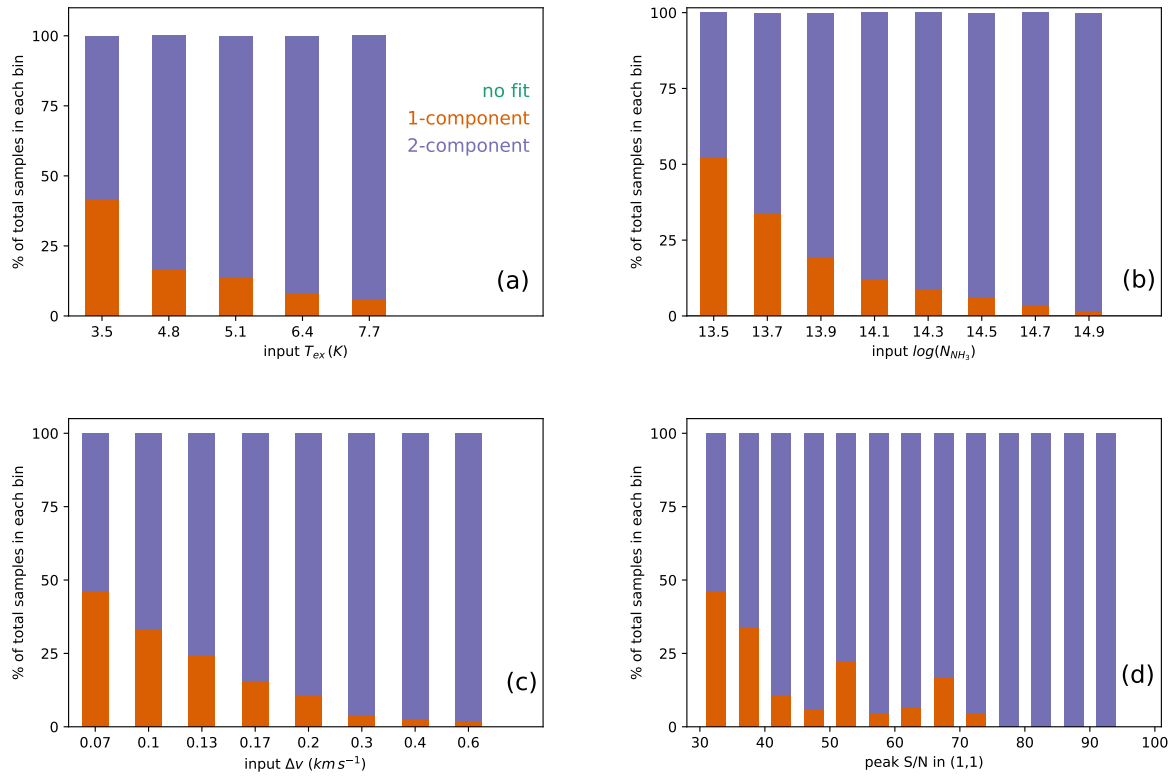

Figure D.2: Number of components fit by the Bayesian method to the two-component input spectra, with variation of $T_{\rm ex}$, N(NH_3), Δv, and SNR in panels (a)-(d), respectively.

output values across the sampled parameter space. The uncertainties for all the calculated $T_{\rm ex}$ values are less than 1 K. For models with input $\sigma_{\rm v} < 0.2\,{\rm km\,s^{-1}}$, the uncertainties derived for $\sigma_{\rm v}$ are within $\pm 0.01\,{\rm km\,s^{-1}}$ of the input value, and for $\sigma_{\rm v} \geq 0.2\,{\rm km\,s^{-1}}$, they lie within $\pm 0.02\,{\rm km\,s^{-1}}$. For N($NH_3$), especially at the lower end, we see a significant spread in the N(NH_3) values determined by the fit. This is likely because at those column densities, NH_3 is optically thin ($\tau \ll 1$), which makes it difficult to have a good estimate of the column density from the fit (see Section 3.5.2.) However, in the high-column density samples, we have a very good determination of N(NH_3), as those spectra have a very high signal-to-noise ratio (SNR). For log (N(NH_3)) $\geq$ 14.3 in the input, the uncertainties are up to $\pm$0.05 dex, and for input log (N(NH_3)) < 14.3, they lie within (-0.2, 0.5) dex.

We see similar trends in the comparison of input and output parameters for the two-component spectra (Figure D.4). Here, we only consider the samples with a two-component fit and show only the comparisons of the varied parameters for the second component (all parameters were kept constant for the first component). Instead of comparing the velocity of the second component, which was the variable parameter, we show here the comparison of separation in velocity between the two components (Δv), which is what we are ultimately interested in. For $T_{\rm ex}$, we have good estimates from the fit for all the values, although they show a marginally wider spread

than the one-component results in Figure D.3. For the input T_{ex}<7 K, the uncertainties are within ±1 K, while for T_{ex}=7.7 K, it is [-1.6, 1] K. We have excellent determinations of Δv across the samples. We calculate uncertainties on the Δv values to be within ±0.08 km s^{-1}, and for Δv ≥ 0.3 km s^{-1}, they are within ±0.01 km s^{-1}. Similar to the one-component results, we see a larger spread in the N(NH_3) values determined by the fit, particularly in the low-N(NH_3) samples. For log (N(NH_3)) ≥ 14.3 in the input, the uncertainties are within (-0.05, 0.15) dex, and for input log (N(NH_3)) < 14.3, they lie within (-0.2, 0.6) dex. All these uncertainties are smaller than the variations in the parameter studied in Chapter 4.

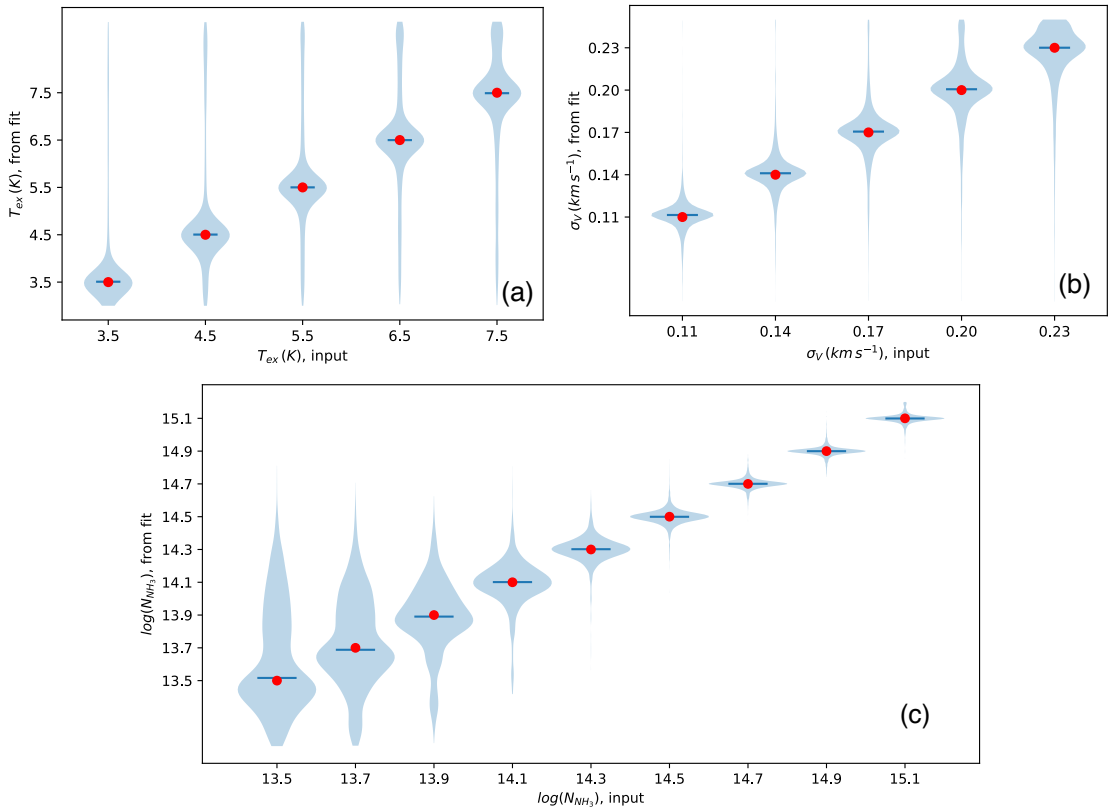

Figure D.3: Distribution of the values from fit against the corresponding input values for T_{ex}, σ_v, and N(NH_3) in the one-component synthetic spectra. The width at each height is proportional to the number of models with that output value in the sample with the input value indicated. The red circles mark the points where input and output values are equal for the parameter, and the blue horizontal lines show the median of the distribution of the values from fit.

D.4 Conclusions

For the range of values considered for T_{ex}, N(NH_3), σ_v and Δv, we find no single case of false detection, ie., where a spectrum is fitted with more components than are actually present. This

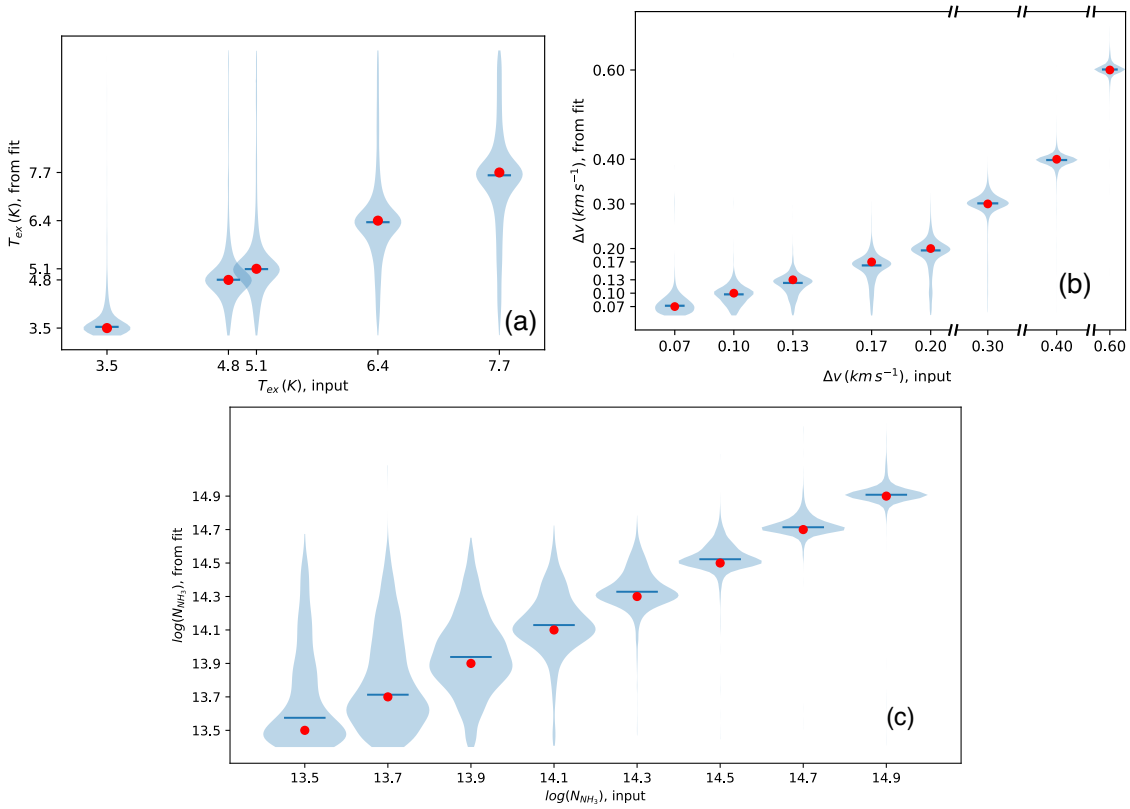

Figure D.4: Distribution of the values from fit against the corresponding input values for $T_{\rm ex}$, Δv, and N(NH_3) in the one-component synthetic spectra. The width at each height is proportional to the number of models with that output value in the sample with the input value indicated. The red circles mark the points where input and output values are equal for the parameter, and the blue horizontal lines show the median of the distribution of the values from fit.

is a significant result, as it shows that the instances when multiple components are detected in observational data by the model, very likely the spectrum actually contains that number of components. This strengthens the results and conclusions from multi-component analysis using this approach (e.g. Chapter 4).

We find the model has difficulty identifying a component only towards the low-SNR regime (low intensity or high noise). The model also gives very reliable estimates of the excitation temperature and the kinematic information (line positions and dispersion). For low column density regions, the estimate of N(NH_3) is less reliable due to the transitions being optically thin ($\tau \ll 1$), something which we previously see observationally in Chapter 3 (Section 3.5.2).

Bibliography

André, P., Di Francesco, J., Ward-Thompson, D., et al. 2014, in Protostars and Planets VI, ed. H. Beuther, R. S. Klessen, C. P. Dullemond, & T. Henning, 27

André, P., Men'shchikov, A., Bontemps, S., et al. 2010a, A&A, 518, L102

André, P., Men'shchikov, A., Bontemps, S., et al. 2010b, A&A, 518, L102

Andre, P., Ward-Thompson, D., & Barsony, M. 2000, in Protostars and Planets IV, ed. V. Mannings, A. P. Boss, & S. S. Russell, 59

Arzoumanian, D., André, P., Könyves, V., et al. 2019, A&A, 621, A42

Bailey, N. D., Basu, S., & Caselli, P. 2015, ApJ, 798, 75

Barranco, J. A. & Goodman, A. A. 1998, ApJ, 504, 207

Bergin, E. A. & Langer, W. D. 1997, ApJ, 486, 316

Bergin, E. A. & Tafalla, M. 2007, ARA&A, 45, 339

Caselli, P., Benson, P. J., Myers, P. C., & Tafalla, M. 2002, ApJ, 572, 238

Caselli, P., Bizzocchi, L., Keto, E., et al. 2017a, A&A, 603, L1

Caselli, P., Bizzocchi, L., Keto, E., et al. 2017b, A&A, 603, L1

Caselli, P. & Ceccarelli, C. 2012, A&A Rev., 20, 56

Caselli, P. & Myers, P. C. 1995, ApJ, 446, 665

Ceccarelli, C., Caselli, P., Bockelée-Morvan, D., et al. 2014, in Protostars and Planets VI, ed. H. Beuther, R. S. Klessen, C. P. Dullemond, & T. Henning, 859

Chen, C.-Y., Mundy, L. G., Ostriker, E. C., Storm, S., & Dhabal, A. 2020a, MNRAS, 494, 3675

Chen, H. H.-H., Offner, S. S. R., Pineda, J. E., et al. 2020b, arXiv e-prints, arXiv:2006.07325

Chen, H. H.-H., Pineda, J. E., Goodman, A. A., et al. 2019, ApJ, 877, 93

Choudhury, S., Pineda, J. E., Caselli, P., et al. 2020, A&A, 640, L6

Choudhury, S., Pineda, J. E., Caselli, P., et al. 2021, A&A, 648, A114

Crapsi, A., Caselli, P., Walmsley, M. C., & Tafalla, M. 2007, A&A, 470, 221

Dame, T. M., Hartmann, D., & Thaddeus, P. 2001, ApJ, 547, 792

Di Francesco, J., André, P., & Myers, P. C. 2004, ApJ, 617, 425

Dunham, M. M., Allen, L. E., Evans, Neal J., I., et al. 2015, ApJS, 220, 11

Dunham, M. M., Stutz, A. M., Allen, L. E., et al. 2014, in Protostars and Planets VI, ed. H. Beuther, R. S. Klessen, C. P. Dullemond, & T. Henning, 195

Enoch, M. L., Evans, Neal J., I., Sargent, A. I., & Glenn, J. 2009, ApJ, 692, 973

Evans, Neal J., I., Rawlings, J. M. C., Shirley, Y. L., & Mundy, L. G. 2001, ApJ, 557, 193

Ferrière, K. M. 2001, Rev. Mod. Phys., 73, 1031

Foreman-Mackey, D., Hogg, D. W., Lang, D., & Goodman, J. 2013, PASP, 125, 306

Foster, J. B., Rosolowsky, E. W., Kauffmann, J., et al. 2009, ApJ, 696, 298

Friesen, R. K., Di Francesco, J., Shirley, Y. L., & Myers, P. C. 2009, ApJ, 697, 1457

Friesen, R. K., Medeiros, L., Schnee, S., et al. 2013, MNRAS, 436, 1513

Friesen, R. K., Pineda, J. E., co-PIs, et al. 2017, ApJ, 843, 63

Fuller, G. A., Myers, P. C., Welch, W. J., et al. 1991, ApJ, 376, 135

Gaia Collaboration. 2018, VizieR Online Data Catalog, I/345

Galli, D., Walmsley, M., & Gonçalves, J. 2002, A&A, 394, 275

Galli, P. A. B., Loinard, L., Ortiz-Léon, G. N., et al. 2018, ApJ, 859, 33

Ginsburg, A. & Mirocha, J. 2011, PySpecKit: Python Spectroscopic Toolkit

Ginsburg, A., Sokolov, V., de Val-Borro, M., et al. 2022, arXiv e-prints, arXiv:2205.04987

Goldsmith, P. F. 2001, ApJ, 557, 736

Goldsmith, P. F., Heyer, M., Narayanan, G., et al. 2008, ApJ, 680, 428

Gong, Y., Belloche, A., Du, F. J., et al. 2021, A&A, 646, A170

Goodman, A. A., Barranco, J. A., Wilner, D. J., & Heyer, M. H. 1998, ApJ, 504, 223

Güver, T. & Özel, F. 2009, MNRAS, 400, 2050

Habart, E., Boulanger, F., Verstraete, L., et al. 2003, A&A, 397, 623

Habing, H. J. 1968, Bull. Astron. Inst. Netherlands, 19, 421

Hacar, A., Tafalla, M., Forbrich, J., et al. 2018, A&A, 610, A77

Hacar, A., Tafalla, M., Kauffmann, J., & Kovács, A. 2013, A&A, 554, A55

Harju, J., Daniel, F., Sipilä, O., et al. 2017, A&A, 600, A61

Hasegawa, T. I., Herbst, E., & Leung, C. M. 1992, ApJS, 82, 167

Henshaw, J. D., Caselli, P., Fontani, F., et al. 2013, MNRAS, 428, 3425

HI4PI Collaboration, Ben Bekhti, N., Flöer, L., et al. 2016, A&A, 594, A116

Ho, P. T. P. & Townes, C. H. 1983, ARA&A, 21, 239

Hollenbach, D. J. & Tielens, A. G. G. M. 1999, Reviews of Modern Physics, 71, 173

Houk, N. & Smith-Moore, M. 1988, Michigan Catalogue of Two-dimensional Spectral Types for the HD Stars. Volume 4, Declinations -26°.0 to -12°.0., Vol. 4

Hsieh, C.-H., Arce, H. G., Mardones, D., Kong, S., & Plunkett, A. 2021, ApJ, 908, 92

Ivlev, A. V., Silsbee, K., Sipilä, O., & Caselli, P. 2019, ApJ, 884, 176

Johnstone, D., Di Francesco, J., & Kirk, H. 2004, ApJ, 611, L45

Kamazaki, T., Saito, M., Hirano, N., Umemoto, T., & Kawabe, R. 2003, ApJ, 584, 357

Kauffmann, J., Bertoldi, F., Bourke, T. L., Evans, N. J., I., & Lee, C. W. 2008, A&A, 487, 993

Kirk, H., Johnstone, D., & Tafalla, M. 2007, ApJ, 668, 1042

Kirk, H., Pineda, J. E., Johnstone, D., & Goodman, A. 2010, ApJ, 723, 457

Koch, E., Rosolowsky, E., & Leroy, A. K. 2018, Research Notes of the American Astronomical Society, 2, 220

Koumpia, E., Harvey, P. M., Ossenkopf, V., et al. 2015, A&A, 580, A68

Kounkel, M., Hartmann, L., Loinard, L., et al. 2017, ApJ, 834, 142

Lada, C. J. 1987, in Star Forming Regions, ed. M. Peimbert & J. Jugaku, Vol. 115, 1

Ladjelate, B., André, P., Könyves, V., & Men'shchikov, A. 2016, in IAU Symposium, Vol. 315, From Interstellar Clouds to Star-Forming Galaxies: Universal Processes?, ed. P. Jablonka, P. André, & F. van der Tak, E46

Ladjelate, B., André, P., Könyves, V., et al. 2020a, arXiv e-prints, arXiv:2001.11036

Ladjelate, B., André, P., Könyves, V., et al. 2020b, arXiv e-prints, arXiv:2001.11036

Larson, R. B. 1981, MNRAS, 194, 809

Launhardt, R., Stutz, A. M., Schmiedeke, A., et al. 2013, A&A, 551, A98

Leroy, A. K., Hughes, A., Schruba, A., et al. 2016, ApJ, 831, 16

Loren, R. B., Wootten, A., & Wilking, B. A. 1990, ApJ, 365, 269

Lovas, F. J., Bass, J. E., Dragoset, R. A., & Olsen, K. J. 2009, NIST Recommended Rest Frequencies for Observed Interstellar Molecular Microwave Transitions - 2009 Revision, (version 3.0), http://physics.nist.gov/restfreq, [Online; accessed 15-May-2020]

Mangum, J. G., Emerson, D. T., & Greisen, E. W. 2007a, A&A, 474, 679

Mangum, J. G., Emerson, D. T., & Greisen, E. W. 2007b, A&A, 474, 679

Markwardt, C. B. 2009, in Astronomical Society of the Pacific Conference Series, Vol. 411, Astronomical Data Analysis Software and Systems XVIII, ed. D. A. Bohlender, D. Durand, & P. Dowler, 251

McKee, C. F. & Ostriker, J. P. 1977, ApJ, 218, 148

McMillan, P. J. 2017, MNRAS, 465, 76

Motte, F., Andre, P., & Neri, R. 1998, A&A, 336, 150

Myers, P. C. 1983, ApJ, 270, 105

Myers, P. C. & Benson, P. J. 1983, ApJ, 266, 309

Ortiz-León, G. N., Loinard, L., Dzib, S. A., et al. 2018, ApJ, 869, L33

Pagani, L., Bacmann, A., Cabrit, S., & Vastel, C. 2007, A&A, 467, 179

Pineda, J. E., Goodman, A. A., Arce, H. G., et al. 2010, ApJ, 712, L116

Pineda, J. E., Goodman, A. A., Arce, H. G., et al. 2011a, ApJ, 739, L2

Pineda, J. E., Goodman, A. A., Arce, H. G., et al. 2011b, ApJ, 739, L2

Pineda, J. E., Offner, S. S. R., Parker, R. J., et al. 2015, Nature, 518, 213

Pineda, J. E., Schmiedeke, A., Caselli, P., et al. 2021, ApJ, 912, 7

Pineda, J. E., Segura-Cox, D., Caselli, P., et al. 2020, Nature Astronomy, 4, 1158

Polychroni, D., Schisano, E., Elia, D., et al. 2013, ApJ, 777, L33

Pon, A., Johnstone, D., & Kaufman, M. J. 2012, ApJ, 748, 25

Robitaille, T. P. & Whitney, B. A. 2010, ApJ, 710, L11

Rosolowsky, E. W., Pineda, J. E., Foster, J. B., et al. 2008, ApJS, 175, 509

Schmiedeke, A., Pineda, J. E., Caselli, P., et al. 2021, ApJ, 909, 60

Scott, D. W. 1992, Multivariate Density Estimation: Theory, Practice, and Visualization (New York: John Wiley & Sons)

Sokolov, V., Pineda, J. E., Buchner, J., & Caselli, P. 2020, ApJ, 892, L32

Swift, J. J., Welch, W. J., & Di Francesco, J. 2005, ApJ, 620, 823

Tafalla, M., Myers, P. C., Caselli, P., Walmsley, C. M., & Comito, C. 2002, ApJ, 569, 815

Taquet, V., Wirström, E. S., Charnley, S. B., et al. 2017, A&A, 607, A20

Walsh, A. J., Myers, P. C., Di Francesco, J., et al. 2007, ApJ, 655, 958

Ward-Thompson, D., Kirk, J. M., André, P., et al. 2010, A&A, 518, L92

White, G. J., Drabek-Maunder, E., Rosolowsky, E., et al. 2015, MNRAS, 447, 1996

Williams, J. P. & Myers, P. C. 2000, ApJ, 537, 891

Wirström, E. S., Charnley, S. B., Persson, C. M., et al. 2014, ApJ, 788, L32

Young, K. E., Lee, J.-E., Evans, Neal J., I., Goldsmith, P. F., & Doty, S. D. 2004, ApJ, 614, 252

Zhang, G.-Y., André, P., Men'shchikov, A., & Wang, K. 2020, A&A, 642, A76

Zucconi, A., Walmsley, C. M., & Galli, D. 2001, Astron. Astrophys., 376, 650

Zucker, C., Schlafly, E. F., Speagle, J. S., et al. 2018, ApJ, 869, 83

Acknowledgements

My journey throughout my PhD has been nothing short of an adventure of the most epic proportions. There have, of course, been many ups and downs, not to mention more than half of it being during a worldwide pandemic. Yet, there has seldom been a day I did not look forward to in my first taste of the life of research. A great number of people made this would-be difficult journey much more fun and enjoyable, and it would be unforgivable to not mention at least some of them here.

I definitely have to start with my supervisors, Paola Caselli and Jaime Pineda, without whom this work would not have been possible in the very literal sense of the word.
Paola, you have been an incredible mentor with invaluable guidance and advice throughout these years. You gave me the independence to pursue my interests while supporting and offering help whenever needed. I will never be able to thank you enough for everything: from offering me the opportunity to start my research career in your group to your inputs during the preparation of this thesis.
Jaime, words fail me when I begin even to fathom the part you played in my PhD. You have been there to guide me, to offer a helping hand, and at more times than I would care to admit, to give me that push when I was stuck and desperately needed it. You have been patient through the tiniest things I went to you for and taken the time to explain the most complicated ones in excruciating detail. You have been the most amazing supervisor, beyond anything I could ever have hoped for. Thank you!

At times, I still have difficulty believing how fortunate I have been to have worked in a group as exciting as our CAS group. Birgitta, from helping me navigate through life in Germany when I started, to helping me with every single silly question I had regarding the thesis submission, you have been a true life-saver. And of course, how can I forget your awesome cakes and cookies that lit up even the most stressful day! Max and Joaquin, there was never a dull moment in the office with you around. Before Covid cut short our shared time, we really did have the most fun office, didn't we?

Elena, you have been so nice and ready to help with anything at any time. Anika, Dom, and Felipe; for all the chats and the tips to navigate the PhD life. Felipe, thanks also for introducing me to your amazing football group. And to every single member of the CAS group, for such a lively environment. My heartfelt thanks to all of you! I have to thank the wonderful people in the football group of MPA-MPE-IPP, too. At least two days almost every week, I knew something

really fun was waiting for me at the end.

I want to take this opportunity to also thank the administrative people at MPE, in particular, Angie and Erich. Thank you for your help in everything, big or small, and of course, the friendly chats.

My amazing friends, life is a lot easier with you guys around. Joya, Sankha, Deep, Champak, and Naba; random chats with you guys had the surprising power to turn the day around, especially while being stuck in my apartment during the lockdowns. Arvind and Lokahith, there was something very comforting about having shared the student life with you two since the IISER days, knowing you are going through the same things, and having the same troubles, too. (You might even say there was something *Bengaluru-ian* about it:-P). Abhijeet, Ilkham, and Periklis; we shared the PhD life from the start to the end. It has been a truly memorable journey filled with numerous trips. Travelling to various places with you three and Lokahith has been a highlight of my time in Europe (We could not make as many trips as we would have liked to, though. Let's meet soon and plan another!). And to Ronald, my companion in swimming, football, and Bayern matches: I will forever be thankful for your friendship.

Finally, and perhaps most importantly, I want to thank my family, especially my parents and my brother. *Ma, Deuta*; you have been my constant sources of encouragement and my two biggest pillars of strength. You have always backed me to follow my interests and have sacrificed much to help me through it all. Words will never be enough, but I want to say my thanks nonetheless. *Moumon*, my little brother, I am so grateful for the fun we continue to have despite being so far apart. And to my cousins, my dearest *pehi*s, and *mahi*s, thanks for all the never-ending calls, video chats and our *adda*s, thanks for never letting me feel I was so far from home.

I am sure to have missed some names of the wonderful people who made these PhD years so enjoyable, but know that I am truly thankful to each and every one of you. I will forever cherish this amazing experience.

Thank you!

Astronomy and Astrophysics
Editor in Chief: T. Forveille

T. Forveille
Astronomy & Astrophysics
Observatoire de Paris
61, avenue de l'Observatoire
75014 Paris, France

Tel.: 33 0(1) 43 29 05 41
Fax: 33 0(1) 43 29 05 57
e-mail: aanda.paris@obspm.fr
Web: http://www.aanda.org

merging
Annales d'Astrophysique
Arkiv for Astronomi
Bulletin of the Astronomical Institutes of the Netherlands
Bulletin Astronomique
Journal des Observateurs
Zeitschrift fur Astrophysik
Bulletin of the Astronomical Institutes of Czechoslovakia

Paris, 8 February 2022

Reprint Permission

Material:
Article by Choudhury, S., Pineda, J. E., Caselli, P., et al. 2021, A&A, 648, A114
Article by Choudhury, S., Pineda, J. E., Caselli, P., et al. 2020, A&A, 640, L6

To be used in:
PhD thesis with provisional title "Structure and Dynamics of Dense Low-mass Cores, Ludwig Maximilian University of Munich

Permission granted to:
Spandan Choudhury
Max-Planck-Institut für extraterrestrische Physik
Garching bei München, Germany
spandan@mpe.mpg.de

I hold copyright on the material referred to above, and hereby grant permission for its use as requested herewith.

The article should be reproduced as a whole in a coherent fashion fully consistent with the version published in A&A.

Credit should be given as follows:
Credit: Author, A&A, vol, page, year, reproduced with permission © ESO.

Thierry Forveille
A&A Editor-in-Chief

Sponsored by Argentina, Armenia, Austria, Belgium, Bulgaria, Chile, Croatia, Czech Republic, Denmark, Estonia, Finland, France, Germany, Greece, Hungary, Italy, Lithuania, Netherlands, Norway, Poland, Portugal, Slovak Republic, Spain, Sweden, and Switzerland.
Produced and distributed by EDP Sciences for ESO.